University of Alberta

Development of a UV Sagnac Interferometer

for Fourier Transform Raman Spectroscopy

by

Bin Li ©

A thesis submitted to the Faculty of Graduate Studies and Research in partial fulfillment of the

requirements for the degree of *Master of Science*

Department of Electrical and Computer Engineering

Edmonton, Alberta

Fall 2003

National Library of Canada
Bibliothèque nationale du Canada

Acquisitions and Bibliographic Services
Acquisisitons et services bibliographiques

395 Wellington Street
Ottawa ON K1A 0N4
Canada

395, rue Wellington
Ottawa ON K1A 0N4
Canada

Your file Votre référence
ISBN: 0-612-87808-2
Our file Notre référence
ISBN: 0-612-87808-2

The author has granted a non-exclusive licence allowing the National Library of Canada to reproduce, loan, distribute or sell copies of this thesis in microform, paper or electronic formats.

L'auteur a accordé une licence non exclusive permettant à la Bibliothèque nationale du Canada de reproduire, prêter, distribuer ou vendre des copies de cette thèse sous la forme de microfiche/film, de reproduction sur papier ou sur format électronique.

The author retains ownership of the copyright in this thesis. Neither the thesis nor substantial extracts from it may be printed or otherwise reproduced without the author's permission.

L'auteur conserve la propriété du droit d'auteur qui protège cette thèse. Ni la thèse ni des extraits substantiels de celle-ci ne doivent être imprimés ou aturement reproduits sans son autorisation.

Canada

University of Alberta

Library Release Form

Name of Author: *Bin Li*

Title of Thesis: *Development of a UV Sagnac Interferometer for Fourier Transform Raman Spectroscopy*

Degree: *Master of Science*

Year this Degree Granted: *2003*

Permission is hereby granted to the University of Alberta Library to reproduce single copies of this thesis and to lend or sell such copies for private, scholarly or scientific research purposes only.

The author reserves all other publication and other rights in association with the copyright in the thesis, and except as herein before provided, neither the thesis nor any substantial portion thereof may be printed or otherwise reproduced in any material form whatever without the author's prior written permission.

(Signed) _

2nd floor
Electrical and Computer Engineering Research Facility

April 29, 2003
Date

University of Alberta

Faculty of Graduate Studies and Research

The undersigned certify that they have read, and recommend to the Faculty of Graduate Studies and Research for acceptance, a thesis entitled **Development of a UV Sagnac Interferometer for Fourier Transform Raman Spectroscopy** submitted by **Bin Li** in partial fulfillment of the requirements for the degree of **Master of Science**.

Dr. R. Fedosejevs

Dr. Y.Y. Tsui

Dr. G.R. Lopphow,

April 29, 2003

Date

Abstract

A comprehensive study of Fourier Transform Ultra-Violet Raman Spectroscopy using a Sagnac Interferometer has been carried out. For comparison, Raman Spectroscopy with a conventional dispersive spectrometer was also carried out. Selected sample spectra were obtained and an analysis of N_2 Raman spectra was given. The optical components of the experimental setup were carefully calibrated, especially the UV CCD camera in order that the quantitative efficiency of the Sagnac interferometer could be compared to a classical dispersive spectrometer. The performance of the Sagnac interferometer was characterized experimentally and was analyzed theoretically. Fourier Transform Raman spectra of selected samples were obtained with the Sagnac Interferometer and were compared with their conventional Raman Spectra. It is shown that single shot FT UV Raman spectroscopy is feasible. This Fourier Transform Spectrometer based on a Sagnac Interferometer can be also applied to other low light level spectroscopic measurements such as Laser Induced Breakdown Spectroscopy and Laser Induced Fluorescence.

Acknowledgement

I would like to thank my supervisor Dr. R. Fedosejevs for his constant encouragements and help in completing my thesis. Thanks to Blair and Rick for their continuing help. I would also like to thank the University of Alberta for offering financial support and research facilities to complete my graduate studies.

Table of Contents

Chapter Page

I Introduction 1

II Raman spectroscopy with a Spectrometer 9

2.1 Experimental setup and procedure 9

2.2 Experimental results 15

2.3 Theoretical calculation of Raman spectrum of Nitrogen 19

III FT UV Raman Spectroscopy with a Sagnac Interferometer 24

3.1 The calibration of the optical components 26

3.1.1 Calibration of UV Raman Filters @ 266nm 27

3.1.2 The calibration of a dielectric mirror 30

3.1.3 The liquid filter, Fluorobenzene in Cyclohexane solvent.....33

3.1.4 The calibration of UV beam Splitter 37

3.1.5 The calibration of UV CCD 42

3.2 Theoretical Model 57

3.2.1 The fringe pattern of Sagnac interferometer 57

3.2.2 Fringe formation in a Sagnac interferometer 61

3.2.3 Theoretical resolution 68

3.3 The characteristics of a Sagnac interferometer 71

3.3.1 Mercury spectra for different positions of the movable mirror 72

3.3.2 The position of UV CCD 77

3.3.3 The calibration of wavelength or wave number 79

3.3.4 The visibility versus the spacing of the fringe 81

3.4 Experimental measurements of Raman spectra 85

3.4.1 Water (H_2O) 86

3.4.2 Methanol (CH_3OH) 88

3.4.3 Cyclohexane (C_6H_6) 92

3.4.4 Ethanol (CH_3CH_2OH) 94

3.4.5 Air (Oxygen & Nitrogen).....96

3.4.6 Teflon 98

3.5 Theoretical calculation of FT Raman spectrum of Nitrogen 103

3.6 Comparison to previous published results 108

IV Other Applications of FT spectroscopy with a Sagnac Interferometer

4.1 FT LIBS with a Sagnac Interferometer 111

4.2 FT LIF with a Sagnac Interferometer.....114

V Discussions and Conclusions 116

VI References 120

Appendix A Pictures of experimental setup 124

Appendix B The experimental procedure 131

Appendix C Fourier Transform program with an example output graph 143

Appendix D The characteristics of the movable mirror with a FT Hg spectrum 148

Appendix E The characteristics of UV CCD position with a FT Hg spectrum 154

List of Tables

Table 2.3-1 The summary of theoretical calculation of N_2 Raman signal 23

Table 3.1.5-1 The readout noise and the background level of the UV CCD camera at various readout rates 43

Table 3.1.5-2 The Dark Current of the UV CCD camera 45

Table 3.1.5-3 Calibration of responsivity using a Tungsten lamp 51

Table 3.3.1-1 Results from the FT Hg spectra by scanning the movable mirror 72

Table 3.3.4-1 The visibility vs. the fringe spacing of Teflon Rayleigh scattering 82

List of Figures

Chapter I Introduction

Fig. 1-1 The experimental setup of Raman spectroscopy with a grating spectrometer 2

Fig. 1-2 The experimental setup of Raman spectroscopy with a Michelson interferometer.....2

Fig. 1-3 The experimental setup of Raman spectroscopy with a Sagnac Interferometer...3

Chapter II Raman spectroscopy with a Spectrometer

Fig. 2.1-1 The experimental setup of Raman spectroscopy with a grating spectrometer...9

Fig. 2.1- 2 The experimental Raman spectrum of Air with some stray scattered light ...10

Fig. 2.1- 3 The experimental Raman and Rayleigh spectrum of Air accumulated over1000 shots using the liquid filter to block the Rayleigh signal 10

Fig. 2.2-1 The experimental Raman spectrum of Methanol, 400 shots 17

Fig. 2.2-2 The reference Raman spectrum of Methanol [33] 17

Fig. 2.2-3 The experimental Raman spectrum of Teflon measured in a single shot, the measured peak frequencies are given for the main peaks with the expected reference Raman frequencies in brackets 18

Fig. 2.2- 4 The reference Raman spectrum of Teflon [29] 18

Fig. 2.3-1 The experimental Air (N2&O2) Raman spectrum 22

Chapter III FT UV Raman spectroscopy with a Sagnac Interferometer

Fig. 3-1 The schematic of FT Raman spectroscopy with a Sagnac interferometer 24

Fig. 3.1.1-1 UVHP Raman filter transmittance vs. wavelength 28

Fig. 3.1.1-2 UVHP Raman filter Optical Density vs. wavelength 28

Fig. 3.1.1-3 UVHP Raman filter transmittance vs. wave number 29

Fig. 3.1.1-4 UVHP Raman filter Optical density vs. wave number.....29

Fig. 3.1.2-1 The transmittance vs. wavelength for the UV dielectric mirror 31

Fig. 3.1.2-2 The Optical Density vs. wavelength for the UV dielectric mirror 31

Fig. 3.1.2-3 The filter transmittance vs. wave number for the UV dielectric mirror 32

Fig. 3.1.2-4 The Optical density vs. wave number for the UV dielectric mirror 32

Fig. 3.1.3 - 1 The transmittance vs. wavelength for the Liquid Filter 35

Fig. 3.1.3 – 2 The Optical Density vs. wavelength for the Liquid Filter 35

Fig. 3.1.3 - 3 The filter transmittance vs. wave number for the Liquid Filter 36

Fig. 3.1.3 – 4 The Optical density vs. wave number for the Liquid Filter 36

Fig. 3.1.4 – 1 The transmittance vs. wavelength of UV Beam Splitter 39

Fig. 3.1.4 - 2 The reflectance vs. wavelength of UV Beam Splitter 39

Fig. 3.1.4-3 The setup for the UV Beam Splitter transmittance and reflectance tests 40

Fig. 3.1.4 – 4 The transmittance and reflectance of the UV the Beam Splitter 40

Fig. 3.1.4-5 The setup for testing of the UV Beam Splitter surface reflection 41

Fig. 3.1.4 – 6 The surface reflections of the UV Beam Splitter 41

Fig. 3.1.5-1 The geometric layout of UV CCD 42

Fig. 3.1.5-2 The Dark Current of UV CCD 43

Fig. 3.1.5-3 The setup of the gain testing of UV CCD with a Tungsten lamp 47

Fig. 3.1.5-4 The spectral radiance of Tungsten lamp (EPT-1182) at 35Amperes 48

Fig. 3.1.5-4 The Quantum efficiency of the UV CCD camera as given by the anufacturer, Andor 48

Fig. 3.1.5-5 The transmittance vs. wavelength of each of the filters and the calculated combined filters transmission 48

Fig. 3.1.5-6 The setup for the responsivity calibration of the UV CCD camera with 266nm laser pulse 52

Fig. 3.2.1-1 The theoretical interference patterns of two coherent point light sources in a plane through the two sources 57

Fig. 3.2.1-2 The fringe pattern on an imaginary CCD 58

Fig. 3.2.1-3 The interference fringe pattern of two coherent point light sources 59

Fig. 3.2.2-1 The schematic diagram of a Sagnac interferometer 61

Fig. 3.2.2-2 The model of a Sagnac interferometer by T. Okamoto [21] 62

Fig. 3.2.2-3 The 3-D model of a Sagnac Interferometer 62

Fig. 3.2.2-4 The 2-D model of Sagnac Interferometer 63

Fig. 3.2.3-1 The fringe spacing and Fourier Transform spectra 69

Fig. 3.3-1 The Oriel Hg discharge lamp spectra measured with a spectrometer 71

Fig. 3.3.1-1 FT Hg spectra for the movable mirror at a position of 12.40 mm 73

Fig. 3.3.1-2 The 3-D plot of the FT Hg spectra vs. the position of the movable mirror 73

Fig. 3.3.1-3 Fringe spacing versus position of the movable mirror 74

Fig. 3.3.1-4 The resolution vs. the minimum measurable wavelength 75

Fig. 3.3.1-5 The resolution vs. the position of the movable mirror 75

Fig. 3.3.1-6 The comparison of the theoretical and the experimental results for the relation of mirror offset and fringe spacing 76

Fig. 3.3.2-1 FT Hg spectrum for a position (z = 12.230 mm) of the UV CCD camera 78

Fig. 3.3.2-2 The 3-D plot of the FT Hg spectrum vs. the position of UV CCD 78

Fig. 3.3.3-1 The wavelength calibration based on the single 253.65nm line of Hg lamp. Both a simple linear and a nonlinear fit (open) and error in calibration (solid) are shown 80

Fig. 3.3.3-2 The wavelength calibration by using a least squares fitting of the multiple-lines of the Hg lamp and lens aberration consideration 80

Fig. 3.3.4-1 Teflon Rayleigh and Raman fringe patterns from 266 nm laser pulse excitation 81

Fig. 3.3.4-2 The fringe visibility vs. the fringe spacing of single shot Teflon Rayleigh scattering 83

Fig. 3.3.4-3 The visibility vs. the fringe spacing of single shot Teflon Rayleigh scattering, the comparison of a single lens and a Doublet lens for s-polarized light 84

Fig. 3.4.1-1 The fringe pattern of Water and its FT Raman spectrum measured with the Sagnac interferometer (10,000 shots) and compared to its conventional Raman spectrum[33] 87

Fig. 3.4.2-1 The fringe patterns of Methanol and its FT Raman spectrum measured with the Sagnac interferometer (10,000 shots) and compared to its conventional Raman spectrum[33] 89

Fig. 3.4.2-2 The fringe patterns of Methanol and its FT Raman spectrum measured with the Sagnac interferometer (single shot) and compared to its conventional Raman spectrum[33] 91

Fig. 3.4.3-1 The fringe patterns of Cyclohexane & its FT Raman spectrum measured with the Sagnac interferometer (10,000 shots) and compared to its conventional Raman spectrum[33] 93

Fig. 3.4.4-1 The fringe patterns of Ethanol & its FT Raman spectrum measured with the Sagnac interferometer (10,000 shots) and compared to its conventional Raman spectrum[33] 95

Fig. 3.4.5-1 The fringe patterns of Air & its FT Raman spectrum measured with the Sagnac interferometer (16,000 shots) 97

Fig. 3.4.6-1 The fringe patterns of Teflon & its FT Raman spectrum measured with the Sagnac interferometer (1,000 shots) and compared to its conventional Raman spectrum 99

Fig. 3.4.6-2 The fringe patterns of Teflon & its FT Raman spectrum measured with a Sagnac interferometer(single shot) and compared to its conventional Raman spectrum 101

Fig. 3.4.6-3 8 overlaid single shot spectra of Teflon to demonstrate reproducibility ...102

Fig 3.5-1 Schematic diagram of the ray come for the solid angle that projects to a single pixel on the UV CCD camera 105

Chapter IV Other Applications of FT spectroscopy with a Sagnac Interferometer

Fig. 4.1-1 The experimental FT LIBS of Aluminum 6061 alloy for 1 mJ, laser pulses focused with a 250 mm focal length lens (single shot) 113

Fig. 4.1-2 The experimental LIF of green paper with laser energy 1mJ, 1000 shots and resolution 226 cm^{-1} 115

Fig. 4.1-3 The experimental LIF of black spruce with laser energy 1mJ, 1000 shots and resolution 113 cm^{-1}.....115

Chapter I

Introduction

The application of Raman spectroscopy as an analytical technique provides a method for chemical identification and for quantitative analysis. Raman spectroscopy, compared to other analytical techniques for chemical identification, has minimal requirements for sample preparation. Over the past decades, the technological developments, such as the laser, charge couple device (CCD) camera and Fourier Transform (FT) spectroscopy, have resulted in enormous increases in Raman signal detection capabilities, substantially less instrumentation costs and relatively compact equipment. These factors have led to a rapidly growing interest in Raman spectroscopy for chemical identification and for on-line monitoring and control of manufacturing processes.

Fourier Transform (FT) Raman Spectroscopy with a Sagnac Interferometer has attracted some attention in recent years [1-10]. The Sagnac interferometer generates an interferogram of Raman scattered light in the spatial domain and a Fourier Transform of this interferogram yields a frequency domain spectrum. This method has some distinct advantages over Raman spectroscopy with a dispersive spectrometer, such as throughput and multiplexing, which give high signal-to-noise ratio and allows the acquisition of the whole spectrum in a single data acquisition. It also has advantages over FT Raman Spectroscopy with a Michelson Interferometer [5, 8] that produces interferograms in time by the mechanical scanning of one mirror of the Michelson Interferometer. The

experimental setups for conventional, Michelson FT and Sagnac FT spectrometers are shown in Figs. 1-1, 1-2 and 1-3 respectively.

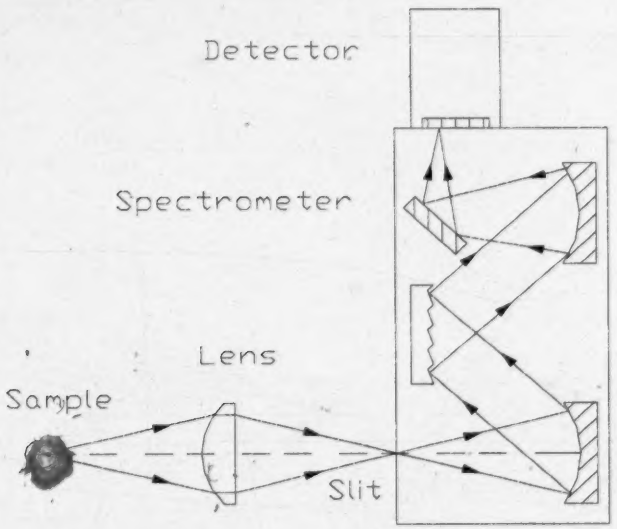

Fig. 1-1 The experimental setup of Raman spectroscopy with a grating spectrometer

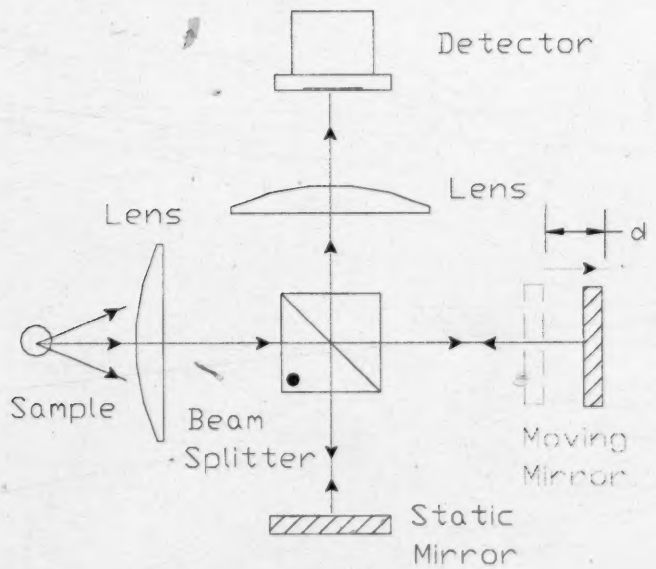

Fig. 1-2 The experimental setup of Raman spectroscopy with a Michelson interferometer

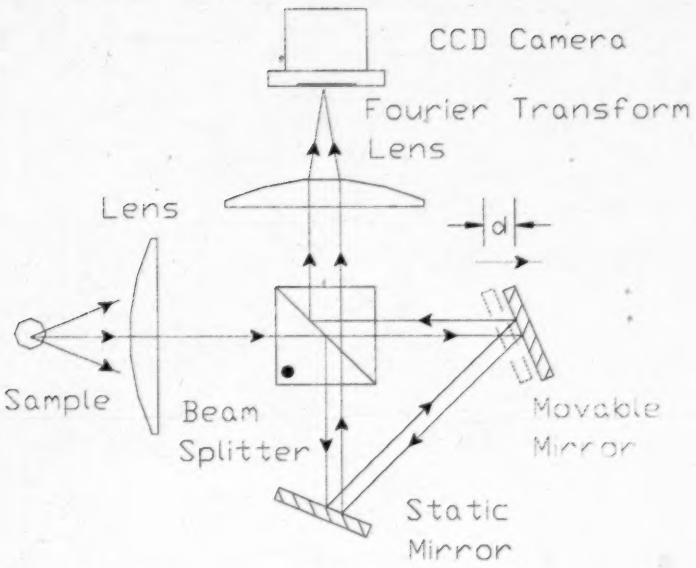

Fig. 1-3 The experimental setup of Raman spectroscopy with a Sagnac Interferometer

FT Raman Spectroscopy with a Sagnac Interferometer generates interferograms in space which are recorded by a detector array. Because the Sagnac interferometer has no scanning motion, many of the mechanical problems associated with a scanning mirror in the Michelson interferometers can be avoided and the instrumentation can be less expensive and simpler. Unlike Scanning FT spectrometers, this static FT spectrometer obtains the full interferogram at once. Under the single shot conditions, because it is not sensitive to changes in the sample during the measurement period, time-resolved spectroscopy can be achieved.

An Ultra-Violet exciting laser can help avoid the interference between the fluorescence and the useful Raman spectra. Because of the relative weakness of a Raman signal, the fluorescence can totally obscure a normal Raman spectrum. Since most

fluorescence occurs between 270nm and 700nm, the wavelength of the exciting laser in this range has to be chosen with extreme care and will depend on the sample being measured. By selecting a suitable wavelength for the excitation source, either in the near IR longer than 700nm or in the UV shorter than 270nm, the overlap of Raman and fluorescence spectra can be avoided. Because the Raman scattering cross-section scales as λ^{-4} of the exciting laser, UV lasers give over an order of magnitude larger Raman signal [24]. FT UV Raman Spectroscopy with a Sagnac interferometer can take advantage of the wavelength scaling by choosing a Raman exciting wavelength at 266nm (the 4th harmonic Nd:YAG laser wavelength) or shorter wavelengths.

The resolution of a FT Raman Sagnac Interferometer in wave numbers is given by $\Delta\sigma = \frac{2\sigma_{max}}{N}$, in which N is the number of pixels in a row of the detector array $\sigma_{max} = \frac{1}{\lambda_{min}}$ and λ_{min} is the shortest wavelength which can be measured. Thus, more pixels in a row of the detector or longer λ_{min} will give better resolution. For FT UV Raman spectroscopy with a Sagnac interferometer, λ_{min} should equal to or be a little bit greater than the wavelength of the exciting laser if one wants to get the best resolution. The spectra in the wavelength range shorter than λ_{min} must be blocked off by a filter, otherwise they will show up and interfere with the real spectra. Ivanov [1] introduced a method of using both row and column pixels of the 2-D detector array in order to achieve better resolution by a large pixel number N, instead of using only rows, in his static FT spectrometer based on a Michelson interferometer. The entire interferogram is folded into a series of partial interferograms along separate rows on the 2-D detector array by a

stepped profile mirror and a tilted mirror. The original spectrum can then be retrieved by applying the Fourier transform to the reconstructed inerferogram which is merged together from the folded interferograms.

How to block Rayleigh scattering while detecting Raman scattering is a bigger issue in a FT Raman spectrometer than in Raman spectroscopy with a dispersive spectrometer, since both Rayleigh and Raman scattering go to the detector in the former case while they are separated by the spectrometer in the latter one. A reflective mirror, an absorbing liquid filter and a long pass interference filter have been successfully used to block the scattered Rayleigh radiation and transmit the Raman scattered radiation in the present experiments. A reflective mirror has the advantage of selecting the cut off wavelength in a certain range by changing the incident angle. A liquid filter, Fluorobenzene diluted in cyclohexane, is first reported in this project behaving as a long pass filter with a cut off wavelength at 266nm. It is inexpensive and its optical density can be adjusted by changing its concentration. The interference filter is efficient but expensive and has to be specially procured for the required wavelength.

In order to compare the performance of a FT Raman Spectrometer based on a Sagnac Interferometer to a conventional Raman spectroscopy, a dispersive spectrometer was successfully built and used to measure selected samples, such as air, methanol and Teflon. A theoretical analysis of the measured strength of the N_2 Raman spectrum was carried out to estimate the instrumental efficiency. This efficiency was compared to that of the Sagnac interferometer.

The visibility of the interference pattern of Raman signals, defined by $\frac{I_{max} - I_{min}}{I_{max} + I_{min}}$, is one of the factors which determines the signal-to-noise ratio of a FT Raman spectrum. It is a function of pixels per fringe cycle when the interference pattern is formed by a single wavelength input signal. The visibility is constant for a small spatial frequency and decreases at some point when the pixels per cycle approaches the Nyquist limit of two pixels per cycle. The reason for the degradation comes from the aberration of the FT lens and the optical sampling geometry. Because the spectral resolution improves as the pixels per cycle decrease, there is a trade off between the S/N ratio and the spectral resolution when choosing the number of pixels per cycle. In addition, optical aberrations may lead to phase distortion across the spatial interferogram leading to a loss of spectral resolution and substructure in the reconstructed spectrum.

The configuration of the Sagnac interferometer is carefully studied in terms of a model based on geometric optics. The UV CCD camera should be located at the plane of maximum overlap, a concept that was introduced by S. Chakrabarti [23]. It is shown that the plane of maximum overlap is at the focal plane of FT lens for our configuration, while these two planes are at different locations in the model of S. Chakrabarti.

FT Raman spectra must be calibrated in terms of wave number or wavelength from its response to monochromatic radiation from calibration light sources. Laser radiation, Rayleigh scattering or spectral lines from a Hg Lamp can be applied for this purpose. When using a simple singlet lens, the wave number or the wavelength

calibration can't be done by simply calibrating the response with a single known wavelength as might be expected in an ideal situation because of the chromatic aberration of lens. Once the dependence of the refractive index as a function of the wavelength is taken into consideration, the wave number or the wavelength calibration matches the standard spectrum very well. Once the system is calibrated, the calibration can be used until the position of the movable mirror of the Sagnac interferometer is moved for some reason.

The objective of the present study was to build and study a Fourier Transform Ultra-Violet Raman Spectrometer based on a Sagnac Interferometer and demonstrate that it can be a useful tool to diagnose materials. The complete system is studied in detail, including the calibration of the optical components, a geometric optics analysis of the system, the wavelength calibration, the resolution limitation and the fringe visibility. After calibration, FT Raman spectra were obtained of a number of samples. It is shown that single shot Raman spectra can be obtained by using this system, which means that time-resolved single shot Raman spectroscopy is feasible.

Without any modification, this setup can also be applied to other spectral applications, such as Laser Induced Breakdown Spectroscopy (LIBS) and Laser Induced Fluorescence (LIF) which are also very useful diagnostic technologies. When LIBS and LIF are carried out with Fourier Transform Spectroscopy using a Sagnac Interferometer, they will have the same advantages as Raman spectroscopy does.

This thesis is organized as following, Chapter I is an Introduction. In Chapter II, Raman spectroscopy with a normal grating spectrometer is presented. This includes the experimental setup and procedures, experimental results and discussion, and theoretical calculations compared with the experimental results. Chapter III deals with Fourier Transform Ultra-Violet Raman spectroscopy using a Sagnac interferometer. The calibration of optical components, the theoretical model, the experimental setup/procedures, the characteristics of a Sagnac interferometer, and the experimental results are given in this chapter. Chapter IV demonstrates other applications of FT UV spectroscopy with a Sagnac interferometer, such as LIBS and LIF. Chapter V presents the discussion and conclusions for this project. The reference papers are listed under References. Finally, Appendices A, B and C give detailed background information relating to this project.

Chapter II

Raman Spectroscopy with a Grating Spectrometer

Before Fourier Transform Ultra-Violet Raman spectroscopy with a Sagnac interferometer was studied, Raman spectra of the selected samples were obtained by the conventional method of Raman spectroscopy with a grating spectrometer.

Section 2.1 Experimental setup and procedure

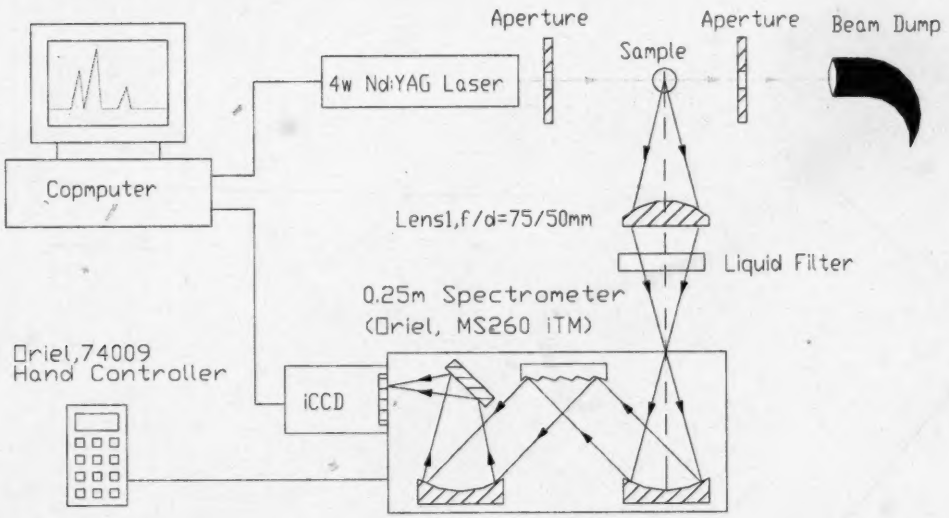

Fig. 2.1 – 1 The experimental setup of Raman spectroscopy with a grating spectrometer

The setup for Raman spectroscopy with a grating spectrometer is shown schematically in Figure 2.1-1. The laser source is a frequency-quadrupled Nd:YAG laser (Big Sky Laser Inc. ULTRA CFR, 266nm, 20Hz, 6nS, 6 mJ, horizontally polarized). The

spectrometer is an imaging ¼ m spectrograph (Oriel Instruments, MS 260i™, Model 74050/74055) with an input F/number of 3.9, a resolution of 0.15 nm with a 1200 l/mm grating and a 25 μm wide by 3 mm high input slit. The MS 260i™ spectrometer features an asymmetrical in-plane Czerny-Turner optical configuration. The detector used in this experiment is an intensified CCD (i-CCD) camera (Andor i-Star720) for low-light level spectroscopy application requiring fast gating. The camera has 1024 pixels in width and 256 pixels in height, an active pixel size of 26 μm by 26μm, and a minimum optical gate width 2ns. The gain can be adjusted over a range of 1 to 255 corresponding to responsivities of 0.5 to 600 counts per photon respectively. Both a short wavelength cutoff dielectric mirror and a liquid filter were used as Raman filters whose calibrations are discussed in Section 3.1.2 and Section 3.1.3. The scattered light is collected with a quartz lens, 75mm focal length and 50 mm in diameter. The Raman spectra are recorded with a program supplied with the i-CCD camera.

The experimental arrangement is shown in Figure 2.1-1. The location of the sample is determined by the imaging properties of the collecting lens. A simple plano-convex fused silica lens with 75 mm focal length and 25.4 mm diameter is placed in front of the slit of spectrometer. The lens is placed to match the acceptance angle of the spectrometer. The distance from slit to the lens equals

$$S_2 = (F/number\ of\ the\ spectrometer) \times (the\ effective\ diameter\ of\ the\ collecting\ lens, at\ 95\%\ of\ the\ full\ diameter) \quad (2.1\text{-}1)$$

$$= 3.9 * 25.4 * 95\%$$

$$= 94 \text{ mm.}$$

While the visible focal length is 75 mm, the actual focal length at a wavelength of 266nm is different than the nominal focal length and can be calculated from the refractive index as a function of wavelength [31].

$$n^2 - 1 = \frac{0.6961663\lambda^2}{\lambda^2 - 0.0684043^2} + \frac{0.4079426\lambda^2}{\lambda^2 - 0.1162414^2} + \frac{0.8974794\lambda^2}{\lambda^2 - 9.896161^2} \qquad (2.1\text{-}2)$$

where λ is the wavelength in microns and n is refractive index. The focal length can then be calculated from the Lens Maker's formula [32]

$$\frac{1}{f} = (n-1)\left(\frac{1}{r_1} - \frac{1}{r_2}\right) \qquad (2.1\text{-}3)$$

Inserting r_1 = 34.5mm, r_2 = ∞ (the curvatures of the lens surfaces given by the manufacturer, Melles Griot) and λ = 266 nm, one can get f = 68 mm. The imaging formula for the lens is given by

$$\frac{1}{f} = \frac{1}{S_1} + \frac{1}{S_2} \qquad (2.1\text{-}4)$$

where S1 and S2 are the distances from the lens to the object and image planes, respectively. Using S2 = 94 mm and f = 68 mm one can calculate S_1 = 250 mm and this is used as the distance from sample to the collecting lens. Thus the image of the source region is demagnified by a factor of 0.38 times onto the entrance slit of the spectrograph.

The laser beam is perpendicular to the optical axis of the collecting lens, interacting with the sample at the crossing point. Two apertures are used for alignment. A beam dump blocks the transmitted light when liquid samples are used. A filter to

block the fundamental light and transmit the Raman light, either mirror or liquid filter, is put between the collecting lens and spectrometer. The iCCD camera is synchronized with the triggering pulse from Nd:YAG laser.

Careful alignment of the optical components must be carried out before running the experiments. Rayleigh scattering in air is used for this purpose because its signal is much bigger than the Raman scattering. In Figure 2.1-1, when the laser fires in air, both Rayleigh and Raman scattering are collected by the collecting lens into spectrometer where the iCCD camera detects these signals. For alignment the iCCD camera is operated in the image mode. The image of Rayleigh scattered light on the iCCD camera is a rectangle and its size depends on the height and width of the slit. By looking at this image of Rayleigh scattering and adjusting the collecting lens in 3 dimension, the image can be centered on the camera and maximum signal can be obtained. This is the optimum positions for all optical components.

After optimizing the Rayleigh scattering, the spectrometer is turned to a center wavelength which can view the Raman spectra while keeping Rayleigh scattering out of the iCCD camera. Fluorescence often accompanies Raman spectra, and there is the possibility that fluorescence may come from the container when liquid samples are used. Thus, air is suggested as a good sample to overcome this problem because no container is involved although its Raman signals are weak.

Figure 2.1- 2 shows a Raman spectra of air without filters. Rayleigh scatting is weak because it is cut by the end of the range of the spectrograph. There is scattered light in the range from 250 cm^{-1} to 1200 cm^{-1} and from 2600 cm^{-1} to 4000 cm^{-1} and these signals must be eliminated because they seriously contaminate the useful signals. The scattered light is most likely Rayleigh light scattering inside spectrometer. When the Raman filter, whether interference mirror or liquid filter, is introduced, these scattered light signals disappear. The Raman spectrum of air using a liquid filter of Fluorobenzene diluted in Cyclohexane is shown in Figure 2.1-3. The effect of Raman filter in blocking Raleigh scattered light can be seen by comparing Figure 2.1-2 with Figure 2.1-3.

The center wavelength was calibrated by measuring the Rayleigh scattering from air with excitation by the 4^{th} harmonic Nd:YAG laser at 266 nm. The pixels per nm calibration was then determined by moving the center wavelength of the spectrometer by a fixed amount, of the order of 20nm, and noting the shift in the Rayleigh scattering peak on the CCD Camera. Thus, the pixel channels on iCCD camera can be converted to wave numbers.

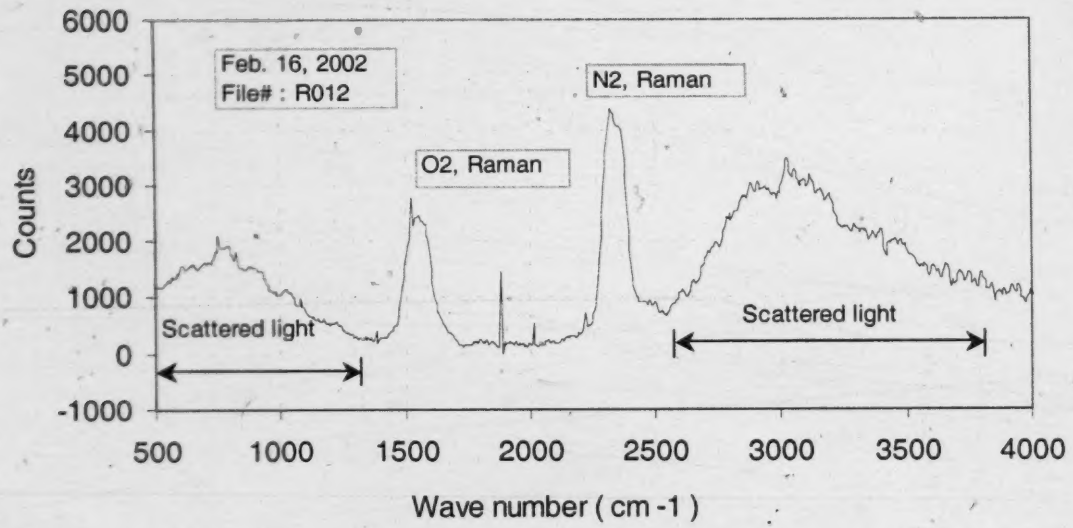

Fig. 2.1- 2 The experimental Raman spectrum of air with some stray scattered light, excited by 4th harmonic Nd:YAG at 266 nm

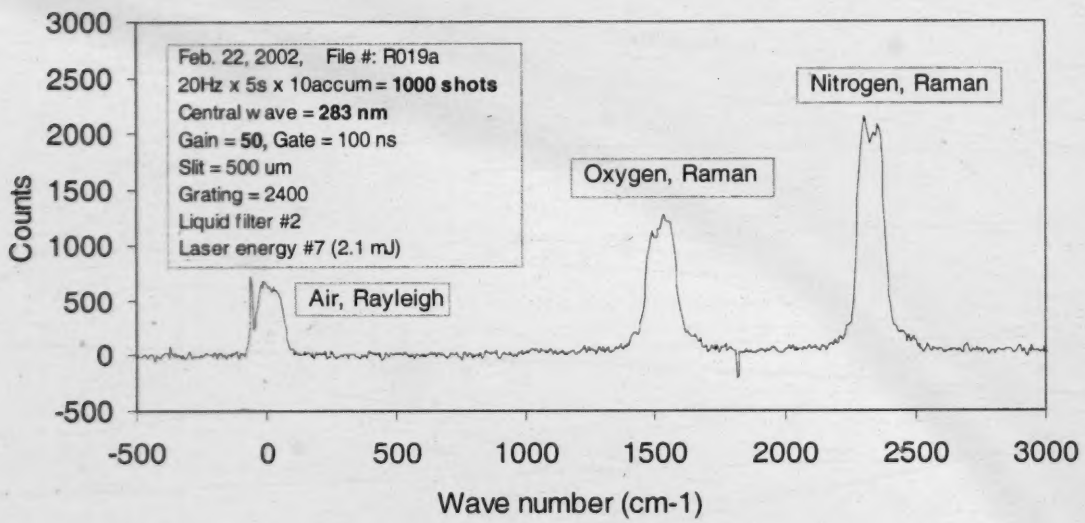

Fig. 2.1- 3 The experimental Raman and Rayleigh spectrum of air accumulated over 1000 shots using the liquid filter to block the Rayleigh signal

Section 2.2 Experimental results

Raman spectra of air, methanol and Teflon are selected to represent gas, liquid and solid samples. The measured Raman spectrum of air is shown in Figure 2.1-3. The laser energy was 2.1 mJ and the repetition rate was 20 Hz. The spectrometer was set at a center wavelength of 283 nm, a 2400 g/mm grating was used and the slit width was 200 μm with a resolution of 11.8 cm^{-1}. The iCCD camera was set at a gain of 50 out of 255 and a gate time of 100ns, center track / track height of the readout mode was 135 / 70 and the exposure time was 5s. Ten accumulations were summed to give a total of 1000 shots integrated for the final spectrum. Liquid filter #2 (as described in section 3.1.3) was used to block the Rayleigh scattering. Rayleigh scattering of air was used as a wavelength calibration at 266nm. Based on the spectral calibration, the measured Raman scattering of Oxygen and Nitrogen are at 1530±12 cm^{-1} and 2326±11 cm^{-1}, respectively. These experimental Raman shift wave number match those from the literature of 1556 cm^{-1} for Oxygen and 2331 cm^{-1} for Nitrogen within 2%.

Next, a Raman spectrum of a liquid sample, methanol, was measured. The measured Raman spectrum of methanol is shown in Figure 2.2-1. Figure 2.2-2 is a reference Raman spectrum of methanol taken from a reference database[33]. The laser energy was 2.1 mJ and the repetition rate was 20 Hz. The spectrometer was set at a center wavelength of 283 nm, a 2400 g/mm grating was used and slit width was 100 μm. The iCCD camera was set at a gain of 1 out of 255 and a gate time of 100ns, center track / track height of the readout mode was 150 / 100 and the exposure time was 2s. Ten

accumulations were summed to give a total of 400 shots integrated for the final spectrum. The Raman filter used was the interference mirror at a 40 degree angle. Rayleigh scattering of air was used as a wavelength calibration at 266nm. The measured experimental Raman shifts of methanol are 2996 ± 42 cm^{-1}, 2890 ± 41 cm^{-1} and 1489 cm^{-1} matching 2946 cm^{-1}, 2836 cm^{-1} and 1453 cm^{-1} from the reference literature within 2%. The reason that Raman line at 1037 cm^{-1} does not show up is due to the low transmittance of the Raman filter at this wavelength.

A Raman spectrum was also taken of a solid sample, Teflon. The Teflon Raman spectrum with a single laser shot is shown in Figure 2.2-3 and a reference Teflon spectrum is in Figure 2.2-4 [29]. As a solid sample, Teflon has a much larger number density than the gas sample leading to much larger signals. The laser energy was 2.1 mJ and the iCCD camera was triggered at real time. The spectrometer was set at a center wavelength of 274 nm, a 2400 g/mm grating was used and the slit width was 100 μm. The iCCD camera was set at a gain of 1 out of 255 and a gate time of 100ns, center track / track height of the readout mode was 135 / 70. The spectrum shown corresponds to a single laser shot. Liquid filter #2 was used to block the Rayleigh scattering. Several features of the Raman spectra for Teflon are found: Symmetric F-C-F stretching mode at 736 ± 17 cm^{-1}, Anti-symmetric F-C-F stretching mode at 1234 ± 28 cm^{-1}, C-C stretching modes at 1317 ± 21 cm^{-1} and 1395 ± 22 cm^{-1}. All these Raman lines match their corresponding ones from literature within 2% as shown in Figure 2.2-3, although the intensities are slightly different due to the transmission variation of the Raman filter and poorer spectral resolution of the measured spectrum compared to the reference spectrum.

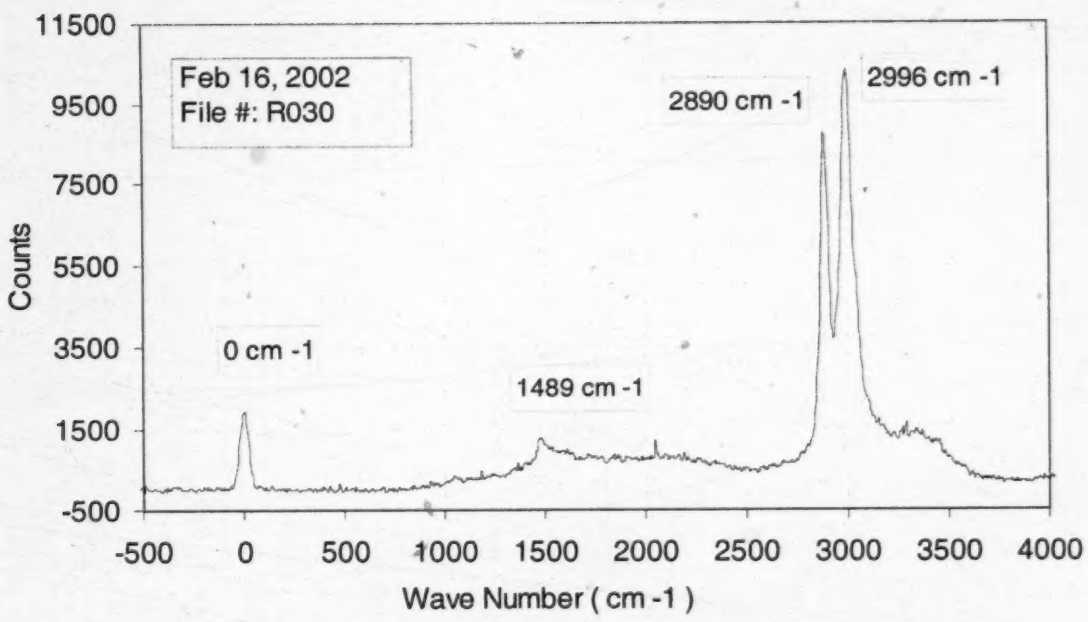

Fig. 2.2 – 1 The experimental Raman spectrum of Methanol, 400 shots

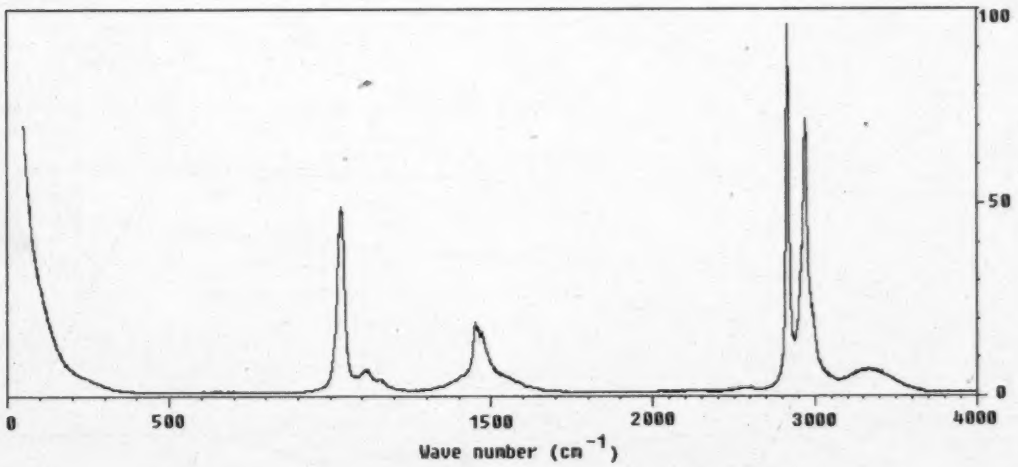

Fig. 2.2 – 2 The reference Raman spectrum of Methanol [33]

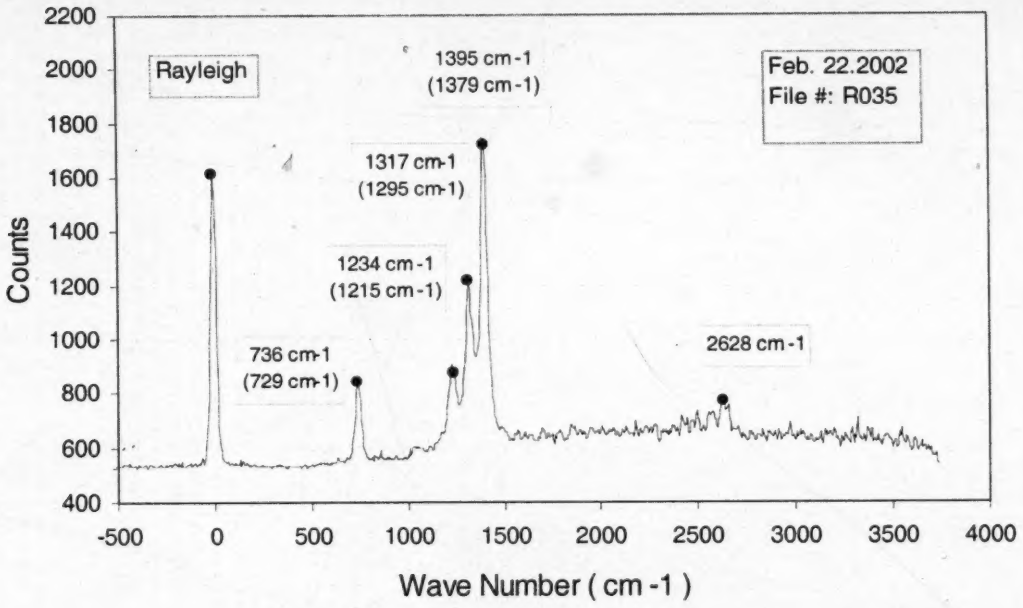

Fig. 2.2- 3 The experimental Raman spectrum of Teflon measured in a single shot, the measured peak frequencies are given for the main peaks with the expected reference Raman frequencies in brackets.

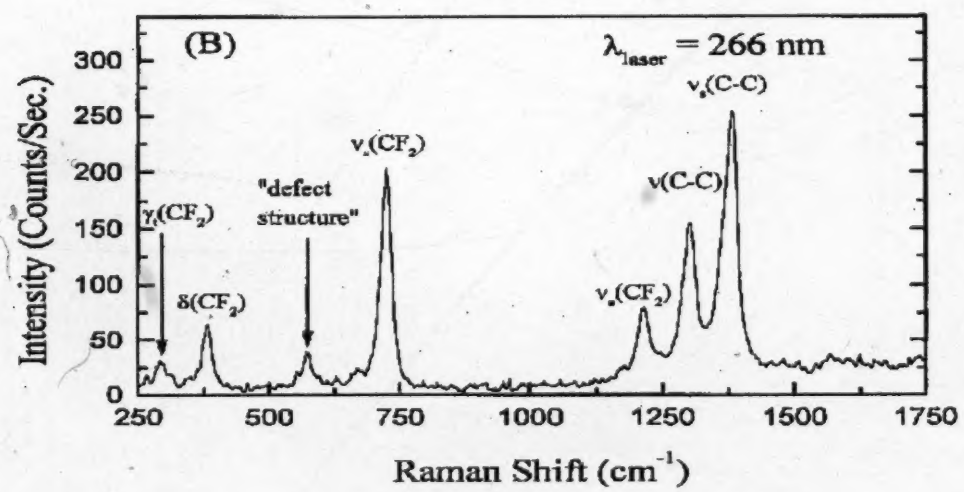

Fig. 2.2- 4 The reference Raman spectrum of Teflon [29]

Section 2.3 Theoretical calculation of Raman spectrum of Nitrogen

In order to estimate the overall efficiency of the grating instrument for Raman spectroscopy, a theoretical calculation was carried out of the expected energy of the Raman radiation on the surface of the i-CCD Camera [24].

$$E_{Raman\ of\ N_2} = T \times (\frac{N}{V})_{N_2} \times (\frac{d\sigma}{d\Omega})_{N_2} \times L_{N_2} \times E_{Laser} \times \frac{h\nu_{Raman}}{h\nu_{Pump}} \times \Omega \qquad (2.3\text{-}1)$$

where T is the transmittance of the optical components between the sample and the i-CCD camera which consists of the liquid filter, the collecting lens, concave mirror, grating and concave mirror given by.

$$T = T_{Liquid\ Filter} \times T_{Lens} \times T_{Concave\ Mirror} \times T_{Grating} \times T_{Concave\ Mirror} \qquad (2.3\text{-}2)$$

$$= 89\% \times 90\% \times 90\% \times 80\% \times 90\%$$
$$= 51.9\%$$

$(\frac{N}{V})_{N_2}$ is the concentration of Nitrogen at the room temperature 24.2 °C and 700 mmHg atmosphere which is 78% of the molecular density of air given by:

$$(\frac{N}{V})_{Air} = \frac{PV}{RT} = \frac{(700/760)atm \times 6.033 \times 10^{23} mol^{-1}}{0.08206 L.atm/mol^{-1} \times 301.2K} \qquad (2.3\text{-}3)$$

$$(\frac{N}{V})_{N_2} = 78\% \times (\frac{N}{V})_{Air} = 1.75 \times 10^{19} molecular.cm^{-3}$$

$(\frac{d\sigma}{d\Omega})_{N_2}$ is the differential cross section of Raman scattering of nitrogen for 266 nm exciting laser wavelength which is taken from ref [24] as:

$$(\frac{d\sigma}{d\Omega})_{N_2} = 7.73 \times 10^{-30} \frac{cm^2}{Sr} \qquad (2.3\text{-}4)$$

L_{N_2} is the observed interaction length of Raman scattering which is calculated by considering the lens magnification and the slit width of the Oriel spectrometer. In Section 2.1, the objective distance is 250mm and the imaging distance is 94mm by theoretical calculation. In the experimental measurement, the actual distance from sample to the collecting lens is 241 mm while the distance from the collecting lens to the slit is 88 mm. The slit width of the spectrometer is 500 μm giving the observed interactive length as:

$$L_{N_2} = 500\mu m \times \frac{241mm}{88mm} = 0.1369\ cm \tag{2.3-5}$$

E_{Laser} is the total laser energy at 20Hz, 2.1 mJ and 10 accumulations of 5 seconds each giving

$$E_{Laser} = 20 \times 10 \times 5 \times 2.1\ mJ = 2.1\ J \tag{2.3-6}$$

Ω is the solid angle of the collecting lens with 75 mm focal length and diameter 25.4 mm. Raman scattering is collected by this lens at a distance of 241 mm. Because the lens holder covers part of lens, we may assume an effective diameter of 95% of 25.4mm. So, the collecting solid angle is

$$\Omega = \frac{\pi \times (\frac{95\% \times \Phi}{2})^2}{d^2} = \frac{\pi \times (\frac{95\% \times 25.4}{2})^2}{241^2} = 7.9 \times 10^{-3}\ Steridian \tag{2.3-7}$$

But, the F# of the collecting lens is 3.6 ($F\# = \frac{88mm}{(25.4mm \times 95\%)} = 3.6$) which is smaller than the F# of spectrometer, 3.9. Thus, some of light can't get through the spectrometer and the solid angle of the light which can reach detector is then given by

$$\Omega = \Omega' \times \left(\frac{3.6}{3.9}\right)^2 = 6.71\times10^{-3}\ Steridian \qquad (2.3\text{-}8)$$

The energy of Raman scattering of N_2 is

$$E_{Raman\ of\ N_2} = T\times(\frac{N}{V})_{N_2}\times(\frac{d\sigma}{d\Omega})_{N_2}\times L_{N_2}\times E_{Laser}\times\frac{h\nu_{Raman}}{h\nu_{Pump}}\times\Omega \qquad (2.3\text{-}9)$$

$$= 51.90\%\times1.75\times10^{19}\times7.73\times10^{-30}\times0.13594\times2.1\times\frac{266}{283.6}\times6.71\times10^{-3}$$

$$= 1.27\times10^{-13}\ J$$

The Raman shift of N_2 is 2331 cm $^{-1}$ and the corresponding wavelength is 283.6 nm for an exciting laser wavelength of 266 nm. The energy of one photon of N_2 Raman scattering is then

$$E_{onephoton} = \frac{hc}{\lambda} = \frac{6.626\times10^{-34}\times3\times10^{8}}{283.6} = 7.01\times10^{-19}\,J \qquad (2.3\text{-}10)$$

The experimentally measured raw Raman spectrum for air is shown in Figure 2.3-1. It can be seen that the full width at half maximum (FWHW) is $N_{channels}$= 21 channels on the i-CCD contributing to the Raman spectrum of N_2. With the gain of 50, the Andor specification is C_{photon}= 1.2 counts per photoelectron. Also the quantum efficiency is given as $Q_{efficiency}$= 15%. Thus, the theoretically calculated counts per channel of the Raman signal expected for N_2 is

$$Counts_{Raman\ of\ N_2} = \frac{E_{Raman\ of\ N_2}}{E_{one\ photon\ Raman}}\times C_{photon}\times Q_{efficiency}\times\frac{1}{N_{Channels}} \qquad (2.3\text{-}11)$$

$$= \frac{1.27\times10^{-13}}{7.01\times10^{-19}}\times1.2\times0.15\times\frac{1}{21}$$

$$= 1554\ Counts$$

The reading from the experimental result in Figure 2.3-1 gives 2000 counts. So, the difference between the theoretical calculation and the experimental result is approximately 22%. Given all the approximate values used in the above calculation, the theoretical cross-section is in good agreement with the experimental results. A summary of these calculations is given in Table 2.3-1.

The experiments conducted with the grating spectrometer thus confirmed the expected spectra and overall spectral efficiency for a standard Raman spectrometer. These results are then compared to results obtained with the Sagnac interferometer system as described in the next chapter.

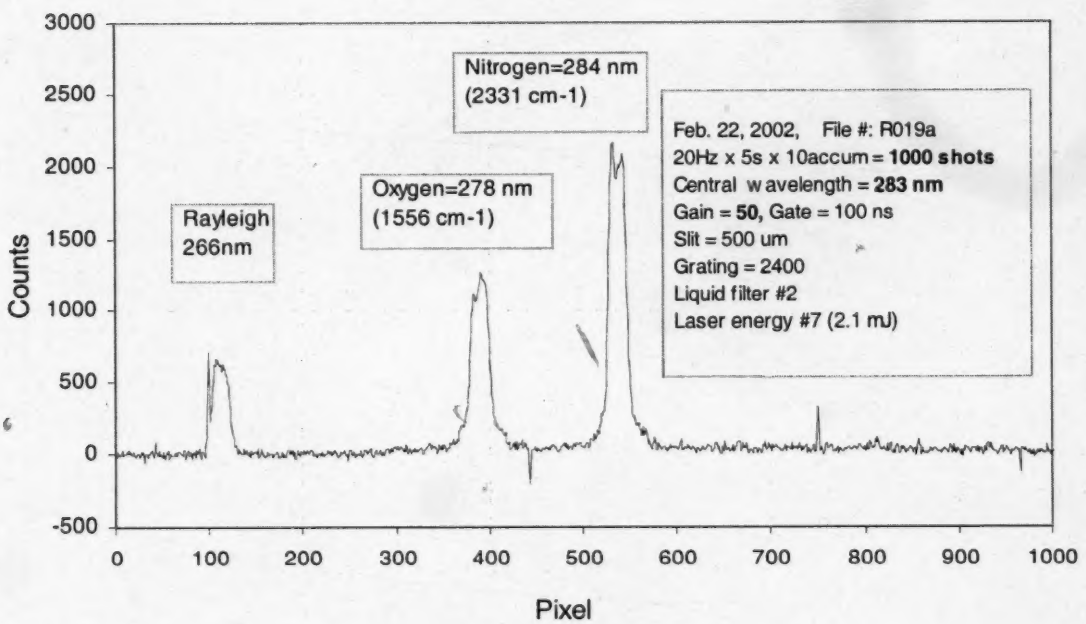

Fig. 2.3 – 1 The experimental air (N_2&O_2) Raman spectrum

Summary of the theoretical calculation and the experimental results	
Transmittance of Optical Components	51.9%
N2 concentration (molecular.cm - 3)	1.75×10^{19}
Cross section of N2 (cm2 / Sr)	7.73×10^{-30}
Interaction length of Raman (cm)	0.14
Laser Energy (J)	2.1
Collection Solid Angle	6.71×10^{-03}
Energy of Raman Signal on the i-CCD of N2 (J)	1.27×10^{-13}
Energy of one photon of Raman of N2 @ 283.6 nm (J)	7.01×10^{-19}
Photons of Raman N2 per channel of OMA	8633
Counts / photons @ (Gain = 50)	1.2
Quatum Efficency of OMA	15%
Counts of Raman of N2 expected theorerically(counts)	1554
Experimental result of Raman of N2 (counts)	2000
Error between theretical calculation and experiment	-22%

Table 2.3 –1 The summary of theoretical calculation of N_2 Raman signal

Chapter III

FT UV Raman Spectroscopy with a Sagnac Interferometer

Figure 3-1 is the schematic diagram of the layout for carrying out FT Raman Spectroscopy with a Sagnac interferometer. The setup consists of a 4th harmonic Nd:YAG laser (Big Sky model ULTRA CFR), a number of diaphragms, a Raman filter, a collecting lens, a beam splitter cube, a movable mirror, a static mirror, a Fourier Transform lens, a UV CCD and a computer. All these optical components are aligned by a pencil type of 532nm Nd:YAG laser. A black painted beam dump blocks the stray laser light for transmitting samples.

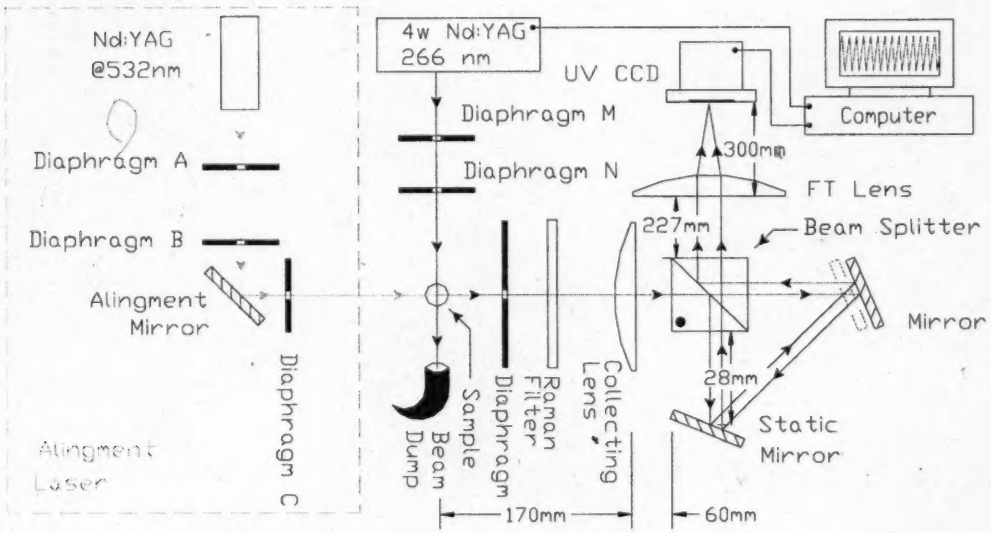

Fig. 3-1 The schematic of FT Raman spectroscopy with a Sagnac interferometer

A 4th harmonic Nd:YAG laser system (ULTRA CFR) working at 266 nm is used as the exciting laser for the Raman spectroscopy. We will simply refer to it as the 4ω Nd:YAG laser from now on. The company claims that this laser can give 6 mJ at 266 nm with a horizontal polarization and the maximum repetition frequency can be up to 20 Hz with a pulse width of 6 ns. The Raman filter is used to block Rayleigh scattering and transmit Raman scattering. It was purchased from Barr Associates, Inc. and was carefully calibrated as described in Section 3.1.1. The collecting lens has a 75mm focal length and a 50mm diameter, while the FT lens has a 300 mm focal length and a 50mm diameter. Both of them are plano-convex lenses made of UV fused silica. They were purchased from THORLAB Inc. with the catalog number LA4078 for the 75mm focal length and LA4855 for the 300mm focal length, respectively. The reflective mirrors are UV MAXBRIte™ (/007) ordered from Melles Griot with the catalog number 02 MLQ 003/007. They are square in shape, 25.0 mm by 25.0 mm and 6 mm thick. The substrates are made of Synthetic fused silica with a specified flatness $\lambda/10$ (λ = 632.8nm) and the surface is coated with a multilayer all-dielectric broadband coating, which gives an average reflection greater than 98% from 245 nm to 390nm @ 0-45° angle of incidence. The UV beam splitter is also a product of Melles Griot and was calibrated in our lab with details given in Section 3.1.4. The UV CCD camera (Model DU 440-BU2, 2492) [36] is a product of Andor Technology Limited and its detailed calibrations can be found in Section 3.1.5. A computer is used to drive the UV CCD camera and to trigger the laser. In some cases it is triggered by the laser depending on different experimental requirements. The pictures of the experimental setup are attached in Appendix A. The alignment of the Sagnac Interferometer is described in detail in Appendix B.

The fringe pattern is then recorded by using the software of Andor Technology Limited and data is saved as ASCII files. The Fourier Transform analysis is carried out by a program written in Matlab 5.3. Details on the codes are given in Appendix C.

Section 3.1 The calibration of the optical components

In order to make sure the optical components of the Sagnac interferometer work properly, they have to be calibrated and compared to their specifications. The main optical components include the Raman filters, UV beam splitter and UV CCD camera.

Three types of filters, UV high pass filter, dielectric mirror and a liquid filter, were calibrated to make sure that they can block the Rayleigh scattering and pass the Raman signal. The UV beam splitter was tested for transmittance, reflectance and the surface reflections for both s-polarization and p-polarization. The UV CCD camera was tested for the readout noise, the dark current and the responsivity. Three different calibrated sources were used: a Tungsten Lamp, a 4ω Nd:YAG laser and a mercury lamp. The results of the calibrations are given in the following sections.

3.1.1 Calibration of UV Raman Filters @ 266nm

Three UV high pass Raman filters (UVHP) were ordered from Barr Associates, Inc[34]. The company claims that these 1.0 inch diameter interference filters can give transmittance greater than 50% on average from 270nm to 290nm and block greater than Optical Density 4 with a designed goal Optical Density 5 at 266nm for normal incident beams.

These filters were measured with the Perkin Elmer Lambda 900 Spectrophotometer at the NanoFab in the University of Alberta. The transmittance and the Optical Density vs. wavelength at the different angles of incidence are shown in Figures 3.1.1-1 and 3.1.1-2. It can be seen that the transmittance curves of the filters match the specification except that the transmittance is lower than 50% @270nm. The blocking curve shifts to shorter wavelength as the incident angle increases. Taking advantage of this, a proper angle is available that the Rayleigh scattering can be effectively attenuated with O.D. > 4 while the low frequency Raman information still can be obtained with transmittance > 50% at 500 cm^{-1} as shown in Figures 3.1.1-3 and 3.1.1-4.

Also, these filters can be used as the long pass filters for an exciting wavelength of 248nm (KrF laser) when they are placed at 45 degrees.

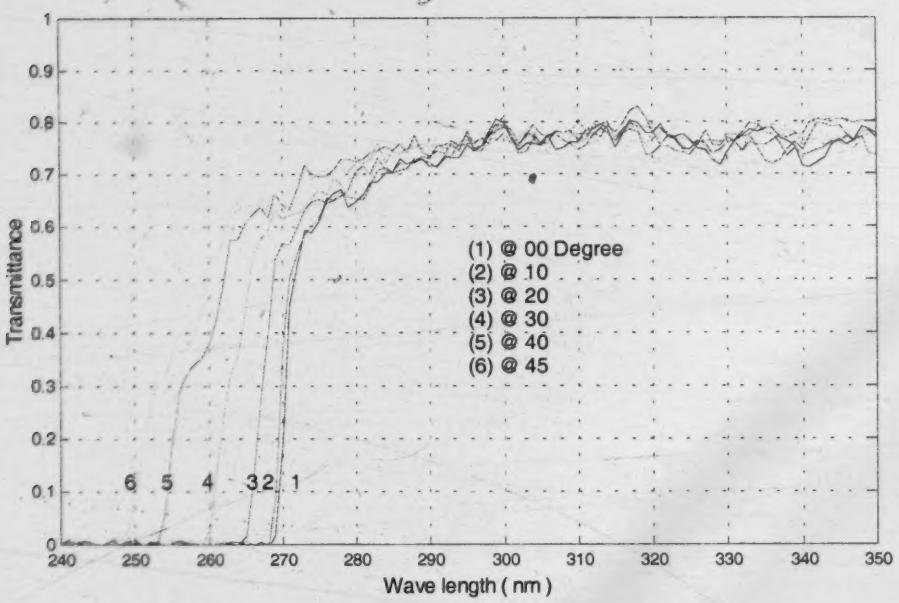

Fig. 3.1.1-1 UVHP Raman filter transmittance vs. wavelength

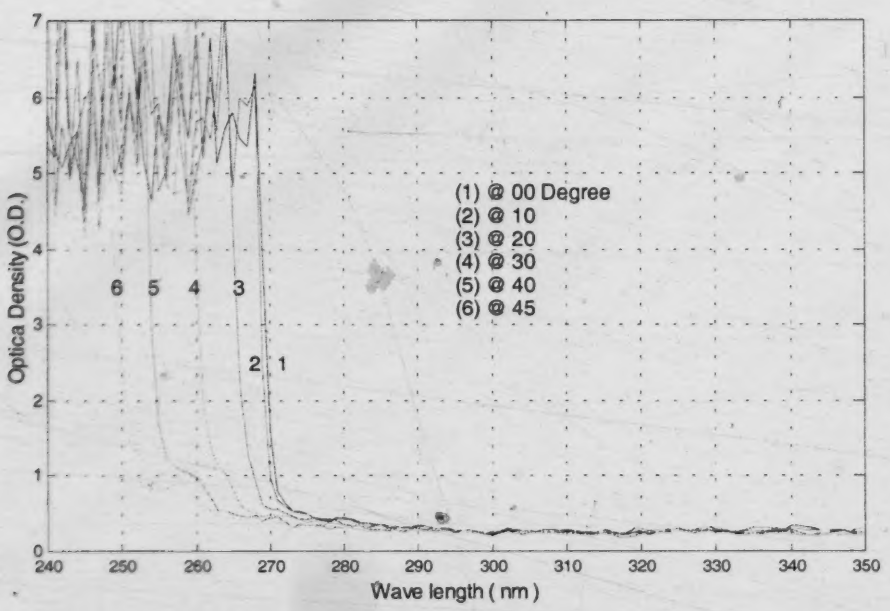

Fig. 3.1.1-2 UVHP Raman filter Optical Density vs. wavelength

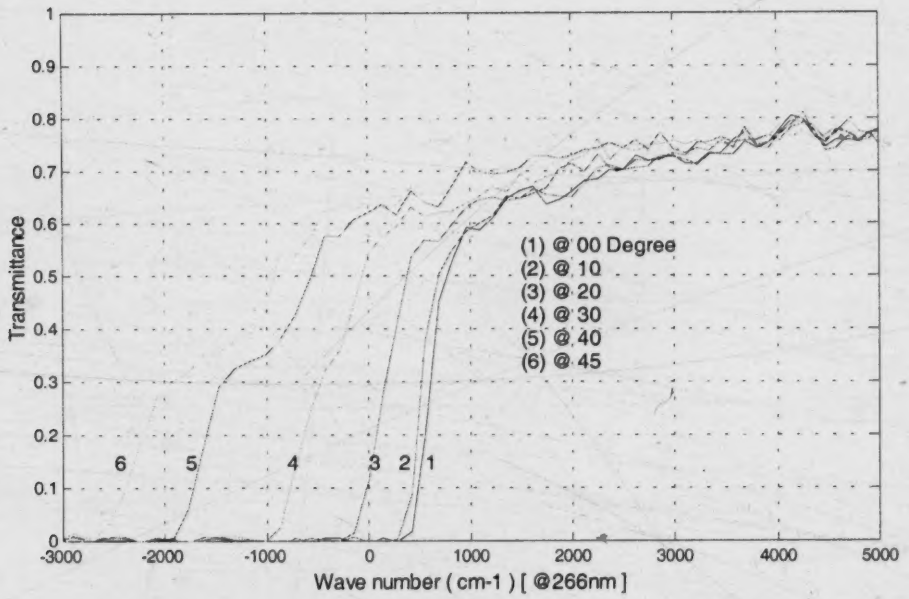

Fig. 3.1.1-3 UVHP Raman filter transmittance vs. wave number

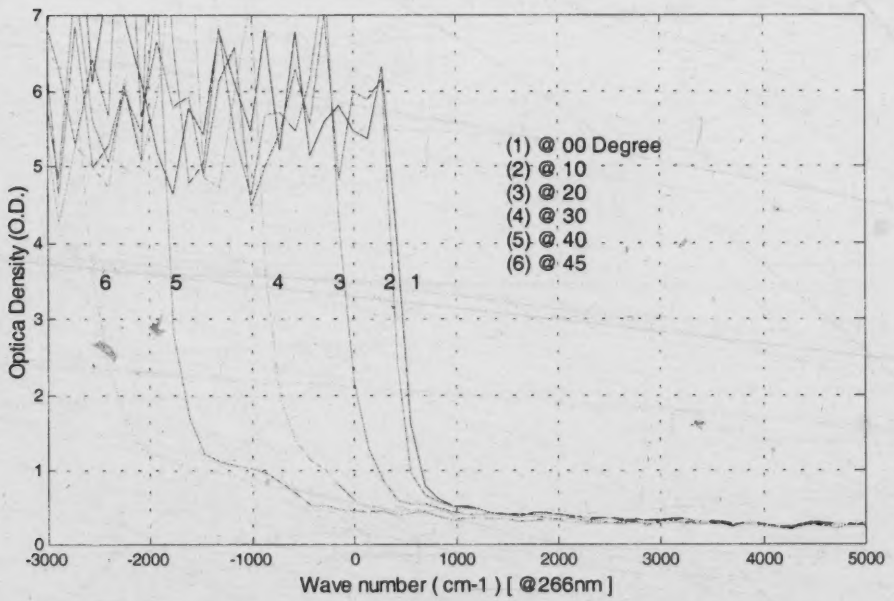

Fig. 3.1.1-4 UVHP Raman filter Optical density vs. wave number

3.1.2 The calibration of a dielectric mirror

A dielectric mirror was initially used as a cutoff filter for the Raman measurements. The mirror was an existing mirror designed to give a high reflectance at 268 nm for a 45° angle of incidence. This mirror was measured with the Perkin Elmer Lambda 900 Spectrophotometer at the NanoFab at various angles of incidence.

The transmittance vs. wavelength at the different angles of incidence is plotted in the Figure 3.1.2-1, and Figure 3.1.2-2 gives the Optical Density vs. wavelength. Because a wavelength of 266nm is used as an exciting wavelength for Raman spectroscopy, the transmittance vs. wave number and the Optical Density vs. wave number for 266 nm Raman exciting wavelength are give in Figures 3.1.2-3 and 3.1.2-4, respectively.

It can be seen that the blocking wavelength shifts to shorter wavelengths as the normal incident angle increases. With a normal incident angle around 37°, the mirror has an Optical Density around 2 for Rayleigh scattering, while the transmittance for Raman spectra is about 30% at 500cm^{-1}.

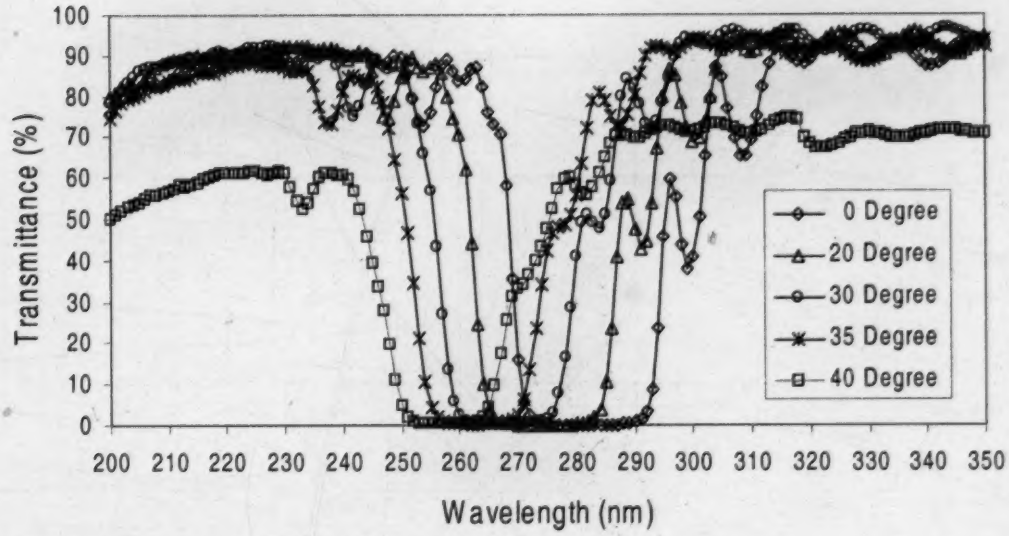

Fig. 3.1.2 – 1 The transmittance vs. wavelength for the UV dielectric mirror

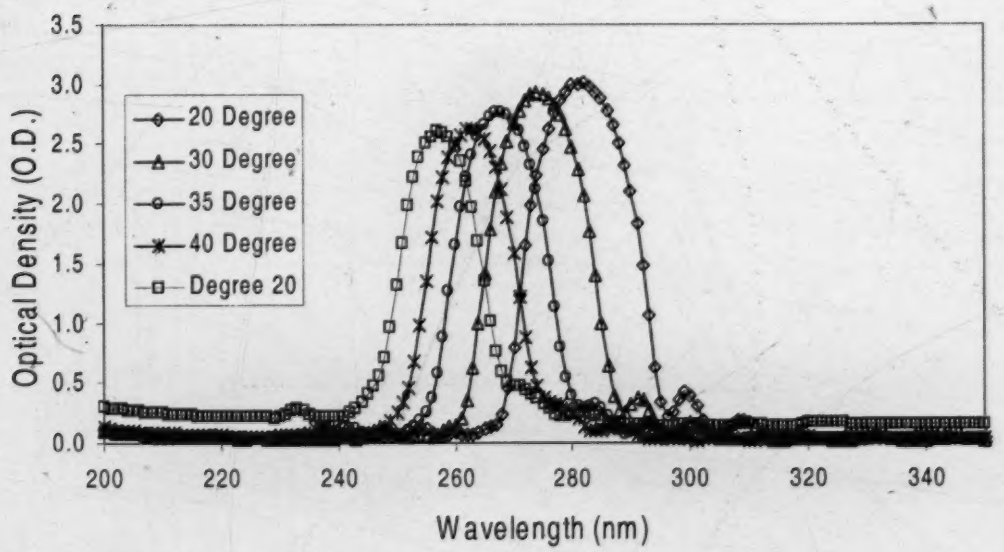

Fig. 3.1.2 – 2 The Optical Density vs. wavelength for the UV dielectric mirror

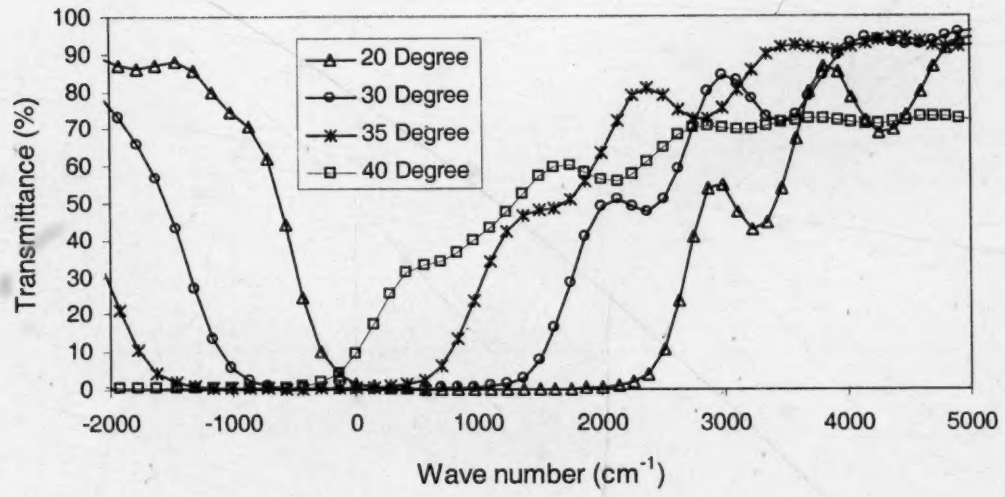

Fig. 3.1.2 - 3 The filter transmittance vs. wave number for the UV dielectric mirror

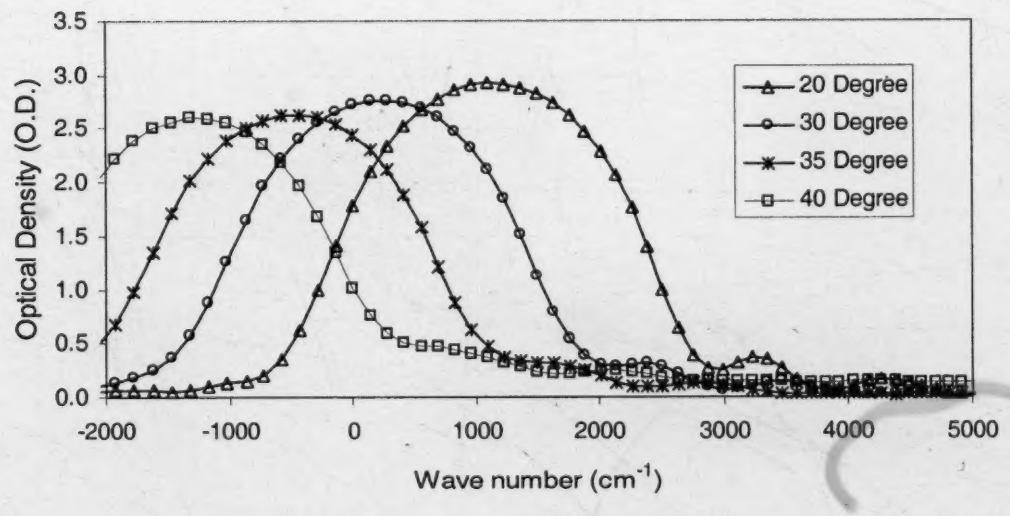

Fig. 3.1.2 – 4 The Optical density vs. wave number for the UV dielectric mirror

3.1.3 Liquid Filter, Fluorobenzene in Cyclohexane solvent

A suitable candidate for a liquid Raman filter, fluorobenzene with light petroleum as solvent, was found from "UV Atlas of Organic Compounds" D7/3 [20]. As it has a very strong absorption at 266 nm and very sharp cut-off, potentially, it can be used as a liquid filter to eliminate Rayleigh scattering at 266nm, the wavelength of the exciting laser. This idea was tested and it was demonstrated that fluorobenzene is a good Raman filter. The advantages are low cost and controllable transmittance by changing its concentration.

The container of the liquid filter is a high quality far UV quartz cell (NSG Precision Cells, Inc)[35]. It is a cylindrical cell with a path length 10mm and diameter 50mm. The transmission of the cell is greater than 80% from 250 nm to 1000 nm.

Because light petroleum is not readily available, cyclohexane was used as the solvent in this case. Other solvents such as, hexanes, octance or methanol are possibly worth trying as they may give even better characteristics for the filter.

A high concentration solution of fluorobenzene with cyclohexane as the solvent is made with a molar concentration given by

$$M_0 = \frac{\left(\frac{M}{M_w}\right)}{V} \qquad (3.1.3\text{-}1)$$

where M_0 is the molarity of the solution, M is the mass of Fluorobenzene, M_w is the molecular weight of Fluorobenzene and V is the volume of solution. Then, this high concentration solution is diluted to the desired concentrations by adding more solvent, the final molar concentration is

$$M_i = \frac{V_0}{V_i} M_0 \qquad (3.1.3\text{-}1)$$

M_0 is the molarity of the high concentration solution, M_i is the molarity of the desired concentration solution, V_0 the volume of high concentration solution and V_i is the volume of the final desired concentration solution.

Four different concentration solution were tested, #1 = 1.10×10^{-1} M, #2 = 1.64×10^{-2} M, #3 = 2.03×10^{-3} M, #4 = 3.66×10^{-4} M. They were measured with the Perkin Elmer Lambda 900 Spectrophotometer at the NanoFab. Figures 3.1.3-1 and 3.1.3-2 show the transmittance and Optical Density versus wavelength. Figures 3.1.3-3 and 3.1.3- 4 give the transmittance and Optical Density versus wave number for 266nm irradiation wavelength.

From these curves, liquid filter #2 with a concentration 1.64×10^{-2} M gives O.D. greater than 4 at 0 cm^{-1} while its transmittance is greater than 40% at 1000cm^{-1}.

This liquid filter was successfully used in the experiments shown in Figure 2.1-3.

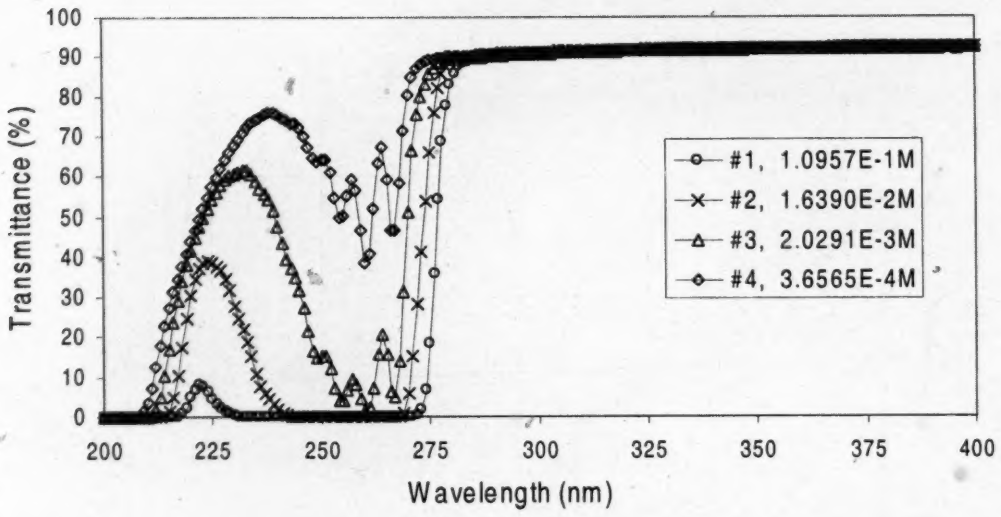

Fig. 3.1.3 - 1 The transmittance vs. wavelength for the Liquid Filter

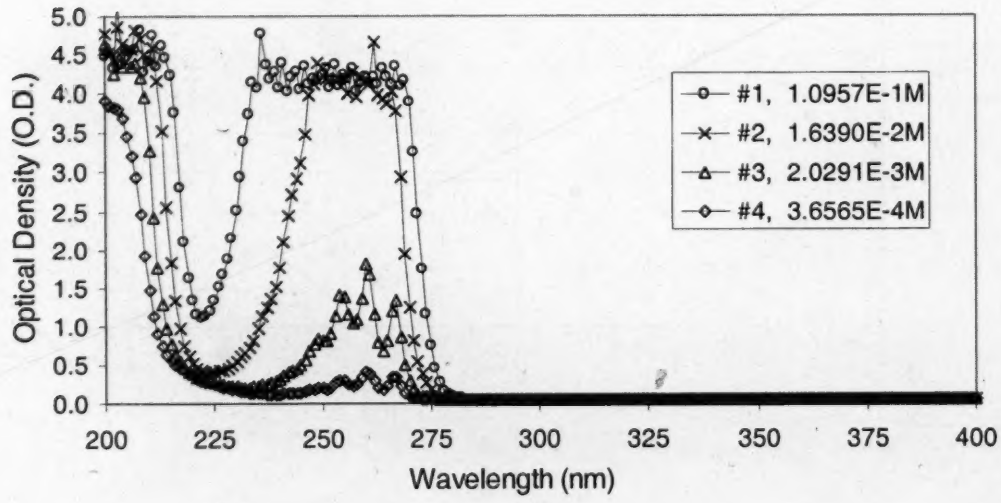

Fig. 3.1.3 – 2 The Optical Density vs. wavelength for the Liquid Filter

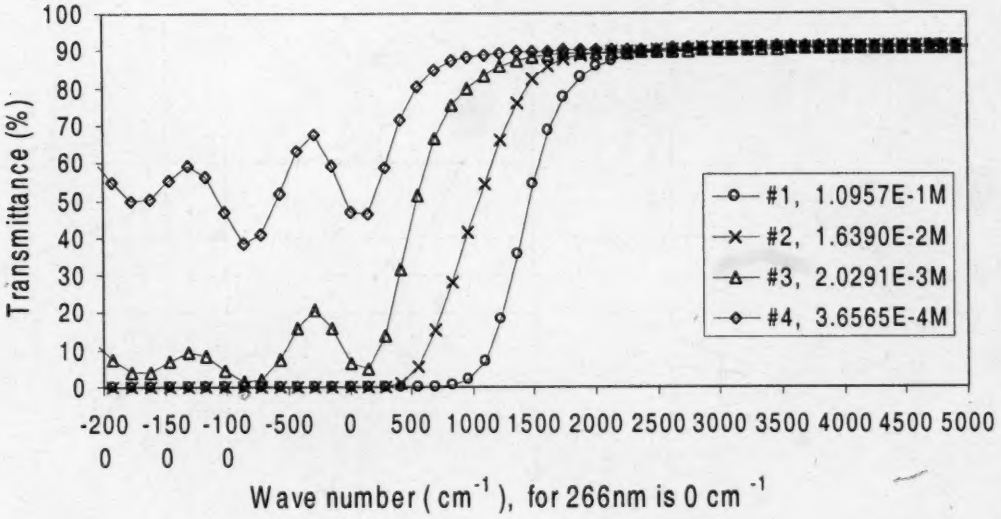

Fig. 3.1.3 - 3 The filter transmittance vs. wave number for the Liquid Filter

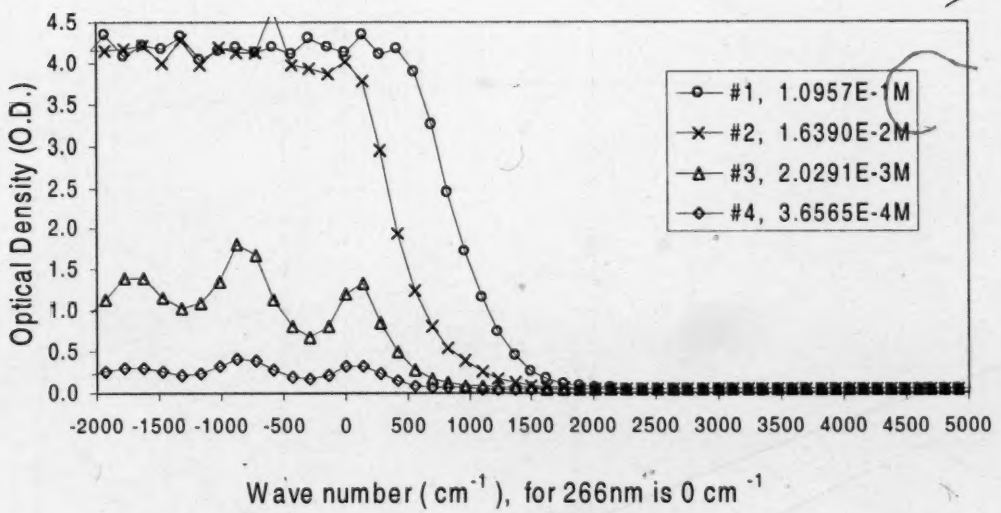

Fig. 3.1.3 – 4 The Optical density vs. wave number for the Liquid Filter

3. 1. 4 Calibration of the UV beam Splitter

The beam splitter is a crucial optical element in the interferometer. It should work properly in the UV region from 248 nm to 310 nm as 4th harmonic Nd:YAG lasers with 266 nm wavelength or KrF lasers with 248 nm wavelength could be used as the exciting lasers for the present FT UV Raman spectroscopy. It should also give the same value of transmittance and reflection for both s and p polarization in order to obtain a high visibility fringe pattern.

Such a beam splitter was ordered from Melles Griot. It is a 1 inch UV-grade synthetic fused silica Broadband Hybrid Cube Beamsplitter with catalog number 03 BSC 057. The company claims that the transmission is 38% ± 6% from 250 nm to 280 nm, 43% ± 6% from 280 nm to 400 nm, s-plane and p-plane components matched to within 5% from 250 nm to 400 nm, the absorption is less than 24%, and entrance and exit surfaces are coated for less than 1% reflectance. No specification sheet comes along with this beam splitter but two theoretical curves were supplied by Melles Griot which are reprinted in Figures 3.1.4-1 and 3.1.4-2 that represent transmission and reflectance versus wavelength respectively. Melles Griot optimizes and specifies the transmitted intensity while calculating the intensity of the reflected light by

$$I_{reflection} = I_{source} - I_{transmit} - I_{absorb} - I_{surface,reflect} \qquad (3.1.4\text{-}1)$$

Since the absorption varies with wavelength and can vary from sample to sample, both transmission/reflectance versus wavelength and the reflection of surfaces have to be checked out in the wavelength region of interest. Also, to operate optimally both s- and p-polarization should give the same effects either in the transmittance or in the reflection.

An experimental setup was designed to verify the transmittance and reflection vs. wavelength for both s and p polarization which is shown in Figure 3.1.4-3. It consisted of the 4th harmonic Nd:YAG laser at 266nm, with p-polarization and a maximum 6 mJ output, a wedge, a neutral density filter with O.D. 0.6, a photodiode (EG&G FN 100) and an oscilloscope. The measurement for s polarization was taken by rotating the beam splitter by 90°. The measurements are summarized in Figure 3.1.4-4. The results of the measurements are shown in Figures 3.1.4-1 and Figure 3.1.4-2 to compare with the theoretical curves of Melles Griot.

The reflection of the surfaces was measured by the same setup but with a different arrangement as shown in Figure 3.1.4-5. Keeping the photodiode in the same position while rotating the beam splitter, the four surfaces were measured accordingly. The measurements are summarized in Figure 3.1.4-6.

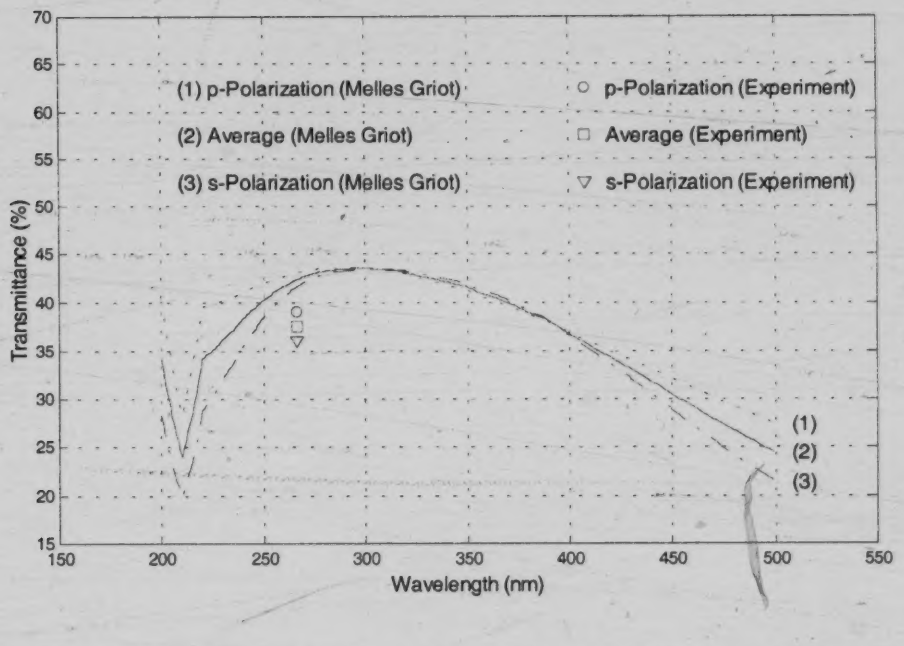

Fig. 3.1.4 – 1 The transmittance vs. wavelength of UV Beam Splitter

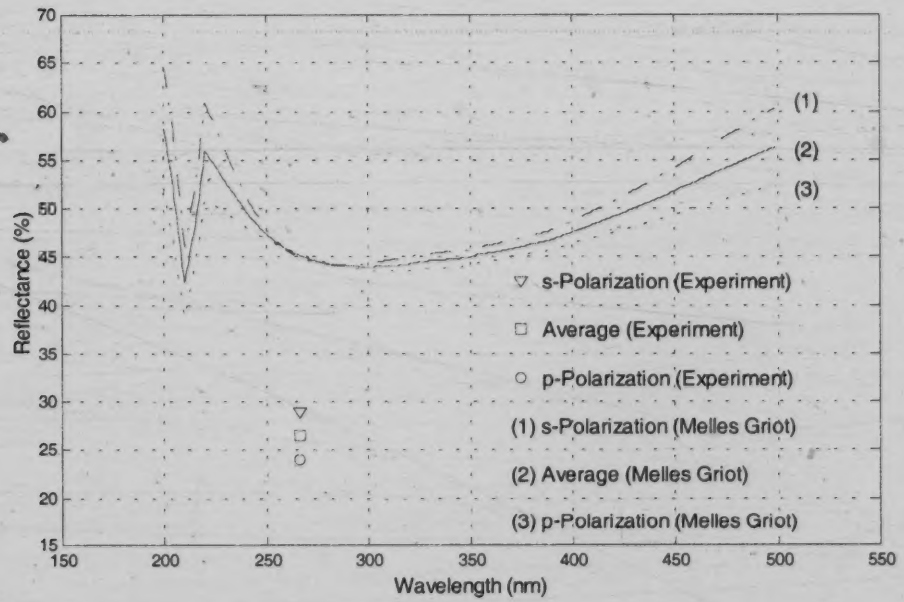

Fig. 3.1.4 - 2 The reflectance vs. wavelength of UV Beam Splitter

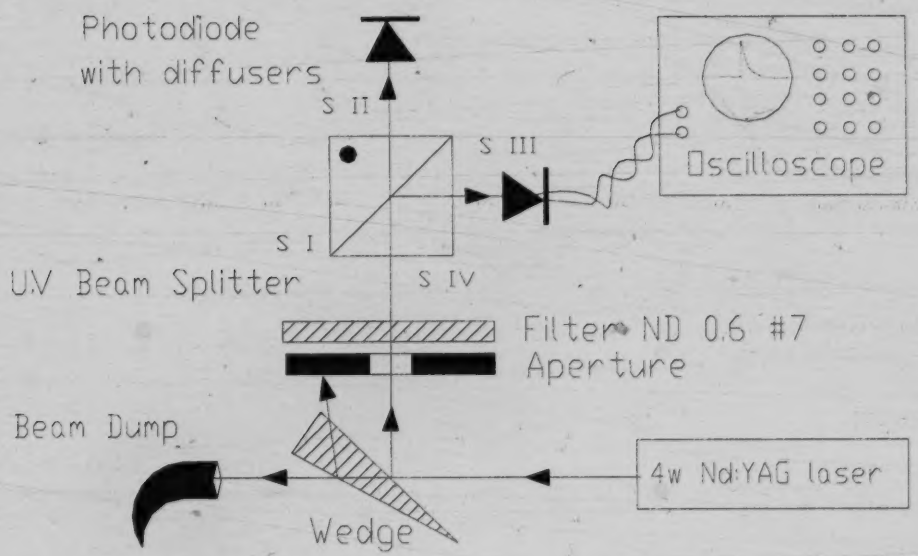

Fig. 3.1.4-3 The setup for the UV Beam Splitter transmittance and reflectance tests

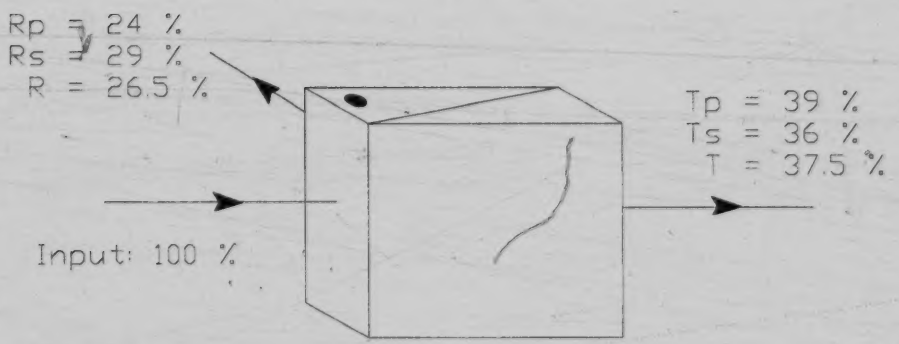

Fig. 3.1.4 – 4 The transmittance and reflectance of the UV the Beam Splitter

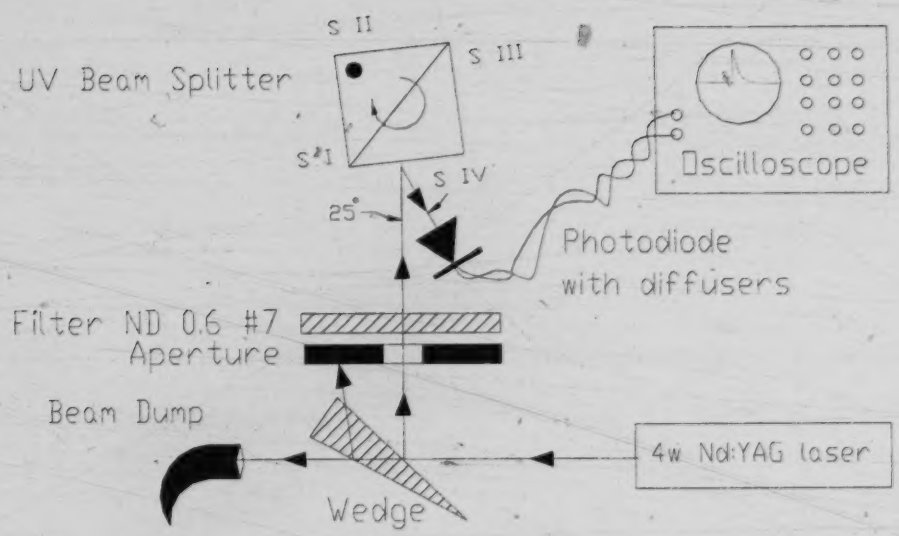

Fig. 3.1.4-5 The setup for testing of the UV Beam Splitter surface reflection

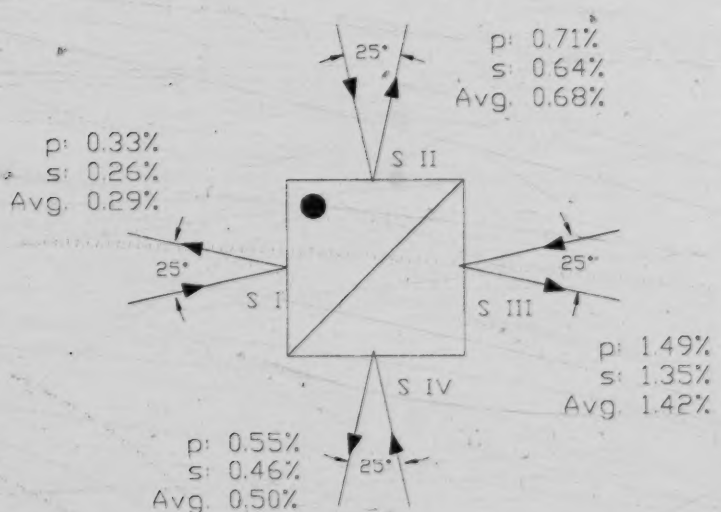

Fig. 3.1.4 – 6 The surface reflections of the UV Beam Splitter

3. 1. 5 The calibration of UV CCD

The UV CCD camera used in this experiment is a product of Andor(DU440-BU2, 2492)[36]. The camera is a 512 pixel high by 2048 pixel wide cooled CCD Camera with a very low noise preamplifier to give the capability of detecting very weak signals. Calibrations were carried out to determine its read out noise, the dark current and the responsivity. These results were compared to the manufacture's specification for this camera. Before we go to next step, we will give a brief description of the geometrical size of the UV CCD camera (Andor model DU440-BU2, 2492). The UV CCD camera has an array of 2048 × 512 active pixel, 13.5 × 13.5 μm^2 pixel size and total image area 27.648mm × 6.912mm. The diagonal length D is thus

$$D = \sqrt{W^2 + H^2} = \sqrt{27.648^2 + 6.912^2} = 28.5 \ mm$$

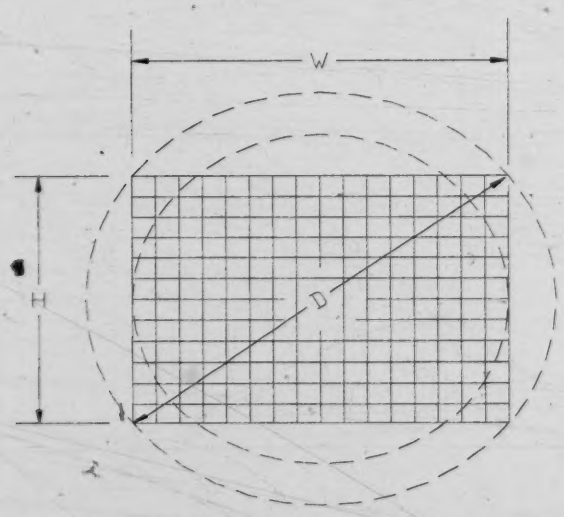

Fig. 3.1.5-1 The geometric layout of UV CCD

The Read Out noise of the UV CCD camera

The readout noise is checked by blocking the UV CCD camera in a dark room and operating at -50°C. The data acquisition is conducted under both 2-D image & Full Vertical Binning (FVB) modes with read out times per pixel of 1 μs, 2 μs, 16μs and 32 μs. For each case, 10 files are used to calculate Root Mean Square (R.M.S.) noise level. The readout noise is calculated by taking the R.M.S. of every individual pixel and averaging the R.M.S. values from the whole 2048 × 512 pixels field of view. The maximum, minimum and the average R.M.S. level of 2048 × 512 pixels and the specification given by Andor for the camera at various readout rates are given in Table 3.1.5-1. The base level is the average value of 2048 × 512 pixels from 10 files. It can be seen from Table 3.1.5-1 that both Readout Noise and Base Level are close to the values listed on the specification sheet of Andor.

FVB, R.M.S (n = 10), T = - 50						Base Level		
	Min	Max	Avg	Andor	%(Andor~Avg.)	Measured	Andor	%
1us	**2.35**	**12.40**	**6.73**	**8.27**	-18.56%	265	239	10.80%
2us	**2.50**	**12.02**	**6.83**	**7.15**	-4.49%	120	159	-24.42%
16us	**1.18**	**5.77**	**2.98**	**3.14**	-5.00%	243	340	-28.43%
32us	**1.14**	**5.49**	**2.93**	**3.20**	-8.36%	338	508	-33.54%
Imaging, R.M.S (n = 10), T = - 50						Base Level		
	Min	Max	Avg	Andor	%(Andor~Avg.)	Measured	Andor	%
1us	**0.94**	**15.15**	**6.46**	**7.98**	-19.09%	244	239	1.97%
2us	**0.63**	**14.74**	**6.42**	**6.68**	-3.85%	105	159	-34.09%
16us	**0.00**	**5.56**	**2.36**	**2.39**	-1.23%	226	340	-33.45%
32us	**0.30**	**5.20**	**2.09**	**2.31**	-9.60%	308	508	-39.35%

Table 3.1.5-1 The readout noise and the background level of the UV CCD camera at various readout rates

The Dark Current of the UV CCD camera

The Dark Current of the UV CCD camera is tested in a dark room with a black cover on the UV CCD camera to eliminate any stray light. The UV CCD camera is set up in a Full Vertical Binning Mode at each of the following temperature –20°C, -30°C, -40°C, or -50°C. For each read out time (1μs, 2μs, 16μs, and 32 μs), data was acquired for exposure times of 1,2,5,10, 30, 60, 120, and 240s, respectively. The read values are converted to electrons from counts by the corresponding responsivities listed on the manufacturer's specifications(2, 2, 1.4, 0.7 electrons per A/D for 1μs, 2μs, 16μs, 32 μs, respectively) and put into Table 3.1.5-2. Then, the dark current, electrons/pixel/second, is calculated by taking a linear fit to the data.

Full vertical binning, Temperature = -20									
Readout Time per pixel (10E-6 s)	Exposure time (S)								electrons/ pixel/sec
	1	2	5	10	30	60	120	240	
1	354	463	778	1307	3420	6718	13281	26320	0.4247
2	224	345	674	862	3227	6604	13069	26160	0.4251
16	421	570	1001	1693	4668	9056	17679	35316	0.3989
32	680	975	1800	3291	8851	17262	34272	51257	0.3008
Full vertical binning, Temperature = -30									
Readout Time per pixel (10E-6 s)	Exposure time (S)								electrons/ pixel/sec
	1	2	5	10	30	60	120	240	
1	293	320	409	533	1205	2083	3864	7627	0.1196
2	165	196	293	448	1086	2035	3879	7543	0.1207
16	313	357	487	712	1557	2764	5237	10121	0.1121
32	475	546	819	1210	2865	5426	10310	19852	0.1111
Full vertical binning, Temperature = -40									
Readout Time per pixel (10E-6 s)	Exposure time (S)								electrons/ pixel/sec
	1	2	5	10	30	60	120	240	
1	264	267	295	335	510	812	1332	2424	0.0354
2	138	149	179	216	402	691	1255	2315	0.0357
16	267	276	310	371	610	976	1737	3124	0.0329
32	380	403	476	572	1053	1814	3238	6016	0.0324
Full vertical binning, Temperature = -50									
Readout Time per pixel (10E-6 s)	Exposure time (S)								electrons/ pixel/sec
	1	2	5	10	30	60	120	240	
1	259	260	269	277	341	399	567	857	0.0098
2	118	122	127	135	189	261	429	790	0.0109
16	241	243	254	271	336	441	615	976	0.0084
32	335	340	357	392	531	726	1073	1681	0.0078

UV CCD Dark Current Tests, Feb 07 2002					
T	R.T.=1*10^ -6S	R.T.=2*10^ -6S	R.T.=16*10^-6 S	R.T.=32*10^ -6S	Andor
-20	0.4247	0.4251	0.3989	0.3008	0.3500
-30	0.1196	0.1207	0.1121	0.1111	0.1000
-40	0.0354	0.0357	0.0329	0.0324	0.0250
-50	0.0098	0.0109	0.0084	0.0078	0.0085
-60					0.0020
Comparision of measurements with Andor for UV CCD Dark Current Tests, Feb 07 2002					
T	R.T.=1*10^ -6S	R.T.=2*10^ -6S	R.T.=16*10^-6 S	R.T.=32*10^ -6S	
-20	21%	21%	14%	-14%	
-30	20%	21%	12%	11%	
-40	42%	43%	32%	30%	
-50	15%	28%	-1%	-8%	
-60					

Table 3.1.5-2 The Dark Current of the UV CCD camera

The above procedure was repeated for temperatures of –20°C, -30°C, -40°C, and -50°C. Figure 3.1.5-1 gives a plot of the resultant dark current and the Andor's values. The Dark Current of the UV CCD camera at –60°C was not tested because the water cooling was not used and air cooling only allowed operation to -50°C.

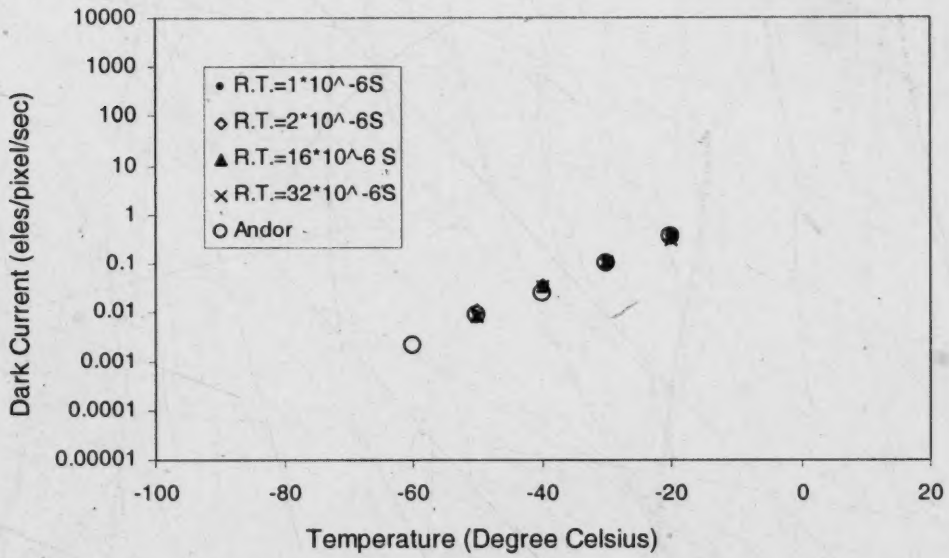

Fig. 3.1.5-2 The Dark Current of UV CCD

The responsivity tests of the UV CCD camera using a Tungsten lamp

The responsitivity of the UV CCD camera was tested using three different calibrated sources: a Tungsten Lamp, a 4ω Nd:YAG laser and a mercury lamp. Figure 3.1.5-2 is a schematic diagram of the tests with the Tungsten lamp. It consists of a Tungsten lamp (General Electric Company, Model No. EPT–1182), an aperture with 3mm diameter, an aperture 7 mm wide by 12 mm high, a spectral filter set, a shutter (Vincent Associates, Model VMM-D1) and the UV CCD camera (Andor DU440-BU2, 2492). The filter set consists of four filters with the lab numbers Filter 700, Filter 5000, Filter 550 and Filter IR#1, accordingly.

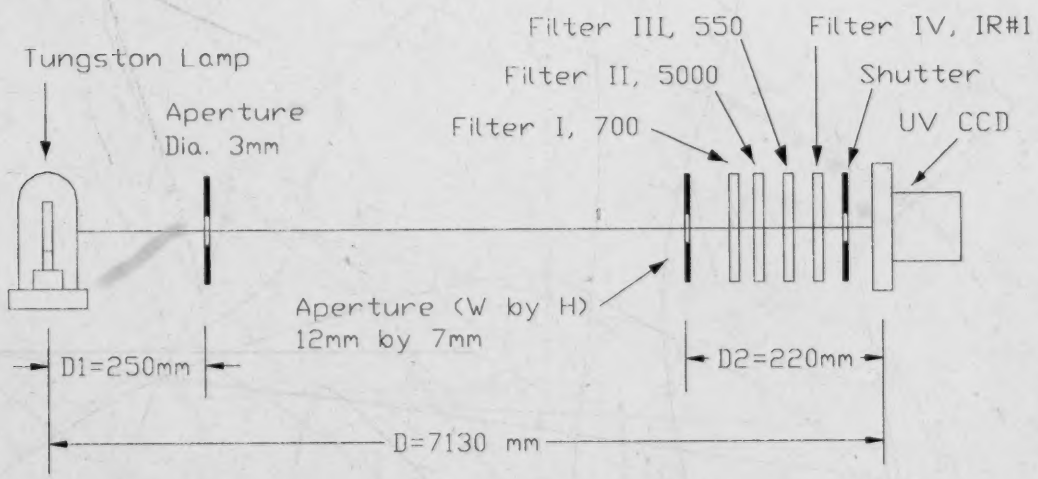

Fig. 3.1.5-3 The setup of the gain testing of UV CCD with a Tungsten lamp

The calibrated radiance vs. wavelength of the Tungsten lamp is shown in Figure 3.1.5-3. Figure 3.1.5-4 shows the Quantum Efficiency of the UV CCD camera vs. wavelength that was given by Andor. The transmittance vs. wavelength of the filter set is

calculated by multiplying each of their individual transmittance vs. wavelength characteristics together and the result is shown in Figure 3.1.5-5.

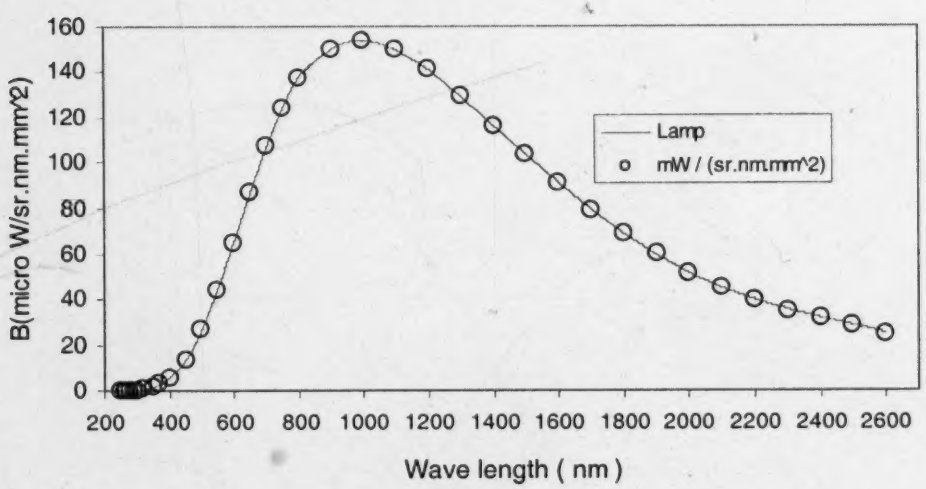

Fig. 3.1.5-4 The spectral radiance of Tungsten lamp (EPT-1182) at 35Amperes

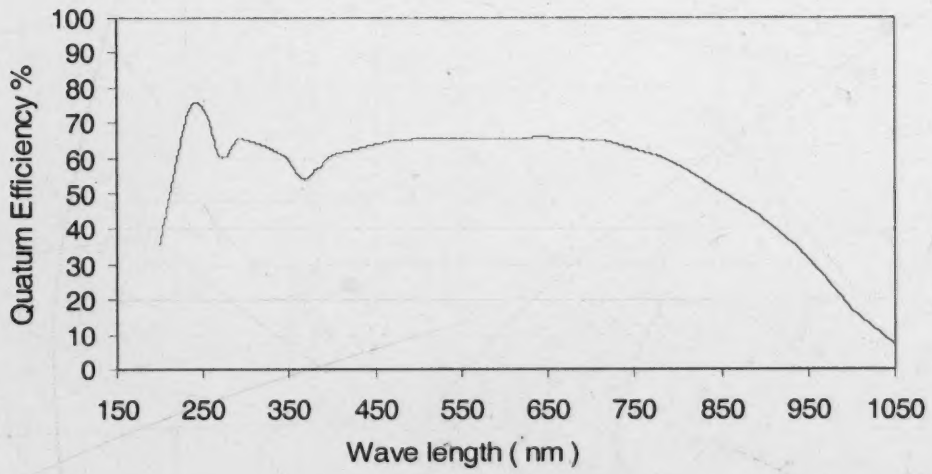

Fig. 3.1.5-4 The Quantum efficiency of the UV CCD camera

as given by the manufacturer, Andor

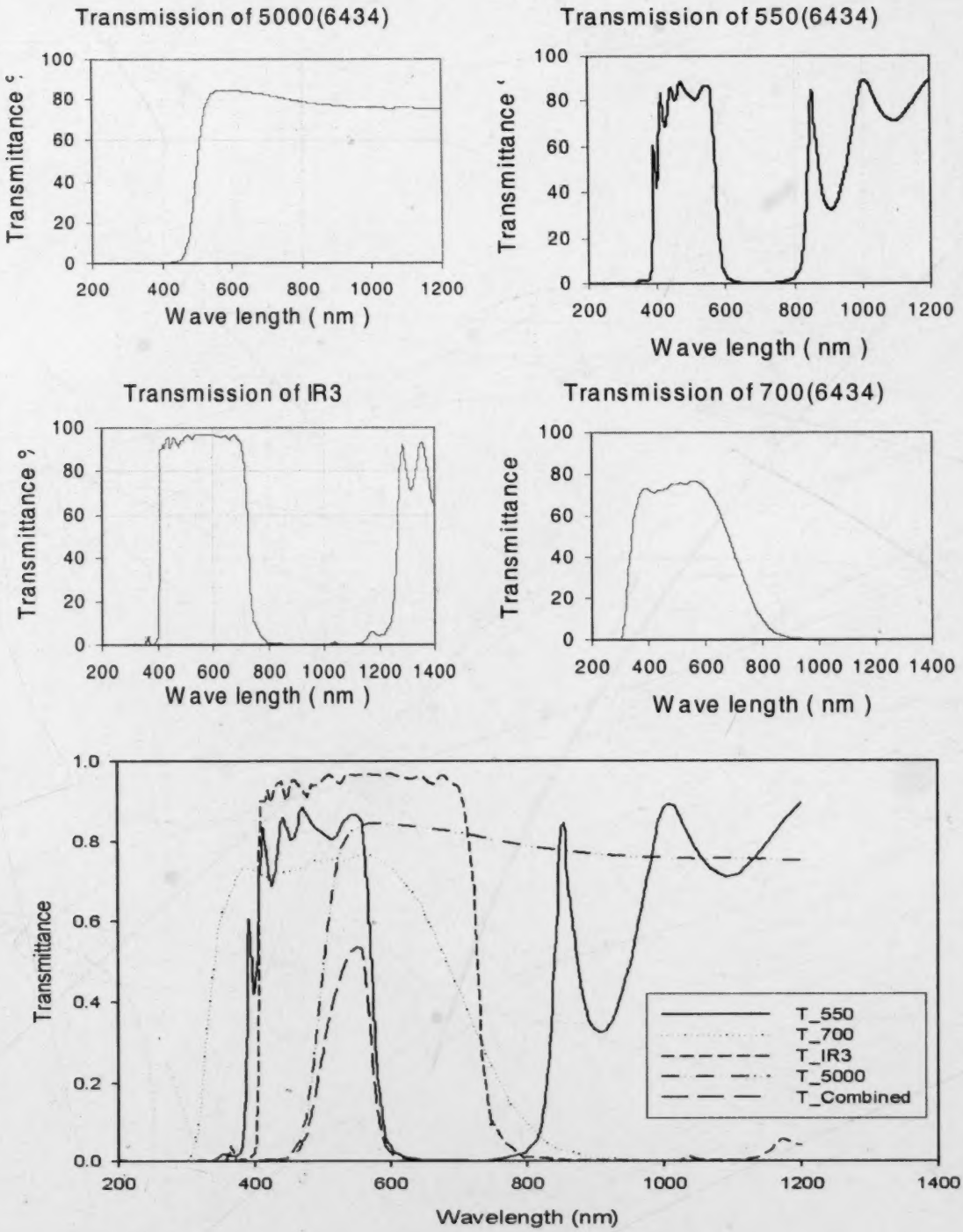

Fig. 3.1.5-5 The transmittance vs. wavelength of each of the filters and the calculated combined filters transmission

As shown in Figure 3.1.5-3, the solid angle of a single pixel to the Tungsten lamp is determined by the area of one pixel and the distance D from UV CCD to the Tungsten lamp as following.

$$\Omega_T = \frac{Area\ of\ one\ pixel}{D^2} \tag{3.1.5-1}$$

The effective area of the Tungsten lamp shining on the UV CCD camera is limited by the size of aperture with diameter d_A, the distance of aperture to Tungsten lamp D_1, the distance of the UV CCD camera to Tungsten lamp D and is given by:

$$A = \frac{D^2}{(D - D_1)^2} \times \frac{\pi}{4} d_A^2 \tag{3.1.5-2}$$

For a given wavelength, the spectral photon density, $n(\lambda)$, is related to the spectral energy density, $E(\lambda)$, as

$$E(\lambda) = n(\lambda)\frac{hc}{\lambda} \tag{3.1.5-3}$$

$$dE(\lambda) = dn(\lambda)\frac{hc}{\lambda} \tag{3.1.5-4}$$

and then the energy is a function of the spectral radiance of the Tungsten lamp $B(\lambda)$, the solid angle Ω, the effective area of Tungsten lamp A, the exposure time T, the transmittance of the filter set $Tr(\lambda)$ and the quantum efficiency of UV CCD $Q(\lambda)$.

$$dE(\lambda) = B(\lambda) \times \Omega \times A \times T \times Tr(\lambda) \times Q(\lambda) \times d\lambda \tag{3.1.5-5}$$

Combining the above equations, the number of photons received by the UV CCD camera is then given by

$$n = \int n(\lambda)d\lambda = \int \frac{\lambda}{hc} \times B(\lambda) \times \Omega \times A \times T \times Tr(\lambda) \times Q(\lambda) \times d\lambda \qquad (3.1.5\text{-}6)$$

The responsivity of the UV CCD camera was tested with the Tungsten lamp on Nov. 18, 2001 and Jan 21, 2002, respectively. Table 3.1.5-4 is the summary of these results and the comparison with Andor. It can be seen that our measured responsivity is approximately 35% lower than that given in the Andor specifications.

	#1	#2	#3	Experiment Average	Andor	Date of measurement
Photons	48947	48947	48947			
Counts from CCD	16817	16912	16510			
Photoelectrons /Counts	2.91	2.89	2.96	2.92 ±0.3	2.00	Nov. 28, 2001
Photons	38181	80460	78721			
Couns from CCD	14685	29800	29156			
Photoelectrons /Counts	2.60	2.70	2.70	2.67 ±0.3	2.00	Jan. 21, 2002

Table 3.1.5-3 Calibration of responsivity using a Tungsten lamp

Responsivity of the UV CCD camera with a 4ω Nd:YAG laser

For calibration using UV laser pulse, the output pulse are directed at a diffuse $BaSO_4$ scattering plate. As shown in Figure 3.1.5-6, when the laser pulse hits the $BaSO_4$ plate, scattered light is generated and then detected by the UV CCD camera. A calibrated neutral density filter is used to prevent the UV CCD camera from saturating. The 4ω Nd:YAG laser was set to an output energy of 3.8 mJ. The UV CCD camera was set to a temperature of -20°C, the exposure time 1s, the delay time 2.315s and in the imaging readout mode. The UV CCD camera is placed at a distance 2.56m away from the $BaSO_4$ scattering plate with an observation angle 49° relative normal.

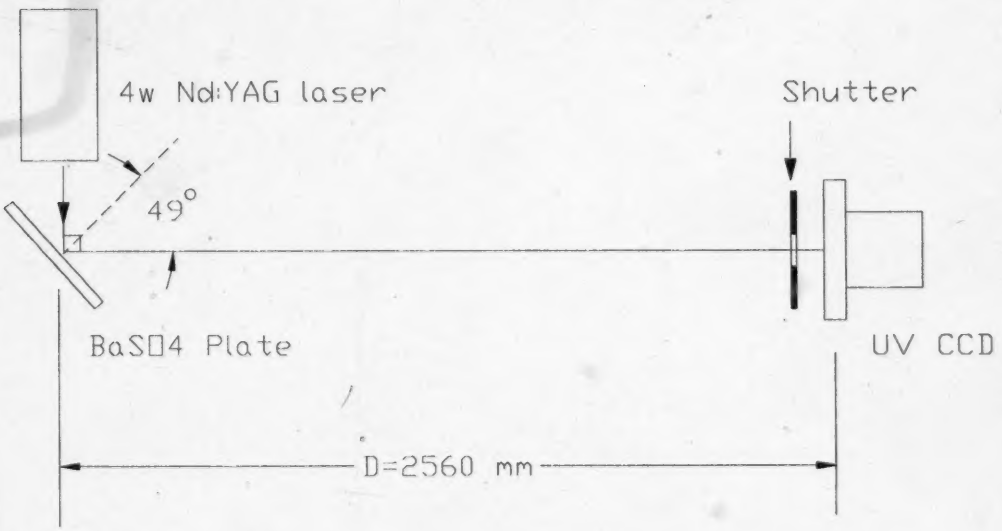

Fig. 3.1.5-6 The setup for the responsivity calibration of the UV CCD camera with 266nm laser pulse

According to the Lambertian scattering law [24], the energy scattered per steradian by the $BaSO_4$ plate is

$$I_{BaSO4} = \eta \times E_0 \times \frac{1}{\pi} \times \cos\phi \qquad (3.1.5\text{-}7)$$

where η is the integrated scattering efficiency of the $BaSO_4$ plate assumed to be 95%, E_0 is the laser pulse energy, 3.8mJ and ϕ is the angle between the normal of $BaSO_4$ plate and the observation direction. The energy on a single pixel of the UV CCD camera is then determined by

$$E_{one\ pixel} = I_{BaSO4} \times \Omega \qquad (3.1.5\text{-}8)$$

where $\Omega = \frac{A_{pix}}{D^2}$ is the solid angle of one pixel to the scattering light source on $BaSO_4$ plate, A_{pix} is the area of one pixel, D is the distance from UV CCD to $BaSO_4$.

The number of photoelectrons detected per pixel is:

$$n_{Re} = \eta \times E_0 \times Q \times \frac{1}{\pi} \times \cos\phi \times \Omega \times \frac{\lambda}{hc} \qquad (3.1.5\text{-}9)$$

$$= 95\% \times 3.8mJ \times 65\% \times \frac{1}{\pi} \times \cos 49^0 \times \left(\frac{13.5\mu m}{2.56m}\right)^2 \times \frac{266nm}{6.626\times10^{-34} J.S \times 3\times10^8 m/S}$$

$$= 9{,}115$$

where Q is the quantum efficiency of UV CCD given by the manufacturer, Andor. The average reading measured on the CCD camera is 2100±50 counts, the gain can then be calculated.

$$Gain = \frac{n_{Re}}{counts} = \frac{9{,}115}{2{,}100} = 4.34 \pm 0.6 \ (photoelectrons/count) \qquad (3.1.5\text{-}10)$$

while Andor claims the gain of the UV CCD camera is 2 photoelectrons per count.

Calibration of the UV CCD camera with a Hg lamp

After checking the calibration by using 266nm laser pulses and Tungsten lamp, the gain of UV CCD was also calibrated with a Hg lamp. The experimental arrangement consists of a Hg lamp(Oriel 6035), a Hg lamp 254.7 nm filter and the UV CCD camera. From the Oriel specification sheet, the Hg Lamp gives an irradiance of B = $7.4\times10^{-5} W/cm^2$ at a distance 25cm away at a wavelength of 254.7 nm. The UV CCD camera is located 7.12m from the Hg lamp with the Hg lamp filter in front of it. The energy on a single pixel of the UV CCD camera can be expressed as

$$E = \left(\frac{D_0}{D}\right)^2 \times B \times T \times A_{Pix} \times \tau \qquad (3.1.5\text{-}11)$$

where D_0 equals 25 cm as indicated by Oriel,

D equals 7.12m, a distance from Hg lamp to UV CCD,

T is the transmittance of Hg filter with Lab Number (SS25) at 254.7 nm, 16.5%,

A_{Pix} is the area of single CCD pixel (13.5μm by 13.5μm),

τ is the shutter time,1s,

and Q is the quantum efficiency of UV CCD at 254.7 nm, 73% as given by Andor.

The numbers of photoelectrons generated in a single pixel can then be calculated

$$n_{Re} = \left(\frac{\lambda}{hc}\right) \times \left(\frac{D_0}{D}\right)^2 \times B \times T \times A \times \tau \times Q \qquad (3.1.5\text{-}12)$$

$$= \left(\frac{254.7nm}{6.626\times10^{-34} J.S \times 3\times10^{8} m/S} \right) \times \left(\frac{25cm}{7.12m} \right)^2 \times 7.4\times10^{-5} W/cm^2 \times 16.5\%$$

$$\times (13.5\mu m \times 13.5\mu m) \times 1S \times 73\%$$

=25,600 photoelectrons

The experimentally measured counts read from the CCD camera after background subtraction are 6000 counts, the responsivity of the UV CCD camera is then

$$R = \frac{n}{counts} = \frac{25,600}{6000} = 4.26 \pm 0.6 \ (photoelect rons/count) \qquad (3.1.5\text{-}13)$$

while Andor claims the gain of UV CCD is 2 photoelectrons per count.

Both the 266nm pulsed laser irradiation and the Hg lamp calibration indicate that the responsivity is at least two times worse than specified. In the visible region it appears to be only 35% worse than specified. These results could indicate that quantum efficiency of the camera is not as high as the specifications claim, particularly in the UV range of the spectrum.

Section 3.2 Theoretical Model

3.2.1 The fringe pattern of Sagnac interferometer

The Sagnac interferometer can be considered as an optical device based on the interference produced from two point light sources. The coherence is obtained from the two interfering monochromatic waves coming from the same point of the light source split into two virtual point sources, as shown in Figure 3.2.1-1. Let the circles spreading out of each point represent crests, then there will be a maximum where they intersect. Considering a point P on the maximum line, the optical path difference is $S_2P-S_1P = n\lambda$. Because the two light sources are in phase, the peak amplitude at P remains constant over time. In between these peak amplitude planes are nodal planes where the amplitude is zero for two coherent point sources. The fringes can be imaged in three dimensions by rotating two dimensional fringe pattern around the line S_1S_2.

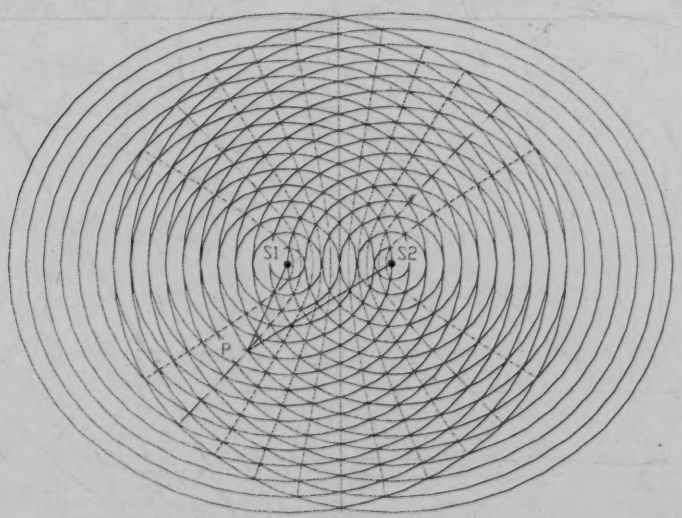

Fig. 3.2.1-1 The theoretical interference patterns of two coherent point light sources in a plane through the two sources

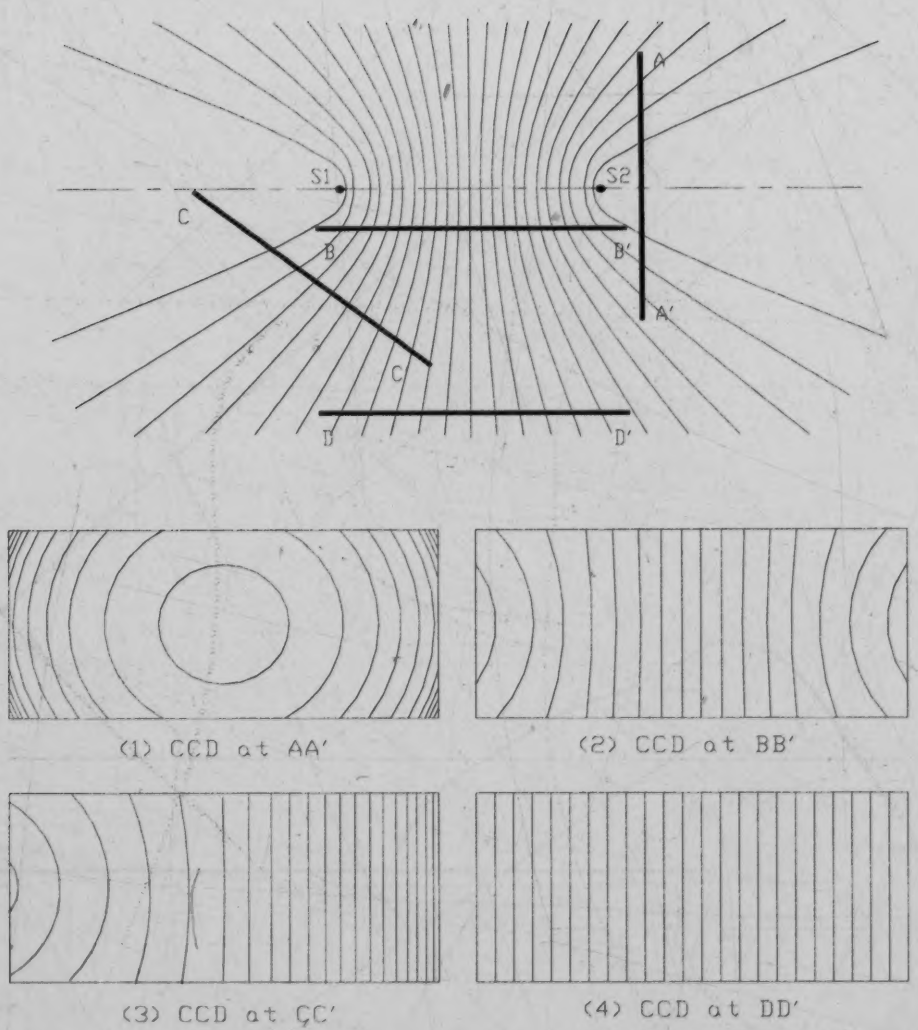

Fig. 3.2.1-2 The fringe pattern on an imaginary CCD

We now examine the fringes of two coherent point sources in Figure 3.2.1-2 and put an imaginary CCD camera at different positions to see the fringe pattern on it. The imaginary CCD camera at line AA' is the case of Michelson interferometer representing by its famous circular rings. When one of the two mirrors is moved in a Michelson interferometer, S_1 moves either toward or away from S_2. A point detector at the center of

the imaginary CCD camera will record a fringe pattern in time. As the imaginary CCD camera moves from position BB' to DD', the fringe pattern changes from the straight lines in the center, with hyperbolic fringe patterns on both sides to the straight lines in the middle with the fringe separation approaching a constant value across the whole screen. The fringe pattern of the imaginary CCD camera at the position DD' is what should be observed when using the Sagnac interferometer, while the situation of the imaginary CCD camera at position BB' should be avoided. It is very important to find out the parameters to optimize the fringe pattern and details on the optimization will be given later. Putting the imaginary CCD camera at the position CC' gives an intermediate fringe pattern between the cases AA'and DD'.

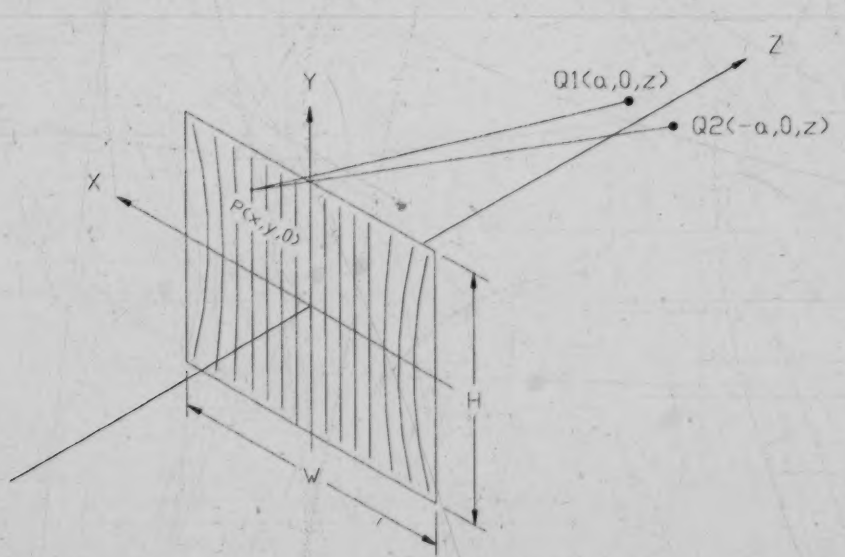

Fig. 3.2.1-3 The interference fringe pattern of two coherent point light sources

The cases related to the Sagnac interferometer should be studied in detail. In Figure 3.2.1-3, two ideal coherent points light sources, located at (a, 0, z) and (-a, 0, z), produce the interference fringe pattern on the x-y plane where a CCD camera, width W

and height H, is located. The optical path difference, $\delta(x, y)$, between these two coherent points at a point P (x, y, 0) on the x-y plane is

$$\delta(x,y) = \sqrt{(x+a)^2 + y^2 + z^2} - \sqrt{(x-a)^2 + y^2 + z^2} \qquad (3.2.1\text{-}1)$$

Solving the above equation, hyperbolic contours are found by

$$x^2 - \frac{y^2}{(\frac{2a}{\delta})^2 - 1} = \frac{z^2 + a^2 - (\frac{\delta}{2})^2}{(\frac{2a}{\delta})^2 - 1} \qquad (3.2.1\text{-}2)$$

The two coherent point light sources generate constructive interference pattern when $\delta(x, y) = m_i\lambda$ where the integral number $m_i = \pm$ 0, 1, 2, ... If $\delta(x, y) << 2a$ and y << z, then equation (3.2.1-2) can then be simplified to

$$x_i = \frac{z\delta(x,y)}{2a} \qquad (3.2.1\text{-}3)$$

or equivalently,

$$\boxed{x_i = \frac{m_i\lambda\, z}{2a}} \qquad (3.2.1\text{-}4)$$

According to equation (3.2.1-3), the condition $\delta(x, y) << 2a$ can be changed to a condition of $\boxed{W << 2z}$. So, under the condition of $W << 2z$, the fringes are straight lines and their separation depends on the input monochromatic wavelength λ. In the present case, z is actually the focus length of FT lens as will be shown later on.

3.2.2 Fringe formation in a Sagnac interferometer

A simple Sagnac interferometer is shown in Figure 3.2.2-1, which consists of a Fourier Transform lens, a static mirror, a movable mirror and a beam splitter. The movable mirror is offset from its symmetric position by a distance d which generates two virtual light sources separated by $\sqrt{2}d$ [5,8]. The function of the Fourier Transform lens is to produce an interference fringe pattern on the CCD detector from these two virtual point sources, that can be transformed to a spectrum in the frequency domain by applying a Fourier Transform.

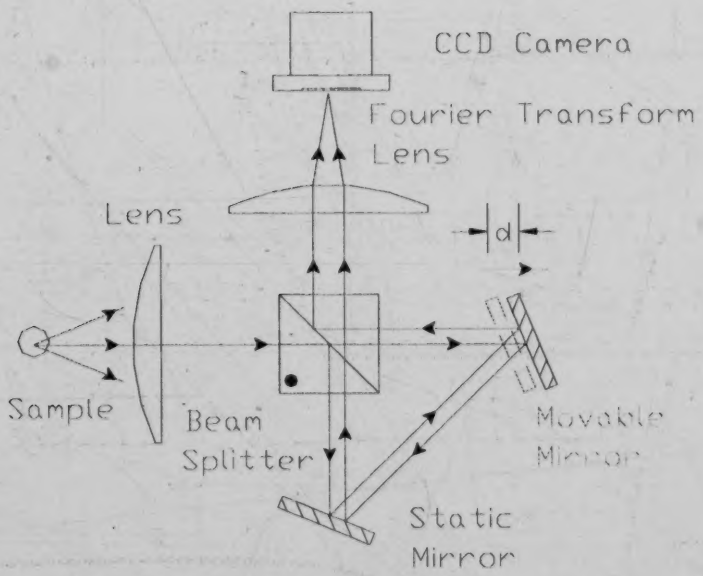

Fig. 3.2.2-1 The schematic diagram of a Sagnac interferometer

In order to understand the function of this Sagnac interferometer, a model has to be established based on the geometric optics. T. Okamoto [21] used a model reprinted in Figure 3.2.2-2. In his description virtual sources are considered located in the front focal

plane of the lens and the photodiode detector array is located in the back focal plane of the lens.

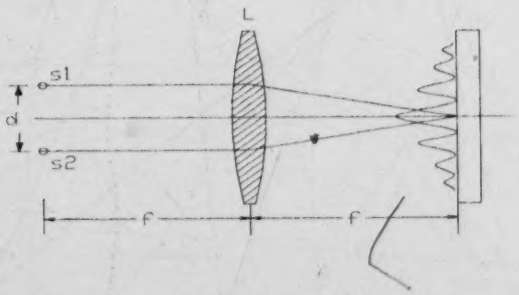

Fig. 3.2.2-2 The model of a Sagnac interferometer by T. Okamoto [21]

In order to understand in detail the optical beam paths, a schematic 3-D model of Sagnac interferometer is shown in Figure 3.2.2-3. A 2-D projection from above to be used for calculations is shown in Figure 3.2.2-4.

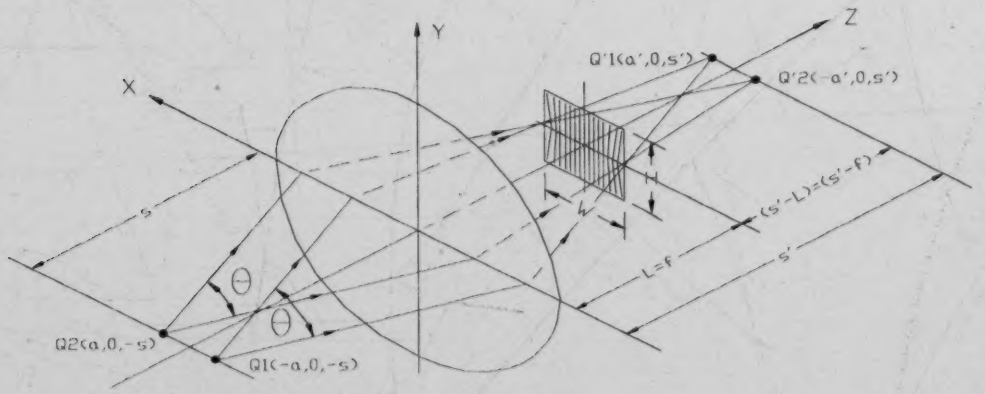

Fig. 3.2.2-3 The 3-D model of a Sagnac Interferometer

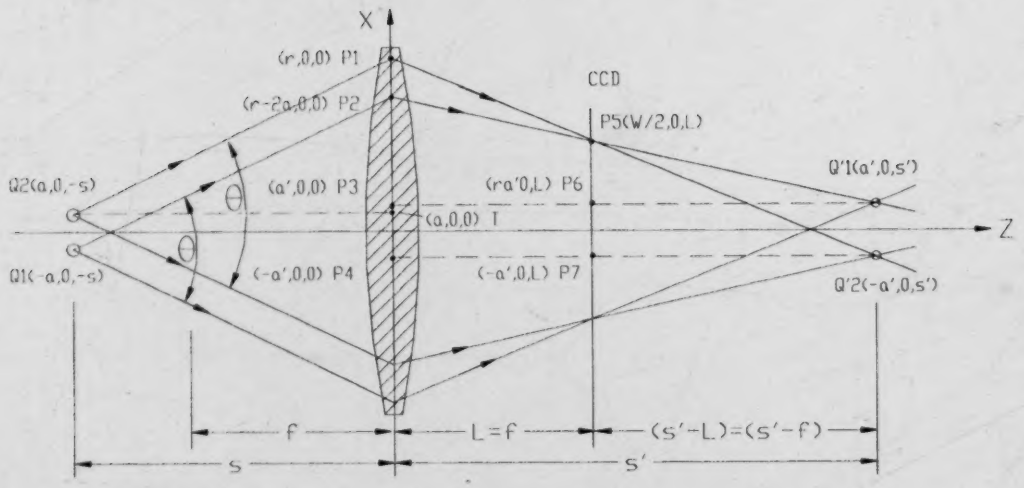

Fig. 3.2.2-4 The 2-D model of Sagnac Interferometer

In Figure 3.2.2-4, a pair of rays, $\overline{Q_2P_1}$ and $\overline{Q_1P_2}$, are in parallel before they reach FT lens. Accoding to simple ray optics these two parallel rays intersect in the focal plane at L = f behind the lens. The FT lens collects the rays from the two virtual light sources at a certain angle θ and produces two wave fronts that interfere at the plane of maximum overlap over a circular region with a diameter W chosen to be the same size as the diagonal dimension of the UV CCD camera. L, θ and W are deduced in the following.

In Figure 3.2.2-4, the similarity of the triangles $\Delta Q'_1 P_5 P_6 \cong \Delta Q'_1 P_2 P_3$ and $\Delta Q'_2 P_5 P_7 \cong \Delta Q'_2 P_1 P_4$ give

$$\frac{\overline{P_5P_6}}{\overline{P_2P_3}} = \frac{\overline{Q'_1P_6}}{\overline{Q'_1P_3}} \text{ and } \frac{\overline{P_5P_7}}{\overline{P_1P_4}} = \frac{\overline{Q'_2P_7}}{\overline{Q'_2P_4}} \qquad (3.2.2 - 1)$$

as $\overline{Q'_1 P_6} = \overline{Q'_2 P_7} = s'-L$ and $\overline{Q'_1 P_3} = \overline{Q'_2 P_4} = s'$, equation (3.2.2 - 1) can be rewritten

$$\frac{\frac{W}{2}-a'}{(r-2a)-a'} = \frac{s'-L}{s'} \qquad (3.2.2 - 2)$$

$$\frac{\frac{W}{2}+a'}{r+a'} = \frac{s'-L}{s'} \qquad (3.2.2 - 3)$$

The simple lens formula gives

$$\frac{1}{s}+\frac{1}{s'} = \frac{1}{f} \qquad (3.2.2 - 4)$$

$$M = \frac{s'}{s} = \frac{s'-f}{f} \quad \frac{f}{s-f} \qquad (3.2.2 - 5)$$

one can get

$$a' = Ma = \frac{s'-f}{f}a = \frac{f}{s-f}a \qquad (3.2.2 - 6)$$

For given W, a, r and f, equation (3.2.2 - 2), (3.2.2 - 3) and (3.2.2 - 6) give (Note: It is easy to deduce by using s instead of s').

$$\boxed{L = f} \qquad (3.2.2 - 7)$$

$$\boxed{W = \frac{f}{s}(2r-2a)} \qquad (3.2.2 - 8)$$

$$\boxed{\tan(\frac{\theta}{2}) = \frac{W}{2f}} = \frac{\overline{P_1 T}}{\overline{Q_2 T}} = \frac{r-a}{s} \qquad (3.2.2 - 9)$$

According to the principle of reversibility, Q'_1 and Q'_2 can be thought as two light sources while Q_1 and Q_2 are their corresponding images. In this way, the equation (3.2.1 - 4), $x_i = \frac{m_i \lambda z}{2a}$, can be rewritten in a new coordinate as

$$x_i = \frac{m_i \lambda (s'-f)}{2a'} \qquad (3.2.2 - 10)$$

Because of $\frac{s'-f}{a'} = \frac{f}{a}$ from equation (3.2.2 - 6), (3.2.2 - 10) can be rewritten as

$$\boxed{x_i = \frac{m_i \lambda f}{2a}} \qquad (3.2.2 - 11)$$

which gives the fringe spacing Δx

$$\boxed{\Delta x = \frac{\lambda f}{2a}} \qquad (3.2.2 - 12)$$

The physical meanings of equations (3.2.2-7), (3.2.2-8), (3.2.2-9) are as follows.

(1) The equation $\boxed{L = f}$ indicates that the plane of maximum overlap is at the focal plane of FT lens. At this position, the CCD camera can obtain a fringe pattern with a good visibility. Any offset from this position will give poor fringe visibility as can be seen from the experimental data to be shown in Section 3.4.2.

(2) The equation $\boxed{W = \frac{f}{s}(2r - 2a) \cong \frac{f \times (2r)}{s}}$ means that the size of the interference fringe pattern at the focal plane of FT lens is determined by the focal length of the FT lens, f, the diameter of the illuminated region of the FT lens, 2r, and the distance from light source to the lens s.

(3) The equation $\boxed{\tan(\frac{\theta}{2}) = \frac{W}{2f}}$ gives a very important result that the input collecting angle of Sagnac interferometer for imaginary sources at the front focal plane of the lens is determined by the size of the UV CCD camera and the focal length of FT lens. Instinctively, the input collecting angle θ was usually thought as $\tan(\frac{\theta}{2}) = \frac{r}{s}$. A typical input collecting angle for our system is calculated here.

$$\theta = 2\arctan(\frac{W}{2f}) = 2\arctan(\frac{28.5mm}{2*300mm}) = 5.46^{\circ}$$

(4) The equation $\boxed{x_i = \frac{m_i \lambda f}{2a}}$ has the following meaning. As the imaginary source distance is not in these equations, it does not affect the spacing of the fringes. This can be seen during the alignment of Sagnac interferometer when the light source is moved back and forth along the optical axis. The fringe spacing remains the same on the screen of UV CCD.

The fringe spacing varies inversely proportional to the separation of the two virtual light sources a, or the offset of the movable mirror d ($a = \sqrt{2}d$), and is proportional to the focal length for a given wavelength. The experimental data to be shown in Figure 3.4.1-6 confirm this formula. We will refer to the equation $\boxed{x_i = \frac{m_i \lambda f}{2a}}$ or $\boxed{\Delta x = \frac{\lambda f}{2a}}$ as the fringe spacing formula.

3.2.3 Theoretical resolution

The theoretical resolution of the Sagnac Interferometer can be derived from the Discrete Fourier Transform (DFT), $y[x_n] \xleftrightarrow{DFT} Y[m]$, of a chromatic wave $y[x_n] = Ae^{j\frac{2\pi}{\Delta x}x_n}$, where $y[x_n]$ is a sequence of intensities across the fringe pattern taken from the UV CCD camera, $x_n = n\delta$ (n = $-\frac{N}{2}$ ... -1, 0, 1, ... $\frac{N}{2}-1$), and δ is the pixel spacing. $Y[m]$ (m = $-\frac{N}{2}$ ... -1, 0, 1, ... $\frac{N}{2}-1$) is the Fourier Transform of $y[x_n]$, N is the number of pixels in one row and Δx is the spacing between fringes.

$$\Delta x = \frac{\lambda f}{2a} \tag{3.2.3-1}$$

According to the theory of the Discrete Fourier Transform [37]

$$Y[m] = \sum_{n=-\frac{N}{2}}^{\frac{N}{2}-1} y[x_n]\, e^{-j\frac{2\pi}{N}mx_n} = \sum A\, e^{j2\pi(\frac{\delta}{\Delta x} - \frac{m}{N})x_n} \tag{3.2.3-2}$$

Assuming that $\frac{\Delta x}{\delta}$ is an integer, the spatial k-vector of the monochromatic input frequency m′ is determined by the relation

$$\frac{\delta}{\Delta x} - \frac{m'}{N} = 0 \tag{3.2.3-3}$$

so,

$$m' = \frac{N\delta}{\Delta x} = \frac{2aN\delta}{\lambda f} = \frac{2aN\delta}{f}\sigma \qquad (3.2.3\text{-}4)$$

where σ is the optical frequency in wave numbers. Under the Nyquist criteria, the minimum resolvable fringe spacing is two pixels, $\Delta x = \frac{\lambda_{min} f}{2a} = 2\delta$, as shown in Fig. 3.2.3-1. Thus, $\lambda_{min} = \frac{4a\delta}{f}$ and $m' = \frac{N}{2}\frac{\lambda_{min}}{\lambda}$

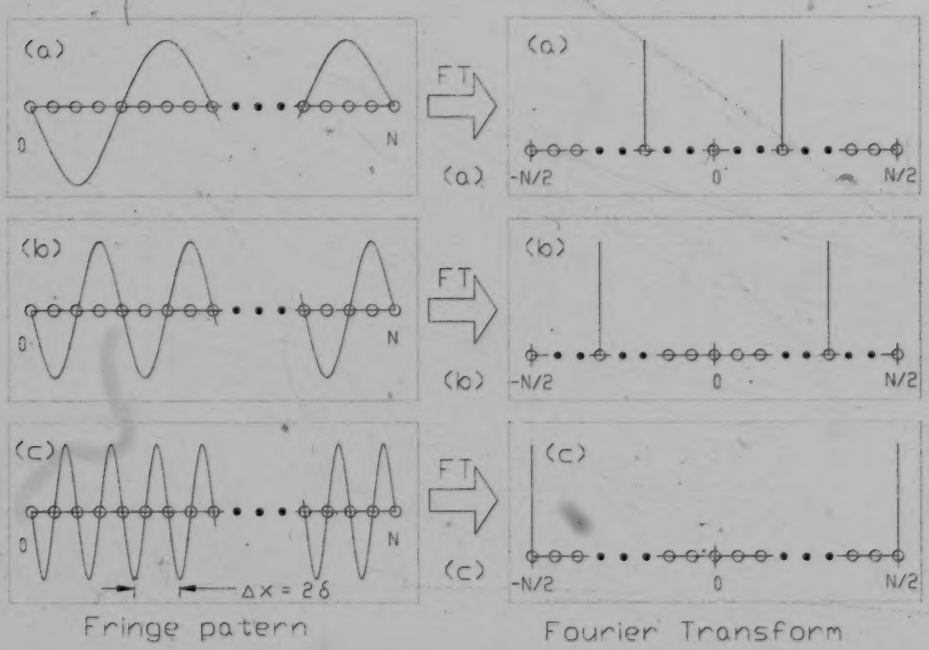

Fig. 3.2.3-1 The fringe spacing and Fourier Transform spectra

$(\Delta x_a > \Delta x_b > \Delta x_c = 2\delta$ gives $\lambda_a > \lambda_b > \lambda_c = \lambda_{min})$

The minimum wavelength λ_{min} which can be measured under the Nyquist criteria is

$$\Delta x = \frac{\lambda_{min} f}{2a} = 2\delta \qquad (3.2.3\text{-}5)$$

The frequency resolution is given by $\Delta m = 1$ which gives

$$\Delta\sigma_{min} = \frac{f}{2\ a\ \delta\ N} = \frac{2}{\lambda_{min} N} \qquad (3.2.3\text{-}6)$$

For any measured wavelength λ the corresponding wavelength resolution is $\frac{\lambda_{min}}{\lambda} = \frac{\sigma_{min}}{\sigma} = \Delta\sigma_{min}\lambda = \frac{2}{N}\frac{\lambda}{\lambda_{min}}$. It can be seen form equation (3.2.3-6) that the maximum resolution of the Sagnac interferometer is determined by the number of pixels per row, N, of the UV CCD camera and the minimum wavelength λ_{min} to be measured. In the application of Raman spectroscopy, this minimum wavelength can be assumed to be the wavelength of the exciting laser. Thus, in order to obtain a high resolution, a large number pixels per row of the CCD camera should be used. It can be seen that using shorter exciting wavelengths has the disadvantage of decreasing the frequency resolution.

Section 3.3 The characteristics of the Sagnac interferometer

Before running the experiments to obtain FT Raman spectra, it is necessary to study the characteristics of the Sagnac interferometer in detail. Both the resolution and fringe visibility are related to the position of the movable mirror. The UV CCD camera has to be placed at the focal plane of FT lens. The chromatic aberration of the FT lens must also be taken into account for the wavelength calibration. All these characteristics of Sagnac interferometer are investigated quantitatively by using an Oriel Hg discharge lamp. Its spectrum is shown in Figure 3.3-1.

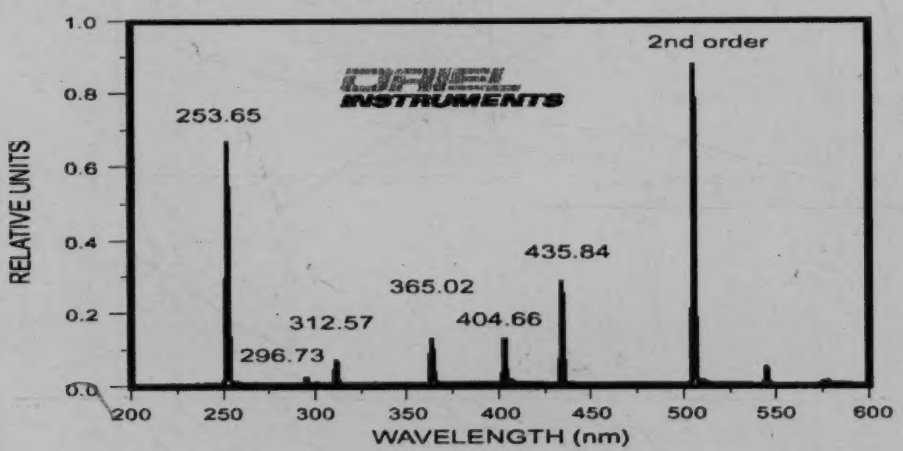

Fig. 3.3-1 The Oriel Hg discharge lamp spectra measured with a spectrometer

The Fourier Transform domain is defined in $(-\nu_c - \nu_c)$, where ν_c is the cut-off frequency based on Nyquist limitation. Since $(-\nu_c - 0)$ and $(0 - \nu_c)$ both give the same symmetric spectra, the spectra can be represented by either one of them. The spectrum in the $(-\nu_c - 0)$ half region is more convenient for viewing the data since the short wavelengths are on the left side while the longer wavelengths are on the right side. This half spectrum will be used through all the following to present the experimental data.

3.3.1 Mercury spectra for different positions of the movable mirror

The position of the movable mirror determines the fringe spacing and resolution of FT spectrum. A series of FT Hg spectra are obtained by scanning the movable mirror. One of these spectra is plotted in Figure 3.3.1-1, others are given in Appendix D and a 3-D plot of the resultant spectra versus mirror position is given in Figure 3.3.1-2. Because of Nyquist criterion, the line at 253.64 nm is aliased with the movable mirror at 12.000mm and thus initially shifts backwards with position towards the cutoff frequency, $-\nu_c$, instead of following the increasing trend. Table 3.3.1-1 gives a summary of data from these spectra.

The spacing of the fringe pattern (cycles/pixel) @ 253.65nm	The spacing of the fringe pattern (pixels/cycle)	The position of the movable mirror relative to its equilibrium position (mm)	The theoretical calculation of the position of the movable mirror(mm)	The position of the movable mirror (mm)	253.65nm at FFT domain (Ni/N)	The minimum wavelengh (nm)	The theoretical resolution with 1024 pixel(cm-1)
0.0305	32.800	0.116	0.118	13850			
0.0427	23.409	0.166	0.165	13800	-0.046	23.3	839
0.0559	17.900	0.216	0.216	13750	-0.060	30.2	646
0.0692	14.450	0.266	0.268	13700	-0.074	37.7	519
0.0823	12.150	0.316	0.319	13650	-0.088	44.6	438
0.0962	10.400	0.366	0.372	13600	-0.102	51.5	379
0.1087	9.200	0.416	0.421	13550	-0.116	59.0	331
0.1212	8.250	0.466	0.469	13500	-0.130	65.9	296
0.1471	6.800	0.566	0.570	13400	-0.158	80.3	243
0.1724	5.800	0.666	0.668	13300	-0.186	94.1	207
0.2000	5.000	0.766	0.775	13200	-0.213	108.0	181
0.2273	4.400	0.866	0.880	13100	-0.241	122.4	160
0.2500	4.000	0.966	0.968	13000	-0.269	136.2	143
0.2778	3.600	1.066	1.076	12900	-0.296	150.1	130
0.3030	3.300	1.166	1.174	12800	-0.324	164.5	119
0.3279	3.050	1.266	1.270	12700	-0.352	178.3	110
0.3529	2.833	1.366	1.367	12600	-0.380	192.7	101
0.3830	2.611	1.466	1.483	12500	-0.408	207.1	94
0.4082	2.450	1.566	1.581	12400	-0.436	221.0	88
0.4348	2.300	1.666	1.684	12300	-0.463	234.8	83

Table 3.3.1-1 Results from the FT Hg spectra by scanning the movable mirror

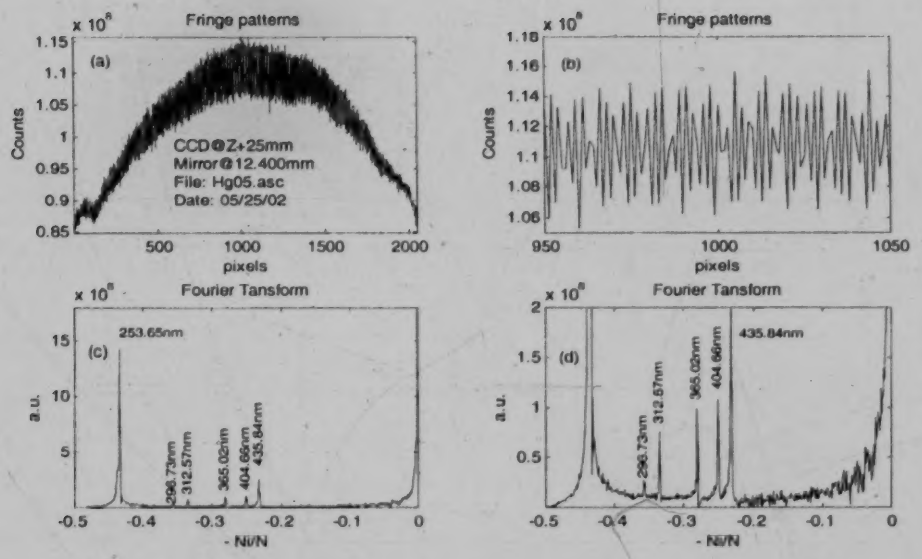

Fig. 3.3.1-1 FT Hg spectra for the movable mirror at a position of 12.40 mm

(a) Fringe pattern (b) Detailed fringe pattern

(c) Hg lamp spectrum (d) Expanded Hg lamp spectrum

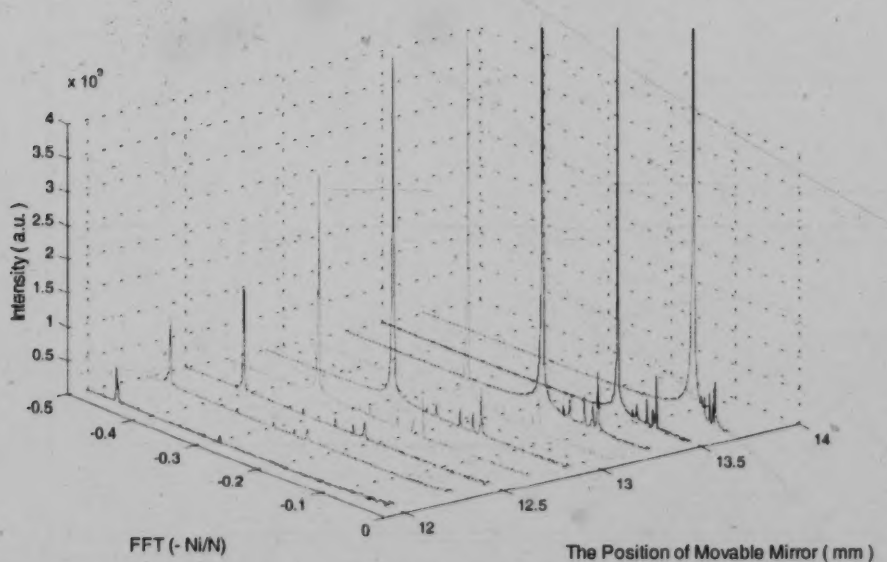

Fig. 3.3.1-2 The 3-D plot of the FT Hg spectra vs. the position

of the movable mirror

The equilibrium position of the movable mirror is defined as the position where the fringe spacing becomes infinite and thus no fringes show up on the screen of the UV CCD camera. As the movable mirror is moved far away from this equilibrium position, the fringes become more tightly spaced. But, it is almost impossible to find out this equilibrium position by adjusting the movable mirror. The intercept determined from the experimental data is used to determine its value as 13.9660mm ± 0.0005 mm in Figure 3.3.1-3.

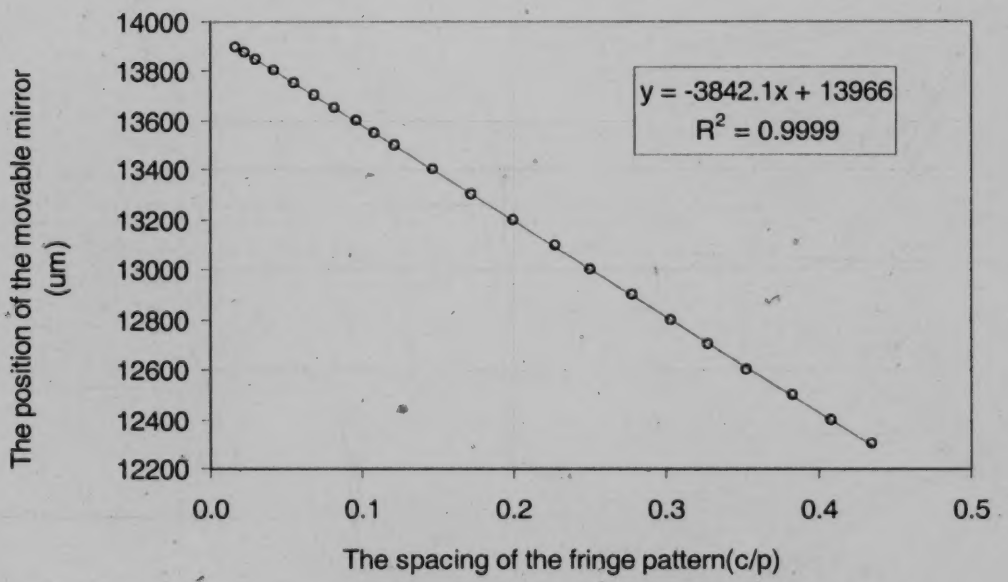

Fig. 3.3.1-3 Fringe spacing versus position of the movable mirror

The minimum measurable wavelength λ_{min} is given by Nyquist criteria which is the wavelength given by ν_c on the 3-D plot in Figure 3.3.1-3 and is also listed in Table 3.3.1-1. It is calculated by $\lambda_{min} = \frac{N_i}{N} \times \lambda_i$, where λ_{min} is the minimum measurable

wavelength, λ_i is a known wavelength such as 253.65 nm, N_i is the position of the known wavelength in the FFT domain and N is the FFT channel number corresponding to ν_c. As mentioned earlier in Section 3.2.3, the resolution is given by $\Delta\sigma_{min} = \frac{2}{N\lambda_{min}}$ and this is plotted in Figure 3.3.1-4

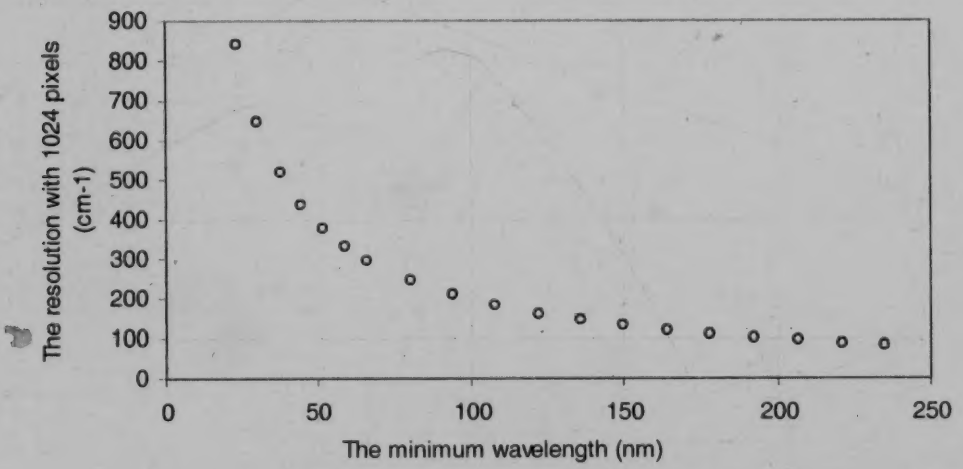

Fig. 3.3.1-4 The resolution vs. the minimum measurable wavelength

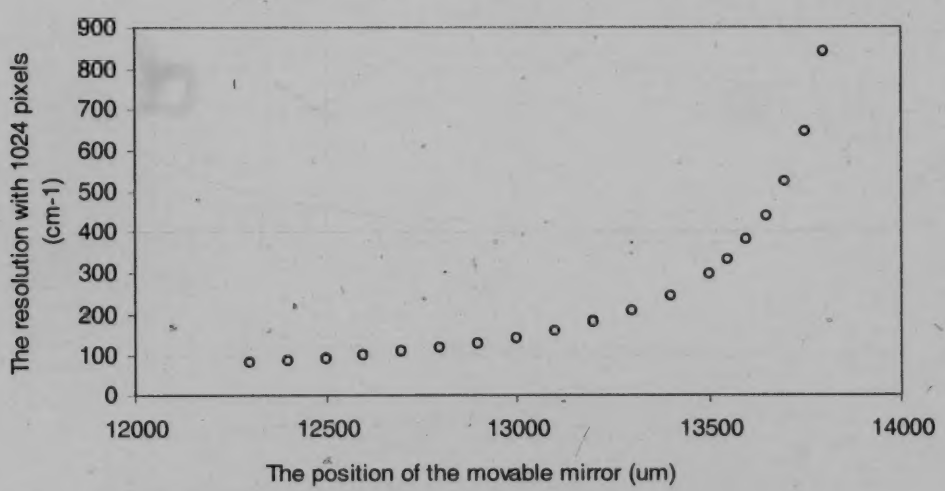

Fig. 3.3.1-5 The resolution vs. the position of the movable mirror

Practically, It is more convenient to relate the resolution to the position of the movable mirror instead of the minimum measurable wavelength as shown in Figure 3.3.1-5.

The fringe spacing formula of Sagnac interferometer as derived in Section 3.2.2 is $\Delta x = \frac{\lambda f}{2\sqrt{2}d}$, where Δx, f, λ and d are the spacing of the fringes, the focal length of the FT lens, the wave length and the off-set of the movable mirror. A comparison of the experimental data and theory is given in Figure 3.3.1-6. It can be seen that theory and experiment agree very well.

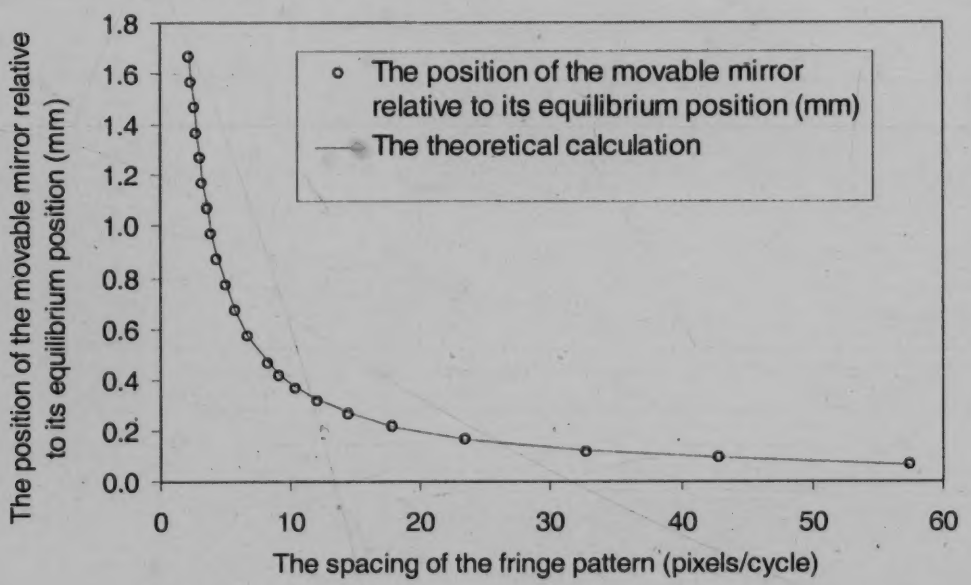

Fig. 3.3.1-6 The comparison of the theoretical and the experimental results for the relation of mirror offset and fringe spacing

3.3.2 The position of the UV CCD camera

As the theory predicts in Section 3.2, the UV CCD camera has to be placed at the focal plane of FT lens. This is confirmed by the experimental results in that there exists a position for the UV CCD camera that gives a good Hg spectrum. Other positions off-set from this optimum positions will give a weaker deformed Hg spectrum. However, the simple lens used for the present experiments has significant chromatic aberration leading to a wavelength dependent focal length. Thus the optimum camera position depends on the wavelength observed.

A set of FT Hg spectra is obtained by scanning the UV CCD camera along its optical axis around the position of the focal plane of the FT lens. One of spectra is shown in Figure 3.3.2-1, while the others are given into Appendix E. In Figure 3.3.2-2, a 3-D plot clearly shows that the FT Hg spectrum is very sensitive to the position of the detector. For the shorter wavelengths, such as 253.64nm line, the amplitude decrease as the UV CCD camera moves farther away from the FT lens while the amplitude of the longer wavelengths, such as 435.84 nm line, increases. The reason is that the refractive index is a function of wavelength. The lens has a shorter focal length for the shorter wavelengths and a longer focal length for the longer wavelengths. This set of the Hg spectrum can help to set up the position of the UV CCD camera. Comparing the ratio of the lines of the Hg spectrum in Appendix C with the Oriel Hg spectrum in Figure 3.3-1 for broad band spectroscopy, the UV CCD camera should be fixed to a position that its FT Hg spectrum has the same line ratios as the reference Hg spectrum.

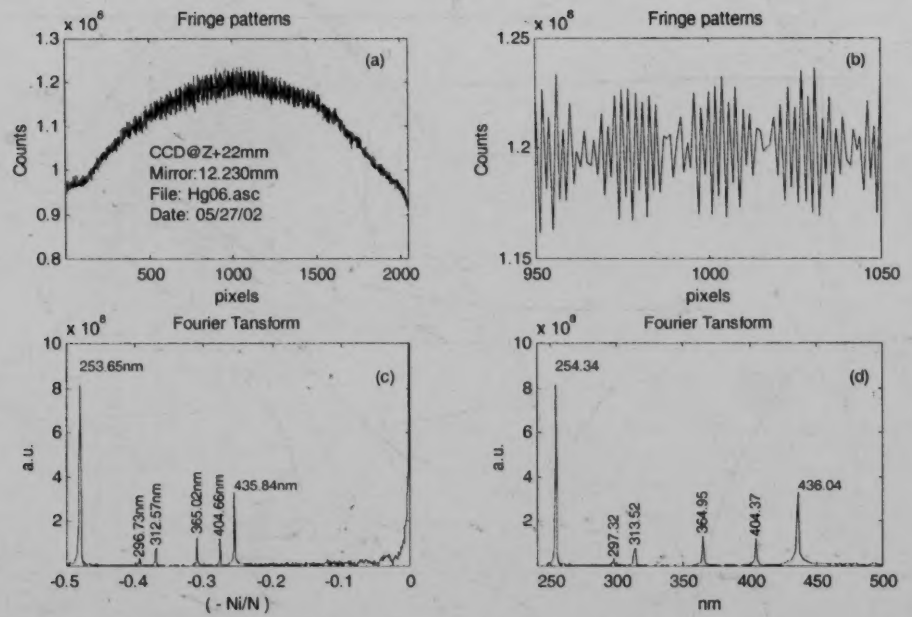

Fig. 3.3.2-1 FT Hg spectrum for one position (z = 12.230 mm) of the UV CCD camera

(a) Fringe pattern (b) Detailed fringe pattern (c) Hg lamp spectrum (d) Detailed Hg lamp spectrum

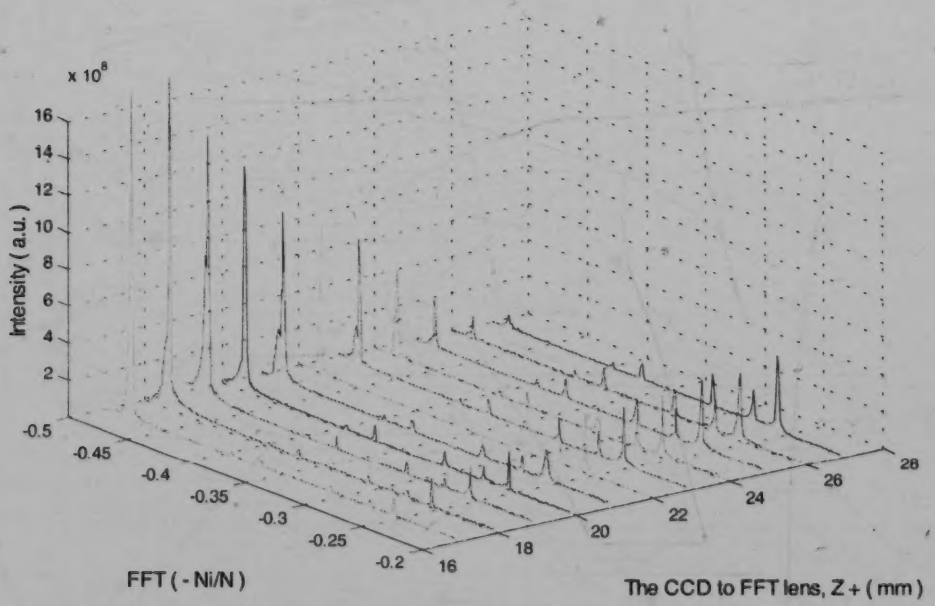

Fig. 3.3.2-2 The 3-D plot of the FT Hg spectrum vs. the position of UV CCD

3.3.3 The calibration of wavelength or wave number

Before the calibration of wavelength or wave number, the FFT spectrum is in the scaled range of ($-\nu_c$ - 0) as shown in Figure 3.3.1-1. The spectrum is meaningful only after calibration in terms of wavelength or wave number. The calibration is based on measuring well known wavelengths, such as a laser line or a couple of well known lines of a spectrum, such as a Hg lamp. The wavelength calibration with a single line of Hg lamp 253.65 nm was carried out by using the linear relation of $\lambda_i = \frac{N_{Hg}}{N_i}\lambda_{Hg}$, where N_i and λ_i are the spectral data array in FFT domain $[i = 0-(N-1)]$ and the calibrated wavelength, λ_{Hg} is the Hg lamp 253.65nm line and N_{Hg} is its corresponding point in FFT domain. But, it can be seen in Figure 3.3.3-1 that the simple linear calibration gives a large difference between the measured wavelength of the other Hg lines and the calibrated wavelength. A large part of the difference is due to the chromatic aberration of the lens. By taking into account the variation of refractive index versus wavelength (Equation 2.1-2) and the resultant varying focal length as a function of wavelength, f_i, give (Equation 2.1-3), a correction can be made to the wavelength calibration given by $\lambda_i = \left(\frac{f_{Hg}}{f_i}\right)\times\left(\frac{N_{Hg}}{N_i}\right)\times\lambda_{Hg}$. The resultant wavelength error has been reduced from 10% to 1.5% by using this corrected formula.

The best accuracy was obtained by using multiple-lines of the Hg lamp, 253.65nm, 296.73mn, 312.57nm, 365.02nm, 404.66nm, 435.84nm, and a least squares

fitting. As shown in Figure 3.3.3-2, the error is reduced to 0.8% which is much better than the single line calibration.

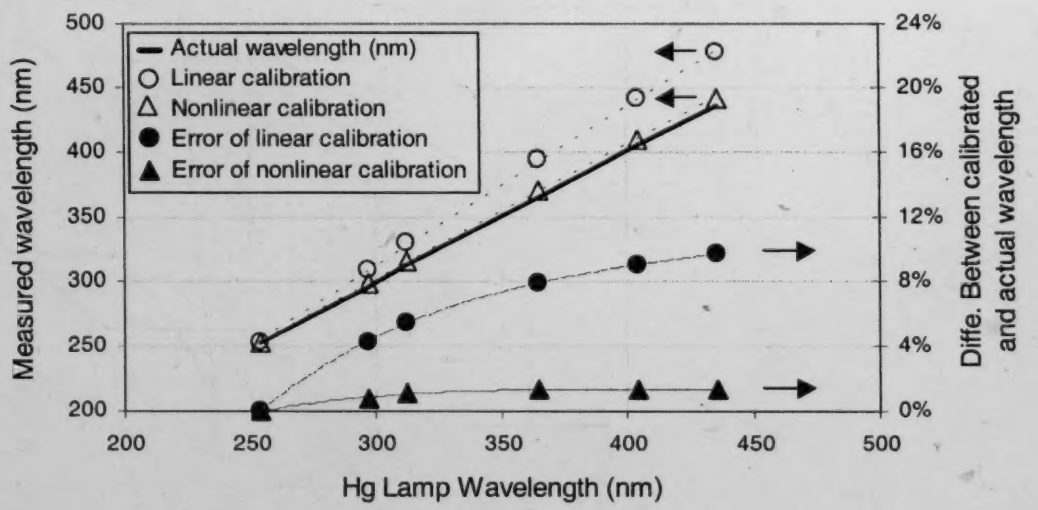

Fig. 3.3.3-1 The wavelength calibration based on the single 253.65nm line of Hg lamp. Both a simple linear and a nonlinear fit (open) and error in calibration (solid) are shown

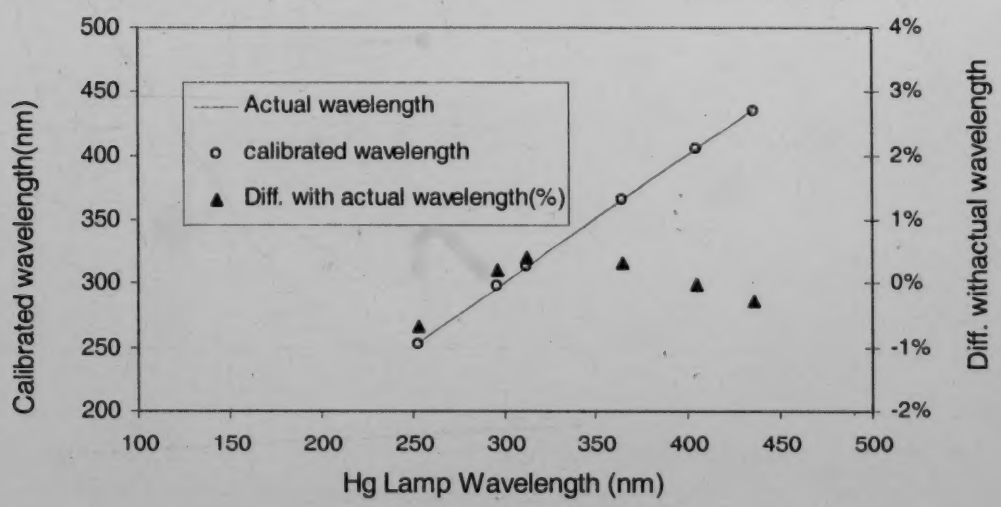

Fig. 3.3.3-2 The wavelength calibration by using a least squares fitting of the multiple-lines of the Hg lamp

3.3.4 The visibility versus the spacing of the fringe

The visibility of interference fringe pattern, defined by $V = \frac{I_{max} - I_{min}}{I_{max} + I_{min}}$, is an important parameter because it determines the signal-to-noise ratio of the FT Raman spectra. The following study shows that it is a function of the fringe spacing given by pixels per cycle.

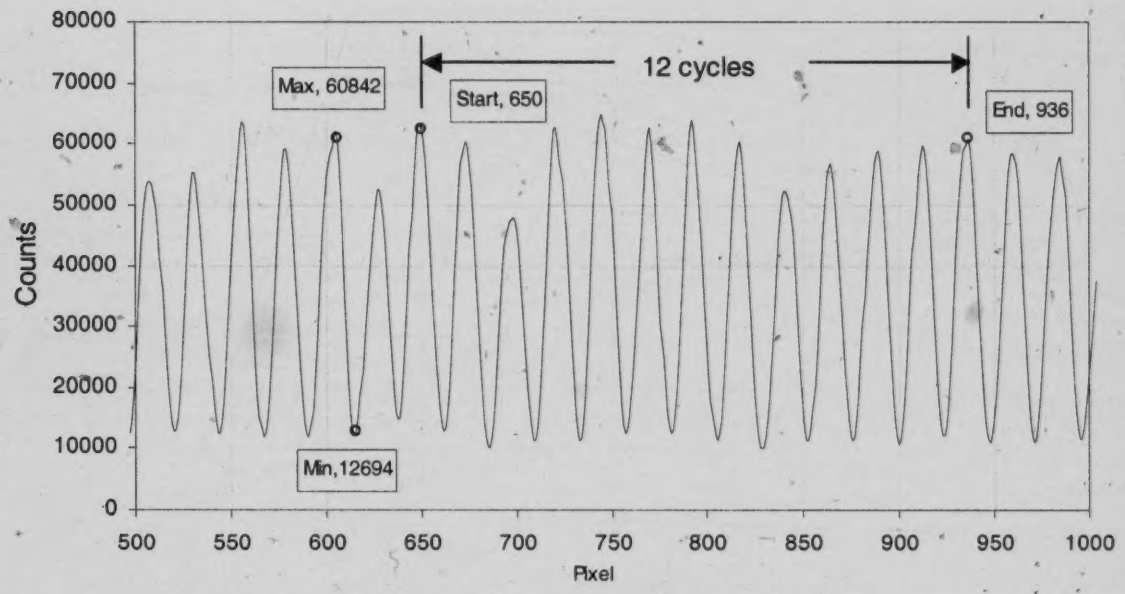

Fig. 3.3.4-1 Teflon Rayleigh and Raman fringe patterns from 266 nm laser pulse excitation

A single wavelength input signal, normally Rayleigh scattering of some sample, is analyzed by the Sagnac interferometer. Its fringe pattern is a sinusoidal wave as shown

in Figure 3.3.4-1. When the position of the movable mirror is changed, the spacing between the two adjoining peaks changes, and the fringe visibility changes also. For each movable mirror position, the maximum I_{max} and the minimum I_{min} of the fringes are measured. Instead of just one cycle, a number of cycles are taken into account to decrease the error in the spacing of fringe pattern. For example, the visibility and the spacing of fringe in Figure 3.4.4-1 are $V = \frac{I_{max} - I_{min}}{I_{max} + I_{min}} = \frac{60842 - 12694}{60842 + 12694} = 0.6548$ and $S = \frac{936 - 650}{12} = 23.83$ pixels/fringe, respectively. The visibility and the spacing are then calculated for a series of movable mirror positions and summarized in Table 3.3.4-1.

Movable Mirror Position(mm)	Pixels per cycle(p/c)	Fringe Visibility	Maximum of Fringe	Minimum of Fringe	End of Fringes	Beginning of Fringes	Cycles
13900	60.6000	0.74	106342	15691	1227	15	20
13875	43.0000	0.70	99122	17595	885	25	20
13850	33.9500	0.69	70226	12839	695	16	20
13825	27.3000	0.70	91512	16384	573	27	20
13800	23.2500	0.65	98080	20603	489	24	20
13750	17.6500	0.69	99441	18231	364	11	20
13700	14.6000	0.65	95545	20120	809	517	20
13650	12.1500	0.65	71481	15270	757	514	20
13600	10.4500	0.63	90847	20929	721	512	20
13550	9.2000	0.59	70074	18285	786	602	20
13500	8.2000	0.59	76558	19642	770	606	20
13400	6.7500	0.53	103725	31427	842	707	20
13300	5.7500	0.45	80638	30319	817	702	20
13200	5.0500	0.43	71692	28284	803	702	20
13100	4.4000	0.39	70910	31290	792	704	20
13000	3.9500	0.35	62707	29933	780	701	20
12900	3.6000	0.30	68056	36325	875	803	20
12800	3.3000	0.27	55803	32324	868	802	20
12700	3.0500	0.23	60727	37843	862	801	20
12600	2.8000	0.19	58605	40024	857	801	20
12500	2.6000	0.16	52760	38118	855	803	20
12400	2.4500	0.15	65166	48480	851	802	20
12300	2.3000	0.13	60859	47272	847	801	20

Table 3.3.4-1 The visibility vs. the fringe spacing of Teflon Rayleigh scattering

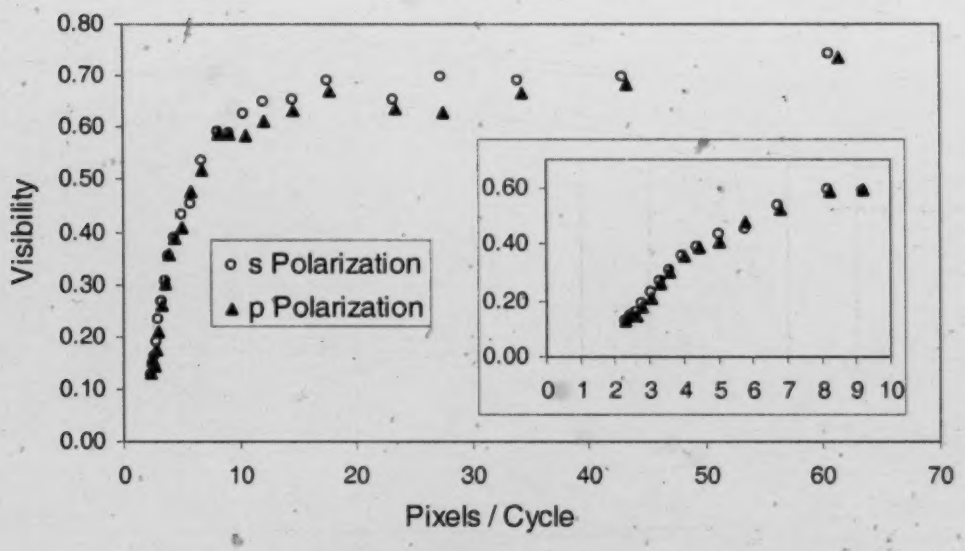

Fig. 3.3.4-2 The fringe visibility vs. the fringe spacing of single shot Teflon Rayleigh scattering

Figure 3.3.4-2 shows the visibility as a function of the spacing of the fringe pattern for Rayleigh scattering of Teflon. The results are shown for both s-polarization (perpendicular to the plane of incidence) and p-polarization(horizontal, or in the plane of incidence). As one can see in Figure 3.3.4-2, the visibility starts at approximately 0.7 and then decreases at some point when the fringe spacing decreases. The reason comes from the aberrations of FT lens and the pixel size used for signal sampling. When the fringe spacing is much larger than the aberration spot size of the lens a clearly resolved sinusoidal spatial modulation is observed. As the fringe spacing approaches the blur spot size of the lens, the peak of sinusoidal wave will decrease because the pixel takes an average value of the peak and its surrounding blur spot area. In this way, the maximum becomes smaller while the minimum becomes larger than their real peak values. Thus,

the visibility decreases as the number of pixels per cycle decreases. At a small number of pixels per cycle, the wavelength resolution is higher but the visibility is poorer. Obviously, there is a trade off between the S/N ratio and the resolution when choosing the number of the pixels per cycle.

An attempt was made to improve the fringe visibility by using a UV doublet lens with diameter of 50mm and focal length of 250mm (CVI L85). The fringe visibility was measured experimentally and the results are shown in Figure 3.3.4-3. The visibility of the doublet lens with 250mm focal length is similar to that of a single lens with 300mm focal length. The doublet used was designed for focusing of a parallel laser beam to a single point on axis and thus may not have been significantly better in the present application where imaging over an extended field of view is required.

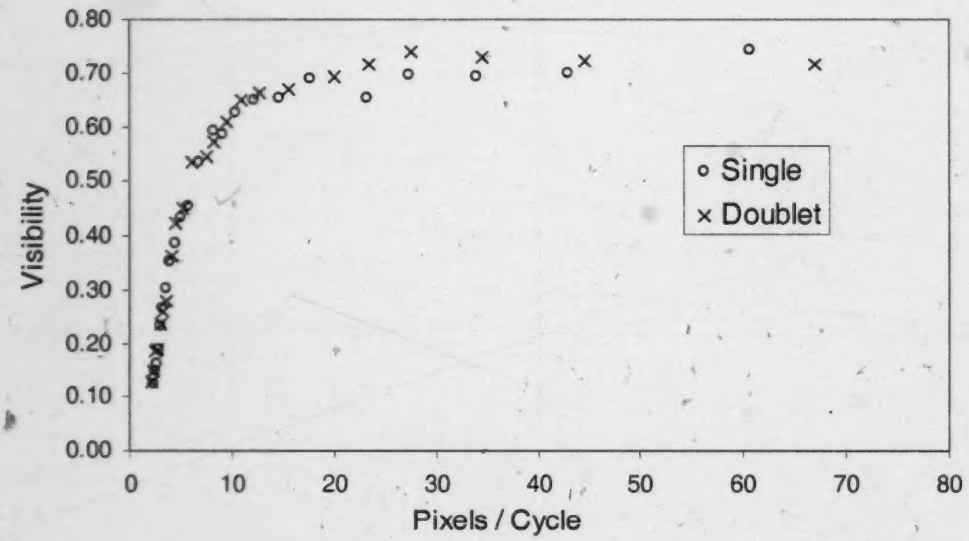

Fig. 3.3.4-3 The visibility vs. the fringe spacing of single shot Teflon Rayleigh scattering, the comparison of a single lens and a Doublet lens for s-polarized light

Section 3.4 Experimental measurements of Raman spectra

The objective of this thesis was to build up and characterize a FT Raman Spectrometer based on a Sagnac Interferometer and to show that it is a useful analysis tool. The performance in measuring Hg spectra and Rayleigh scattering from Teflon has already been shown. Some Raman spectra are now given here, showing that the Sagnac Interferometer indeed can be used for Raman spectroscopy.

These samples are selected from solid, liquid and gas phases. They are Teflon, Water, Methanol, Ethanol, Cyclohexane and air (Nitrogen, Oxygen). For each sample, their fringe pattern, FT Raman spectrum and the corresponding conventional Raman spectrum are given.

In addition, single laser shot, FT Raman spectra of Teflon and Methanol are also demonstrated.

3.4.1 Water (H_2O)

The measured FT Raman spectrum of water is shown in Figure 3.4.1-1 in which (a) is the fringe pattern, (b) is an exploded detailed plot of the fringe pattern, (c) is the measured Fourier Transform Raman spectrum of water and (d) is a conventional Raman spectrum of water with a conventional spectrometer from a reference database [33].

The experimental conditions are chosen as follows. The UV CCD camera is set up to work at a temperature -50°C, the read out time 32 μs and the accumulation number 10,000 shots. Laser energy is set at 2.1mJ and approximately 10 Hz. In accumulate mode, the charge on the CCD array was read out for every laser shot and added to the total signal. Rayleigh scattering was blocked using the UV high pass Raman filter. The scattered light was viewed perpendicular to the direction of the polarization vector of the incident laser light. The Fourier Transform is carried out over a range of 1024 pixels. The movable mirror is at a position 12.230mm, the relative distance is 1.736 mm to its equilibrium position, and the theoretical resolution is 80 cm^{-1} as shown in section 3.3.1. The wave number is calibrated by using multiple lines of the Hg lamp with consideration of chromatic lens aberration whose procedure is described in Section 3.3.3.

In the reference [33] Figure 3.4.1-1(d), the features of the Raman spectrum of water are characterized by a small peak from 1600 cm^{-1} to 1700 cm^{-1}, a large peak from 3000 cm^{-1} to 3700 cm^{-1} with the peak maximum at 3414 cm^{-1} and a small shoulder from the peak maximum to the shorter wave number. All the features of the main peak

show up in the FT Raman spectrum in Figure 3.4.1-1(c). The peak maximum 3417 cm^{-1} of FT Raman spectrum of water is only 0.2 % different than the reference spectrum. Thus, water can be successfully measured by the Sagnac Raman Interferometer.

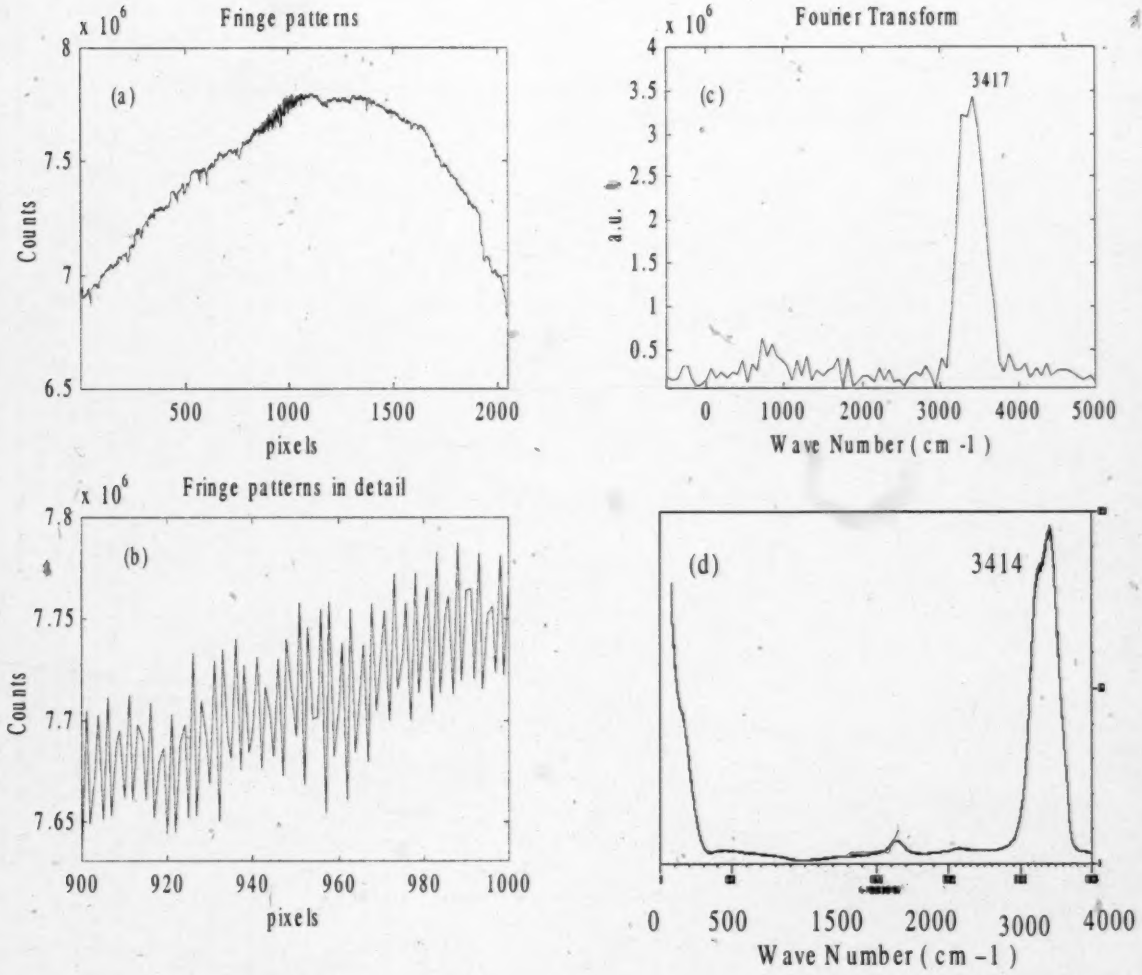

Fig. 3.4.1-1 The fringe pattern of water and its FT Raman spectrum measured with the Sagnac interferometer (10,000 shots) and compared to its conventional Raman spectrum[33]: (a) full fringe pattern, (b) detailed fringe pattern, (c) Fourier Transform spectrum and (d) reference Raman spectrum

3.4.2 Methanol (CH_3OH)

The measured FT Raman spectrum of methanol is shown in Figure 3.4.2-1 in which (a) is the fringe pattern, (b) is an exploded detailed plot of the fringe pattern, (c) is the measured Fourier Transform Raman spectrum of Methanol and (d) is a conventional Raman spectrum of methanol with a conventional spectrometer from a reference database [33].

The experimental conditions are chosen as follows. The UV CCD camera is set up to work at a temperature -50°C, the readout time 32 μs and the accumulation number 10,000 shots. Laser energy is set at 2.1mJ and approximately 10 Hz. In accumulate mode, the charge on the CCD array was read out for every laser shot and added to the total signal. Rayleigh scattering was blocked using the UV high pass Raman filter. The scattered light was viewed perpendicular to the direction of the polarization vector of the incident laser light. The Fourier Transform is carried out over a range of 1024 pixels. The movable mirror is at a position 12.230mm, the relative distance is 1.736 mm to its equilibrium position, and the theoretical resolution is 80 cm^{-1} as shown in section 3.3.1. The wave number is calibrated by using multiple lines of the Hg lamp with consideration of chromatic lens aberration whose procedure is described in Section 3.3.3.

In the reference[33] Figure 3.4.2-1(d), the features of Raman spectrum of Methanol are characterized by its peaks at 1037 cm^{-1}, 1453 cm^{-1}, 2836 cm^{-1} and 2946 cm^{-1}. All these features show up in FT Raman spectrum in Figure 3.4.2-1(c) at 1056 cm^{-1}, 1479 cm^{-1}, 2811 cm^{-1} and 2945 cm^{-1}. The differences between the measured and reference spectral peaks are 1.8%, 1.8%, -0.9% and -0.03%, respectively. The relative

intensity of the peak at 1037 cm^{-1} in the reference spectrum is bigger than the one in FT Raman spectrum. The reason for this is some attenuation from the Raman filter. Thus, the measurement of Methanol by the Sagnac Raman Interferometer is in good agreement with the reference.

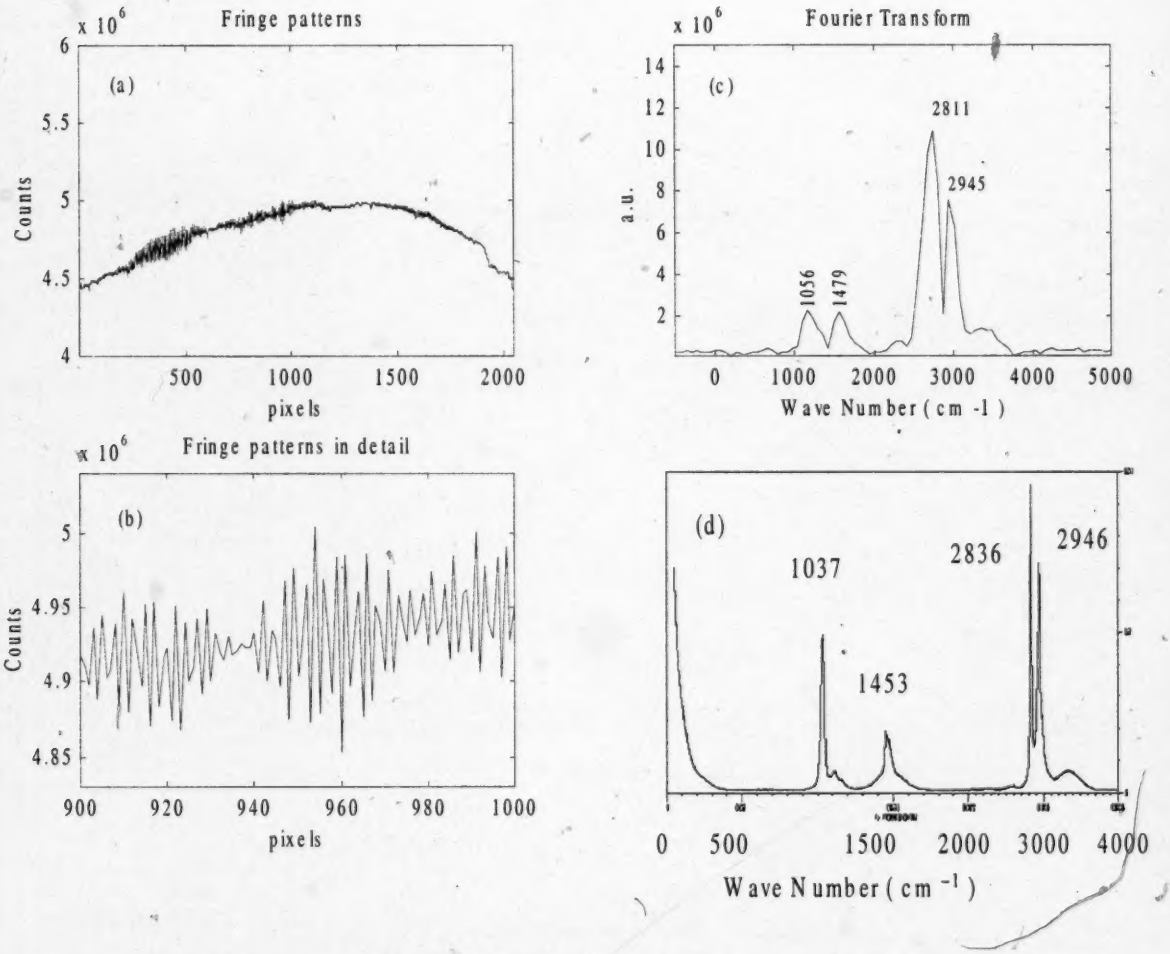

Fig. 3.4.2-1 The fringe patterns of Methanol and its FT Raman spectrum measured with the Sagnac interferometer (10,000 shots) and compared to its conventional Raman spectrum[33]: (a) full fringe pattern, (b) detailed fringe pattern, (c) Fourier Transform spectrum and (d) reference Raman spectrum

Methanol by a single laser shot

The measured FT Raman spectrum of methanol by a single laser shot is shown in Figure 3.4.2-2 in which (a) is the fringe pattern, (b) is an exploded detailed plot of the fringe pattern, (c) is the measured Fourier Transform Raman spectrum of methanol and (d) is a conventional Raman spectrum of methanol with a conventional spectrometer from a reference database [33].

The experimental conditions are chosen as follows. The UV CCD camera is set up to work at a temperature -50°C, the readout time 32 μs and the accumulation number 1 shot. Laser energy is set at 2.1mJ. Rayleigh scattering was blocked using the UV high pass Raman filter. The scattered light was viewed perpendicular to the direction of the polarization vector of the incident laser light. The Fourier Transform is carried out over a range of 2048 pixels. The movable mirror is at a position 13.600 mm, the relative distance is 0.3660 mm to its equilibrium position, and the theoretical resolution is 189 cm^{-1} as shown in section 3.3.1. The wave number is calibrated by using multiple lines of the Hg lamp with consideration of chromatic lens aberration whose procedure is described in Section 3.3.3.

In the reference [33] Figure 3.4.2-2(d), the features of Raman spectrum of Methanol are characterized by its peaks at 1037 cm^{-1}, 1453 cm^{-1}, 2836 cm^{-1} and 2946 cm^{-1}. In Figure 3.4.2-2(c), because of the resolution, the peaks in the conventional spectrum at 2836 cm^{-1} and 2946 cm^{-1} are merged to a single peak at 2965 cm^{-1}. Under

the single laser shot condition, the major feature of the FT Raman spectrum of Methanol can be observed by the Sagnac Raman Interferometer.

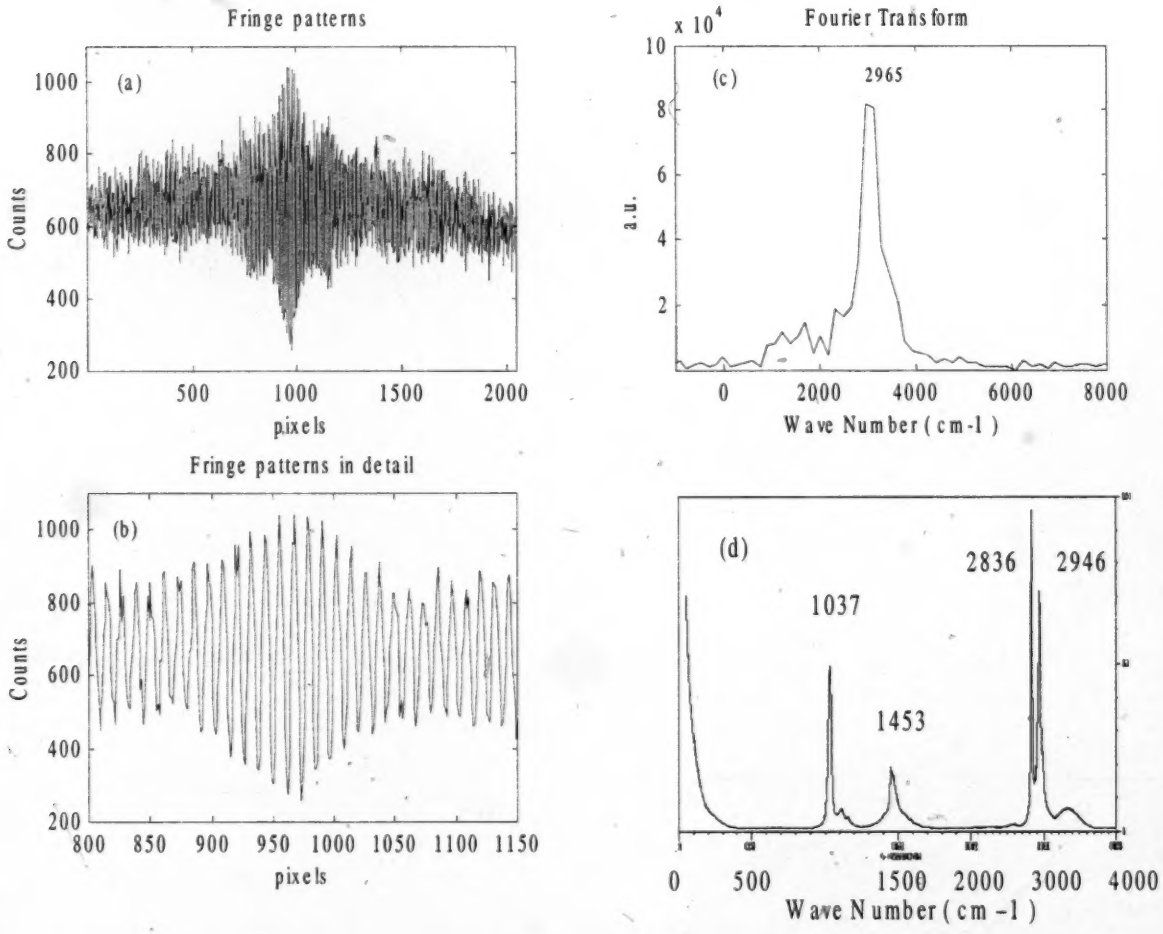

Fig. 3.4.2-2 The fringe patterns of Methanol and its FT Raman spectrum measured with the Sagnac interferometer (single shot) and compared to its conventional Raman spectrum[33]: (a) full fringe pattern, (b) detailed fringe pattern, (c) Fourier Transform spectrum and (d) reference Raman spectrum

3.4.3 Cyclohexane (C_6H_{12})

The measured FT Raman spectrum of cyclohexane is shown in Figure 3.4.3-1 in which (a) is the fringe pattern, (b) is an exploded detailed plot of the fringe pattern, (c) is the measured Fourier Transform Raman spectrum of cyclohexane and (d) is a conventional Raman spectrum of cyclohexane with a conventional spectrometer from a reference database [33].

The experimental conditions are chosen as follows. The UV CCD camera is set up to work at a temperature -50°C, the readout time 32 μs and the accumulation number 10,000 shots. Laser energy is set at 2.1mJ and approximately 10 Hz. In accumulate mode, the charge on the CCD array was read out for every laser shot and added to the total signal. Rayleigh scattering was blocked using the UV high pass Raman filter. The scattered light was viewed perpendicular to the direction of the polarization vector of the incident laser light. The Fourier Transform is carried out over a range of 1024 pixels. The movable mirror is at a position 12.230mm, the relative distance is 1.736 mm to its equilibrium position, and the theoretical resolution is 80 cm^{-1} as shown in section 3.3.1. The wave number is calibrated by using multiple lines of the Hg lamp with consideration of chromatic lens aberration whose procedure is described in Section 3.3.3

In the reference[33] Figure 3.4.3-1(d), the features of Raman spectrum of Cyclohexane are characterized by its peaks at 803cm^{-1}, 1028cm^{-1}, 1267cm^{-1}, 1446cm^{-1}, 2853cm^{-1} and 2938cm^{-1}. All the features show up in FT Raman spectrum in Figure

3.4.3-1(c) at 818 cm^{-1}, 1043cm^{-1}, 1283cm^{-1}, 1461cm^{-1}, 2834cm^{-1} and 2968cm^{-1}. Their differences are 1.9%, 1.5%, 1.3%, 1.0%, -0.7% and 1.0%, respectively. The relative intensity of the peak at 803 cm^{-1} in the reference spectrum is bigger than the one in FT Raman spectrum. The reason for this is attenuation from the Raman filter. Thus, the Sagnac Raman Interferometer also gives a good FT Raman spectrum for Cyclohexane.

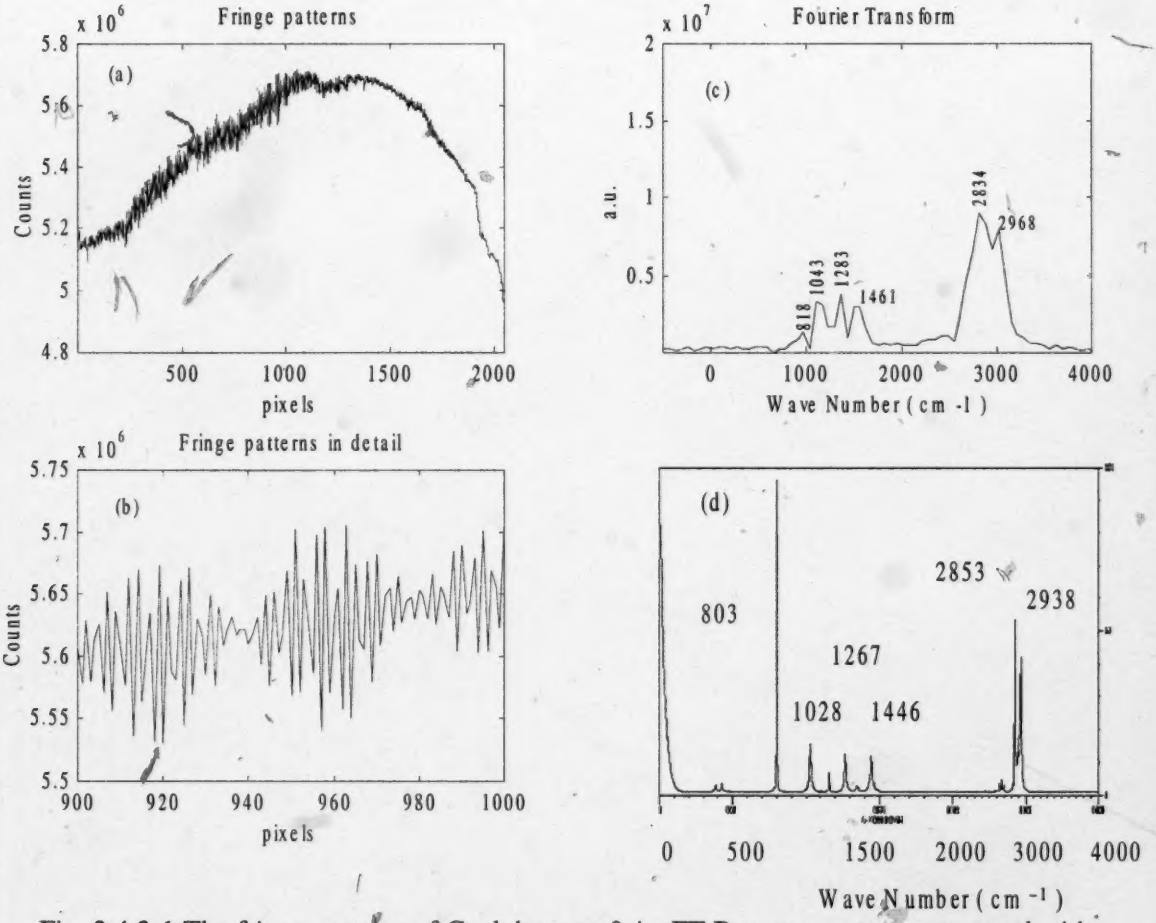

Fig. 3.4.3-1 The fringe patterns of Cyclohexane & its FT Raman spectrum measured with the Sagnac interferometer (10,000 shots) and compared to its conventional Raman spectrum[33]: (a) full fringe pattern, (b) detailed fringe pattern, (c) Fourier Transform spectrum and (d) reference Raman spectrum

3.4.4 Ethanol (CH_3CH_2OH)

The measured FT Raman spectrum of ethanol is shown in Figure 3.4.4-1 in which (a) is the fringe pattern, (b) is an exploded detailed plot of fringe pattern, (c) is the measured Fourier Transform Raman spectrum of ethanol and (4) is a conventional Raman spectrum of ethanol with a conventional spectrometer from a reference database [33].

The experimental conditions are chosen as follows. The UV CCD camera is set up to work at a temperature -50°C, the readout time 32 μs and the accumulation number 10,000 shots. Laser energy is set at 2.1mJ and approximately 10 Hz. In accumulate mode, the charge on the CCD array was read out for every laser shot and added to the total signal. Rayleigh scattering was blocked using the UV high pass Raman filter. The scattered light was viewed perpendicular to the direction of the polarization vector of the incident laser light. The Fourier Transform is carried out over a range of 1024 pixels. The movable mirror is at a position 12.230 mm, the relative distance is 1.736 mm to its equilibrium position, and the theoretical resolution is 80 cm^{-1} as shown in section 3.3.1. The wave number is calibrated by using multiple lines of the Hg lamp with consideration of chromatic lens aberration whose procedure is described in Section 3.3.3.

In the reference[33] Figure 3.4.4-1(d), the features of Raman spectrum of Cyclohexane are characterized by its peaks at 884cm^{-1}, 1063cm^{-1}, 1097cm^{-1}, 1455cm^{-1}, 2878cm^{-1}, 2927cm^{-1} and 2937cm^{-1}. In the FT Raman spectrum in Figure 3.4.4-1(c), only the features at 907cm^{-1}, 1121cm^{-1}, 1473cm^{-1}, and 2951cm^{-1}show up. Their differences

are 2.6%, 2.2%, 1.2% and 0.5% from the closest reference peaks, respectively. The relative intensity of the peak at 884 cm^{-1} in the reference spectrum is bigger than the one in FT Raman spectrum. The reason for this is some attenuation from the Raman filter. Some of the peaks are merged in FT Raman spectrum because of the resolution. Thus, the Sagnac Raman Interferometer can also identify the FT Raman spectrum of Ethanol.

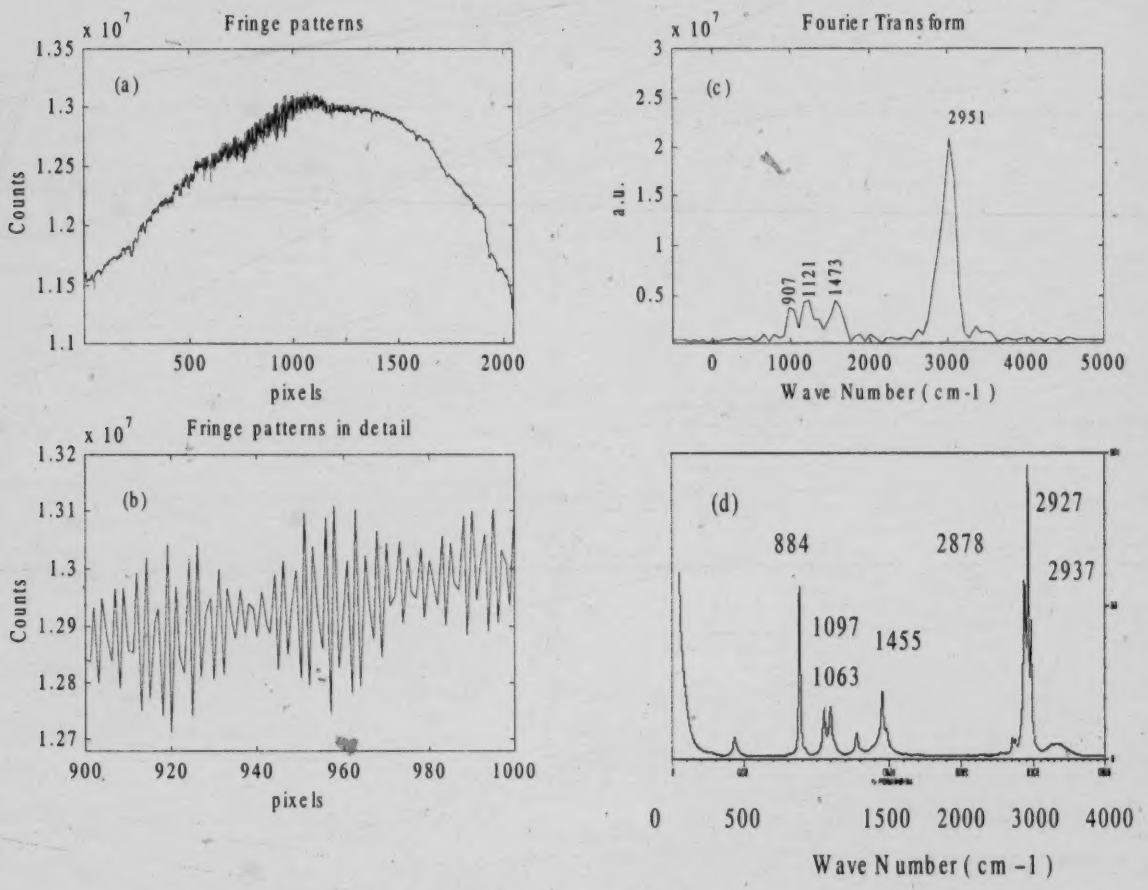

Fig. 3.4.4-1 The fringe patterns of Ethanol & its FT Raman spectrum measured with the Sagnac interferometer (10,000 shots) and compared to its conventional Raman spectrum[33]: (a) full fringe pattern, (b) detailed fringe pattern, (c) Fourier Transform spectrum and (d) reference Raman spectrum

3.4.5 Air

The measured FT Raman spectrum of air is shown in Figure 3.4.5-1 in which (a) is the fringe pattern, (b) is an exploded detailed plot of the fringe pattern, (c) is the measured Fourier Transform Raman spectrum in the wavelength domain and (d) is the FT Raman spectrum.

As a gas sample, air has a much lower molecular density than the solid or liquid samples and the experimental conditions must be extended from those used to solid or liquid samples. The experimental conditions are chosen as follows. The UV CCD camera is set up to work at a temperature -50°C, read out time 32 μs and shutter time 800S. For this case the camera is used in integration mode where all photons are integrated over the 800s exposure and the camera is read out once at the end of this period. The laser was operated at 20 Hz for this case. Laser energy is set at 2.1mJ. Rayleigh scattering was blocked using the UV high pass Raman filter. The scattered light was viewed perpendicular to the direction of the polarization vector of the incident laser light. The Fourier Transform is carried out over a range of 1024 pixels. The movable mirror is at a position 13.100 mm, the relative distance is 0.8660 mm to its equilibrium position, and the theoretical resolution is 160 cm^{-1} as shown in section 3.3.1. The wave number is calibrated by using multiple lines of the Hg lamp with consideration of chromatic lens aberration whose procedure is described in Section 3.3.3.

Although the Signal to Noise ratio is much poor than that of liquid or solid samples, Raman spectra of Oxygen and Nitrogen are still recognizable. The wave numbers for Oxygen and Nitrogen are at 1560cm $^{-1}$ and 2341cm $^{-1}$, respectively. The difference from their reference wave number 1556 cm $^{-1}$ and 2331 cm $^{-1}$ are only 0.3% and 0.4%. Thus, air can be detected by the Sagnac Raman Interferometer.

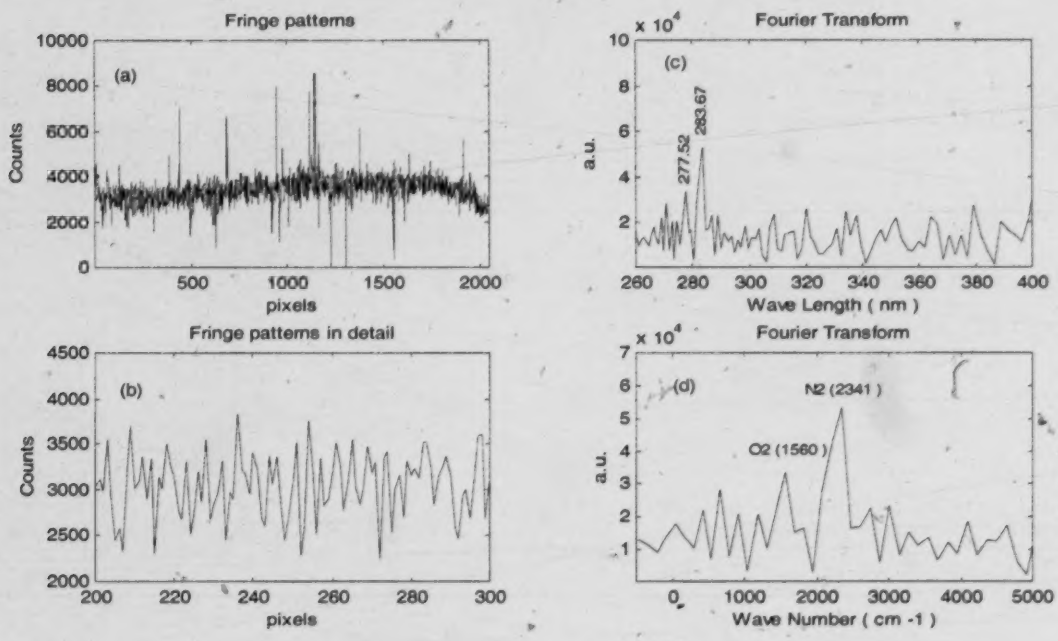

Fig. 3.4.5-1 The fringe patterns of air & its FT Raman spectrum measured with the Sagnac interferometer (16,000 shots): (a) full fringe pattern, (b) detailed fringe pattern, (c) Fourier Transform spectrum in wavelength and (d) Fourier Transform spectrum in wave number

3.4.6 Teflon

The measured FT Raman spectrum of Teflon is shown in Figure 3.4.6-1 in which (a) is the fringe pattern, (b) is an exploded detailed plot of the fringe pattern, (c) is the measured Fourier Transform Raman spectrum of Teflon and (d) is a conventional Raman spectrum of Teflon with a conventional spectrometer which was carried out in our lab and was shown in Figure 2.2-3 previously.

As a solid sample, Teflon has a much larger number density than the gas sample leading to much larger signals. The UV CCD camera is set up to work at a temperature -50°C, the readout time 32 μs and the accumulation number 1,000 shots. Laser energy is set at 2.1mJ. In accumulate mode, the charge on the CCD array was read out for every laser shot and added to the total signal. Rayleigh scattering was blocked using the UV high pass Raman filter. The scattered light was viewed perpendicular to the direction of the polarization vector of the incident laser light. The Fourier Transform is carried out over a range of 1024 pixels. The movable mirror is at a position 12.230mm, the relative distance is 1.736 mm to its equilibrium position, and the theoretical resolution is 80 cm^{-1} as shown in section 3.3.1. The wave number is calibrated by using multiple lines of the Hg lamp with consideration of chromatic lens aberration whose procedure is described in Section 3.3.3.

In the reference [29] Figure 3.4.6-1(d), the features of Raman spectrum of Teflon are characterized by its peaks at 729cm^{-1}, 1215cm^{-1}, 1295cm^{-1}, 1379cm^{-1} and 2679cm^{-1}.

In Figure 3.4.6-1(c), the FT Raman spectrum show these peaks at 742 cm^{-1}, 1397cm^{-1}, and 2678cm^{-1}. Their differences are 1.8%, 1.3% and -0.04% from the closest reference peaks, respectively. These peaks in the conventional spectrum at 1215 cm^{-1}, 1295 cm^{-1}, 1379 cm^{-1} are merged to a single peak at 1397 cm^{-1} because of the lower resolution of the Sagnac Interferometer. The major features of Teflon Raman spectrum are well measured by the Sagnac Raman Interferometer.

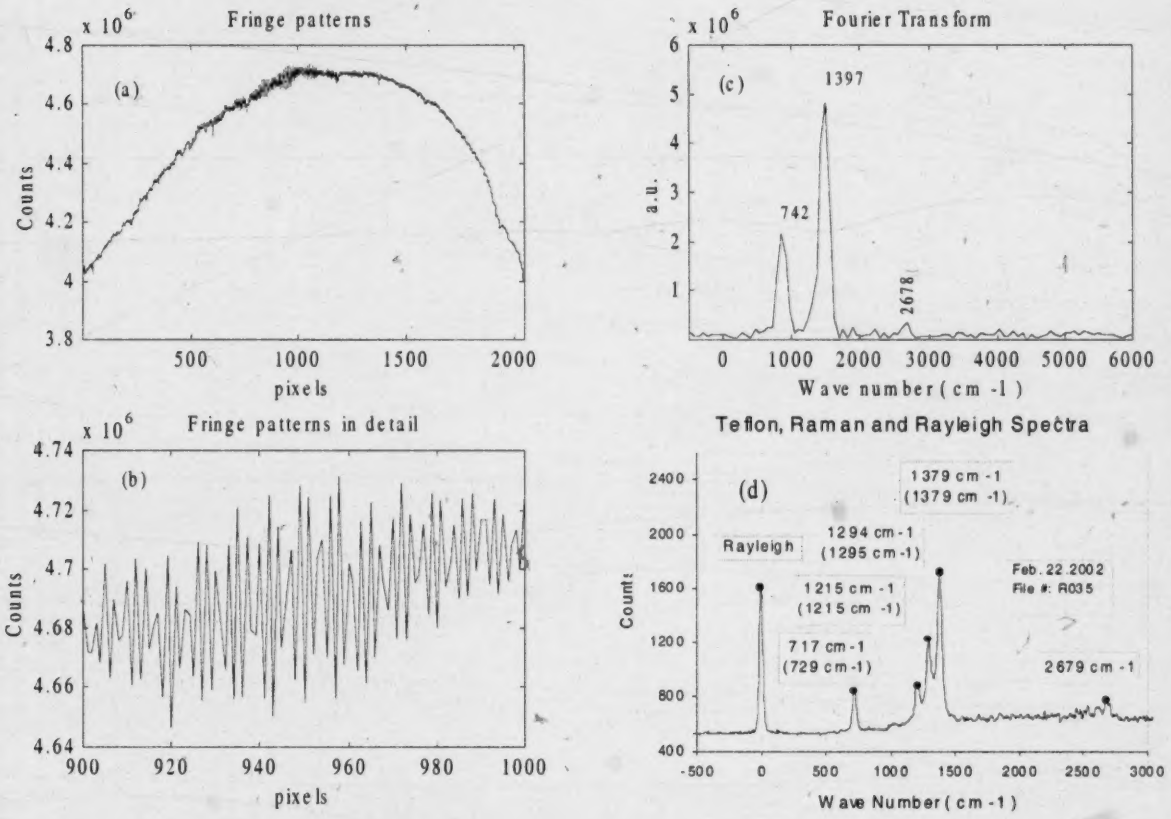

Fig. 3.4.6-1 The fringe patterns of Teflon & its FT Raman spectrum measureed with the Sagnac interferometer (1,000 shots) and compared to its conventional Raman spectrum: (a) full fringe pattern, (b) detailed fringe pattern, (c) Fourier Transform spectrum and (d) reference Raman spectrum

Teflon by a single shot

The measured FT Raman spectrum of Teflon by a single laser shot is shown in Figure 3.4.6-2 in which (a) is the fringe pattern, (b) is an exploded detailed plot of the fringe pattern, (c) is the measured Fourier Transform Raman spectrum of Teflon and (d) is a conventional Raman spectrum of Teflon with a conventional spectrometer which was carried out in our lab and was shown in Figure 2.2-3 previously.

The experimental conditions are chosen as follows. The UV CCD camera is set up to work at a temperature -50°C, the readout time 32 μs and the accumulation number 1 shot. Laser energy is set at 2.1mJ. Rayleigh scattering was blocked using the UV high pass Raman filter. The scattered light was viewed perpendicular to the direction of the polarization vector of the incident laser light. The Fourier Transform is carried out over a range of 2048 pixels. The movable mirror is at a position 13.600 mm, the relative distance is 0.3660 mm to its equilibrium position, and the theoretical resolution is 189 cm $^{-1}$ as shown in section 3.3.1. The wave number is calibrated by using multiple lines of the Hg lamp with consideration of chromatic lens aberration whose procedure is described in Section 3.3.3.

In the reference Figure 3.4.6-2(d), the features of Raman spectrum of Teflon are characterized by its peaks at 729cm^{-1}, 1215cm^{-1}, 1295cm^{-1}, 1379cm^{-1} and 2679cm^{-1}. In Figure 3.4.6-2(c), the FT Raman spectrum show these peaks at 739 cm^{-1}, 1380cm^{-1}, and 2618cm^{-1}. Their differences are 1.4%, 0.1% and -2.3% from the closest reference peaks,

respectively. The peaks in the conventional spectrum at 1215 cm^{-1}, 1295 cm^{-1}, 1379 cm^{-1} are merged to a single peak at 1380 cm^{-1} because of the lower resolution. A single laser shot, FT Raman spectrum of Teflon can be realized by using the Sagnac Raman Interferometer.

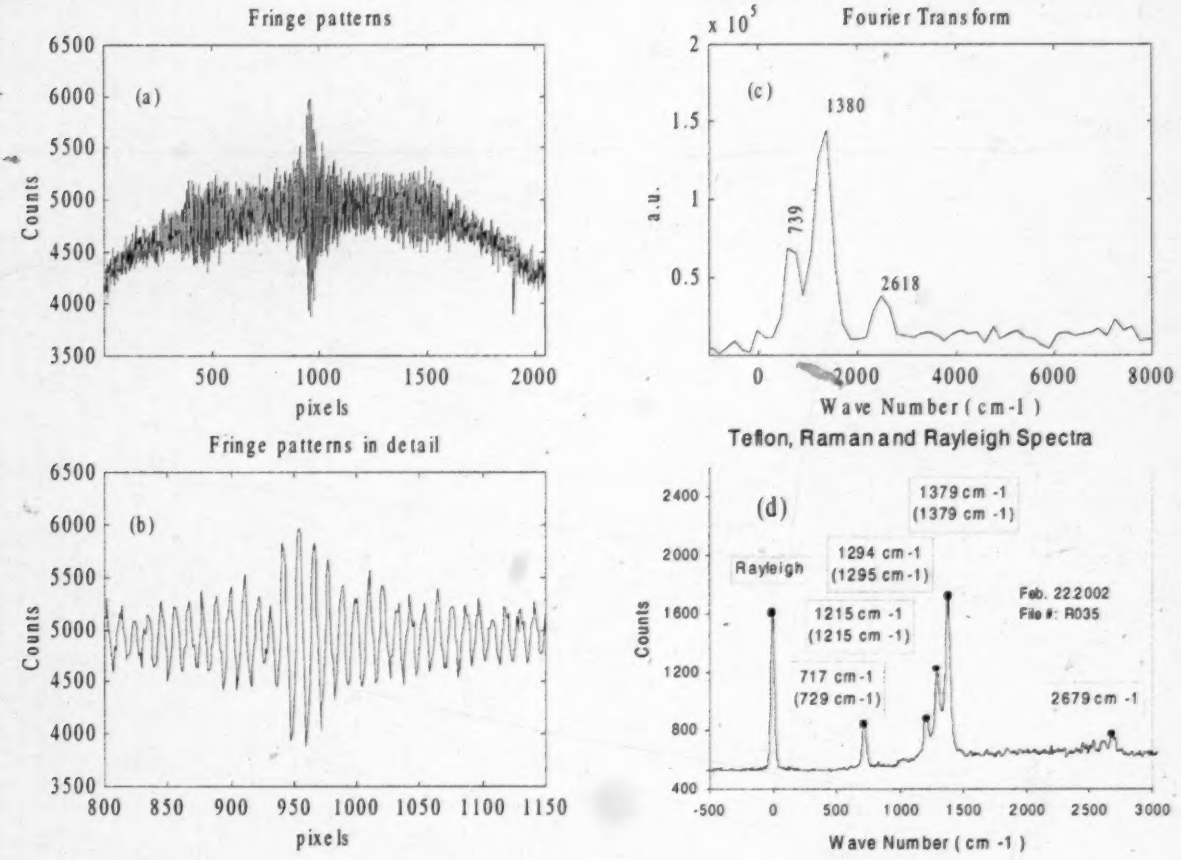

Fig. 3.4.6-2 The fringe patterns of Teflon & its FT Raman spectrum measured with a Sagnac interferometer (single shot) and compared to its conventional Raman spectrum: (a) full fringe pattern, (b) detailed fringe pattern, (c) Fourier Transform spectrum and (d) reference Raman spectrum

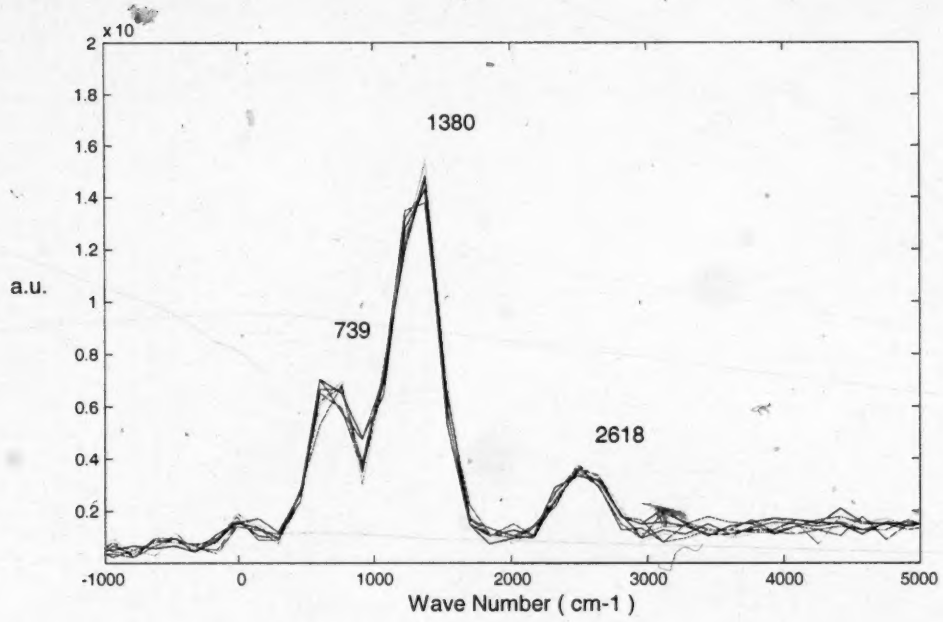

Fig. 3.4.6-3 8 overlaid single shot spectra of Teflon to demonstrate reproducibility

The reproducibility of the single shot spectra of Teflon was investigated by comparing 8 single shot spectra as shown in Fig 3.4.6-3. From the eight spectra the obtained spectral peaks had measured intensities and standard deviations of 68525±1691, 146250 ± 5676 and 35650 ± 1537 for the peaks obtain at 739 cm^{-1}, 1380, cm^{-1} and 2618 cm^{-1}. Thus it is seen that very good reproducibility is obtained for these single shot spectra.

Section 3.5 Theoretical calculation of FT Raman spectrum of Nitrogen

In order to estimate the overall efficiency of the FT UV Raman spectroscopy based on a Sagnac interferometer, a theoretical calculation was carried out by using Equation (2.3-1) which is copied here for convenience.

$$E_{Raman\ of\ N_2} = T \times (\frac{N}{V})_{N_2} \times (\frac{d\sigma}{d\Omega})_{N_2} \times L_{N_2} \times E_{Laser} \times \frac{h\nu_{Raman}}{h\nu_{Pump}} \times \Omega \qquad (3.5\text{-}1)$$

where T is the transmittance of the optical components between the sample and the UV CCD camera which consists of the UV high pass filter, the collecting lens, beam splitter, two mirrors and FT lens. Because the transmittances for reflecting and transmitting are different through the beam splitter, mirror, mirror and beam splitter, the average should be taken into consideration.

$$T_{R,Sagnac} = T_{R,Beam\ splitter} \times T_{Mirror} \times T_{Mirror} \times T_{R,Beam\ splitter} \qquad (3.5\text{-}2)$$

$$= 26.5\% \times 98\% \times 98\% \times 26.5\% = 6.7\%$$

$$T_{T,Sagnac} = T_{T,Beam\ splitter} \times T_{Mirror} \times T_{Mirror} \times T_{T,Beam\ splitter} \qquad (3.5\text{-}3)$$

$$= 37.5\% \times 98\% \times 98\% \times 37.5\% = 13.5\%$$

$$T_{Avg,\ Sagnac} = \frac{(T_{R,Sagnac} + T_{T,Sagnac})}{2} = \frac{6.7\% + 13.5\%}{2} = 10.1\% \qquad (3.5\text{-}4)$$

Thus, the overall transmittance is given by

$$T = T_{UV\ High\ pass\ filter} \times T_{Lens} \times T_{Avg,\ Sagnac} \times T_{FT\ Lens} \qquad (3.5\text{-}5)$$

$$= 75\% \times 90\% \times 10.1\% \times 90\% = 6.2\%$$

As with Equation (2.3-6) and (2.3-7)

$$(\frac{N}{V})_{N_2} = 78\% \times (\frac{N}{V})_{Air} = 1.75 \times 10^{19}\ molecular.cm^{-3} \qquad (3.5\text{-}6)$$

$$(\frac{d\sigma}{d\Omega})_{N_2} = 7.73 \times 10^{-30}\ \frac{cm^2}{Sr} \qquad (3.5\text{-}7)$$

L_{N_2} is the observed interaction length of Raman scattering which is assumed to be

$$L_{N_2} = 0.1cm \qquad (3.5\text{-}8)$$

E_{Laser} is the total integrated laser energy at 20Hz, 2.1 mJ and 800 seconds exposure time

$$E_{Laser} = 20 \times 2.1 \times 800\ mJ = 33.6\ J \qquad (3.5\text{-}9)$$

Ω is the solid angle of the collecting lens with 75 mm focal length and diameter 50 mm. The scattered light is focused by the FT lens with 300 mm focal length and a diameter 50 mm. When the refractive index as a function of wavelength is taken into account, the collecting and the FT lenses have focal lengths of 70 mm and 280 mm respectively at the N_2 Raman scattering 283.6 nm. Fig 3.5-1 shows how the scattered light with a starting solid angle Ω_2 goes through the optical components of Sagnac interferometer and projects

on a single pixel with area $A_{\text{one pixel}}$ on the UV CCD camera. A_2 and A_1 are the areas on the surfaces of collecting and the FT lenses projected by the beam with a solid angle Ω_2.

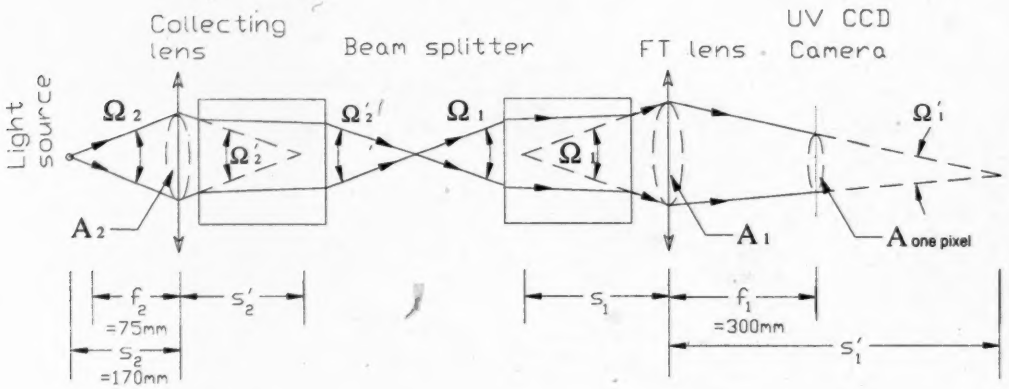

Fig 3.5-1 Schematic diagram of the ray cone for the solid angle that projects to a single pixel on the UV CCD camera

One can get the following relationship from Fig 3.5-1

$$\Omega_1' = \frac{A_{one\ pixel}}{(s_1' - f_1)^2} = \frac{A_1}{(s_1')^2} \tag{3.5-10}$$

$$\Omega_1 = \frac{A_1}{(s_1)^2} = \frac{A_2}{(s_2')^2} = \Omega_2' \tag{3.5-11}$$

$$\Omega_2 = \frac{A_2}{(s_2)^2} \tag{3.5-12}$$

The above Equations (3.5-10), (3.5-11) and (3.5-12) give

$$\Omega_2 = \left(\frac{s_1 s_2}{s_1 s_2 \times (s_1 - f_1)} \right)^2 \times A_{one\ pixel} \qquad (3.5\text{-}13)$$

Eliminate s by using $\frac{1}{s} + \frac{1}{s} = \frac{1}{f}$, which then gives the collection solid angle for one pixel as

$$\Omega = \Omega_2 = \left(\frac{f_2}{f_1 (s_2 - f_2)} \right)^2 \times A_{one\ pixel} \qquad (3.5\text{-}14)$$

$$= \left(\frac{70mm}{280mm \times (170mm - 70mm)} \right)^2 \times (13.5\mu m)^2$$
$$= 4.6 \times 10^{-7}\ Steradian$$

Thus, the energy of Raman scattering of N_2 into a single pixel is

$$E_{Raman\ of\ N_2} = T \times (\frac{N}{V})_{N_2} \times (\frac{d\sigma}{d\Omega})_{N_2} \times L_{N_2} \times E_{Laser} \times \frac{h\nu_{Raamn}}{h\nu_{Pump}} \times \Omega \qquad (3.5\text{-}15)$$

$$= 6.2\% \times 1.75 \times 10^{19} \times 7.73 \times 10^{-30} \times 0.1 \times 33.6 \times \frac{266}{283.6} \times 4.6 \times 10^{-7}$$
$$= 1.2 \times 10^{-17}\ J$$

The energy of one photon of N_2 Raman scattering is

$$E_{onephoton} = \frac{nh\nu}{\lambda} = \frac{1 \times 6.626 \times 10^{-34} \times 3 \times 10^8}{283.6} = 7.01 \times 10^{-19} J \qquad (3.5\text{-}16)$$

The experimentally measured raw FT UV Raman spectrum for air is shown in Figure 3.4.5-1. In this case, the Andor specification gives 0.7 photoelectrons per count and quantum efficiency 65% of UV CCD camera. Thus, the theoretically calculated counts of FT UV Raman signal expected for N_2 in each pixel is

$$Counts_{FT\ UV\ Raman\ of\ N_2} = \frac{E_{Raman\ of\ N_2}}{E_{one\ photon\ Raman}} \times \frac{1}{photoele.\ per\ cout} \times Q_{efficiency} \quad (3.5\text{-}17)$$

$$= \frac{2.9\times10^{-17}}{7.0\times10^{-19}} \times \frac{1}{0.7} \times 65\% = 16\ Counts$$

The reading from the experimental result in Figure 3.4.5-1 is 3000 counts in 512 pixels Full Vertical Binning mode which gives 5.9 counts on a single pixel. So, the difference between the theoretical calculation and the experimental result is approximate 175%. This is consistent with the calibration measurements which indicated that the quantum efficiency appears to be 2.13 times lower than the manufacturer's specification in the UV spectral range. In addition Raman light from Oxygen would add approximately an additional 55% to the signal as seen from Fig 2.3.1 which could increase the discrepancy further.

The total calculated Raman energy onto the CCD camera collected by the Sagnac interferometer is 12 pJ in 16000 shots versus the total energy collected by the conventional spectrometer of 0.127 pj in 1000 shots. Thus per shot the Sagnac interferometer collects approximately 6 times as much light as the conventional interferometer. It would be expected that the resultant signal to noise would be better in the FT Sagnac spectrum, but this not the case for the observed spectra. It is expected that this is due to aberrations in the imaging optics reducing fringe visibility and perhaps vibration in the optical components leading to shifting of fringes shot to shot. Further work will be required to identify all the reasons for this discrepancy.

Section 3.6 Comparison to previous published results

Several papers on Fourier Transform spectroscopy based on a Sagnac interferometer [2, 5, 7-11, 17-21] and in particular Raman application [5, 8], have been published.

In the present study, the understanding of Fourier Transform Sagnac interferometry has been advanced in several areas. The physical principles of FT spectroscopy based on Sagnac interferometer have been clearly presented. The curvature of the interference fringe pattern was identified as an additional factor which requires correction. The condition to minimize this curvature, choosing the focal length of the FT lens much greater than the width of UV CCD camera, was indicated. A geometric optical analysis was carried out to indicate that the interference fringe pattern is located at the focus plane of the FT lens which is also the plane of maximum overlap. The optimum position of UV CCD camera determined experimentally for a Hg spectral lamp confirmed this optimum UV CCD camera position. Also, the fringe spacing formula, $\Delta x = \frac{\lambda f}{2a}$, and the resolution formula, $\Delta\sigma_{max} = \frac{2}{N\lambda_{min}}$, were derived. These formulae were confirmed experimentally by measuring the Hg spectra versus the position of the movable mirror.

It was discovered that the chromatic aberration of the FT lens affects the optimum position of UV CCD camera relative to the FT lens and also affects the wavelength calibration for any given position. A better accuracy wavelength calibration was

obtained by taking the chromatic aberration of FT lens into consideration. There has been very limited analysis of such aberration effects on the performance of Sagnac Interferometers in the past [11] with no discussion of wavelength correction techniques. The relationship of the fringe visibility to the fringe spacing was experimentally determined showing the reduction in fringe visibility for fine fringe spacing due to optical aberrations. The reduction in resolution due to optical aberrations has been noted in reference [11] but no experimental measurements of the effect were presented. Thus there is a trade off between improved S/N ratio with large fringe spacing and high fringe visibility versus improved resolution which requires fine fringe spacing. In the present study a complete analysis of optical throughput has been carried out of the Sagnac interferometer and compared to a standard dispersive spectrometer indicating the higher potential light gathering power of the Sagnac interferometer.

The FT Raman spectra that were demonstrated in this study are in the Ultra-Violet range, which are different than the previously reported results in the visible range [5, 8]. But, it is challenge to get the required quality UV components. The specification in terms of optical figure in fractions of a wavelength and balance between reflectivity and transmission of beamsplitter are significantly poorer for standard commercially available UV components.

In the present study, the resolution is not as good as previous results because a shorter wavelength exciting laser (266nm) was used in order to avoid fluorescence and increase the Raman scattering. The spectral resolution is inversely proportional to the

minimum or cutoff wavelength, assumed to be the same as the exciting laser wavelength. Thus for the same number of pixels on a CCD camera the frequency resolution will scale inversely with probe wavelength. This is seen when comparing the best spectral resolution obtained in the present study of 80 cm^{-1} as compared to the spectral resolution of 24 cm^{-1} reported in references [5, 8] for a probe wavelength of 830 nm.

Chapter IV

Other Applications of FT spectroscopy with a Sagnac Interferometer

Section 4.1 FT LIBS with the Sagnac Interferometer

Laser-Induced Breakdown Spectroscopy, or LIBS, is a technique in which a focused laser pulse is directed onto a sample. The energy from the laser pulse heats, vaporizes, atomizes, and ionizes the material on the surface of the sample resulting in a small hot plasma. The line emission from the atoms and ions in the plasma is then detected. Elements in the plasma are subsequently identified via their unique spectral signatures. This technique can be applied to the rapid analysis of metals alloy as one example.

Generally, the free spectral range, $\Delta\nu_{max} - \Delta\nu_{min}$, is limited by the spectrograph. The whole spectrum has to be retrieved with several data acquisitions over different wavelength ranges and combined together if the complete spectrum is desired. In order to overcome this disadvantage, the Sagnac Interferometer can be employed to give braoad spectral coverage. The illumination geometry is modified a little bit, simply by putting a focusing lens into laser beam and focusing it on the sample, to obtain FT LIBS with a single laser shot for the whole wavelength range.

A single shot FT LIBS of Aluminum (Al 6061) with the Sagnac Interferometer was carried out and the result is shown in Figure 4.1-1 where (a) is the fringe pattern of LIBS, (b) is the detailed fringe pattern, (c) is the Fourier Transform of LIBS and (d) is the LIBS spectrum measured with a conventional spectrograph in our lab. By comparing the LIB spectra using these two methods, it can be seen that the wavelength of these two spectra matches very well, for example: Al I 309.27 nm (310nm), Cu I 324.75nm (324 nm), Cr I 357.87nm (358nm), Mg I 383.45 nm (383nm) and Al I 396.15nm(397nm) with FT LIBS wavelengths in brackets. The features of the two LIBS spectra for the same sample are slightly different because different experimental conditions were employed, such as different laser energy and focal length lens. The cutoff in the Sagnac spectrum at 460 nm is due to the mirrors used in the interferometer.

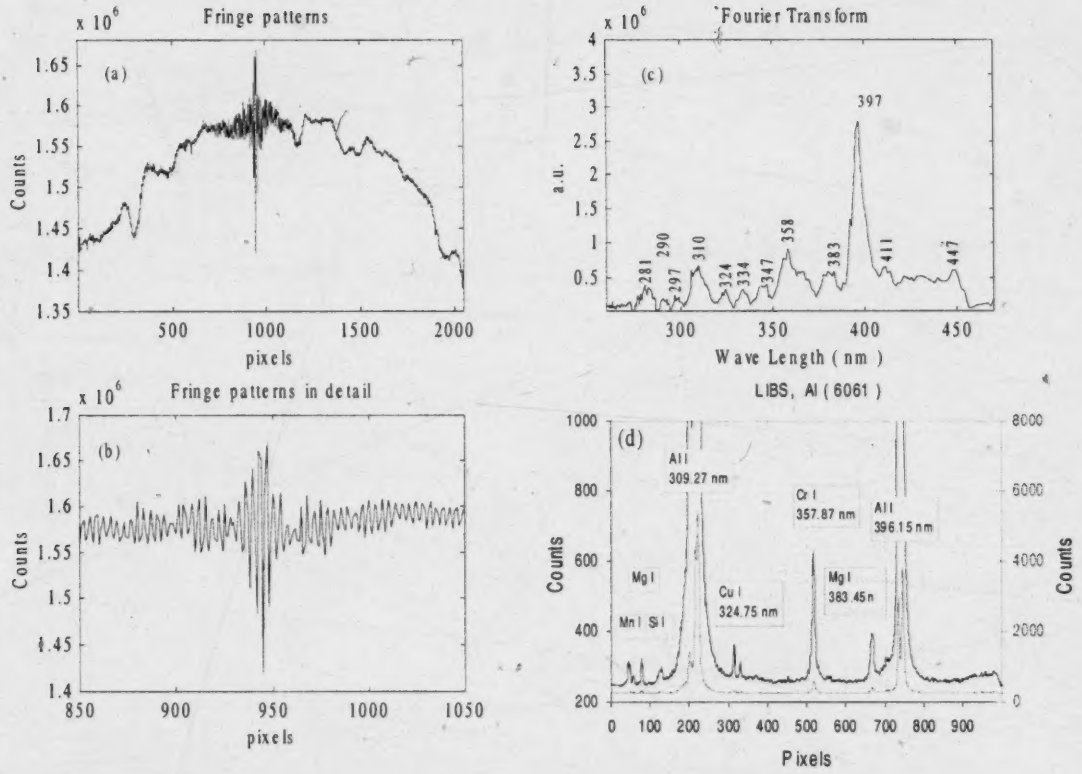

Fig. 4.1-1 The experimental FT LIBS of Aluminum 6061 alloy for 1 mJ, laser pulses focused with a 250 mm focal length lens (single shot)

Section 4.2 FT LIF with a Sagnac Interferometer

Laser-Induced Fluorescence, LIF, is a process whereby molecules/atoms of the samples are excited to higher electronic energy states via laser absorption and subsequently fluoresce. Each sample has its unique spectral profile and the intensity of this fluorescence is a function of the species concentration. LIF is a useful diagnosis technology for both qualitative and quantitative measurements.

Without modification, the same experimental setup for FT Raman Spectroscopy with a Sagnac Interferometer can also be used for LIF. The experimental procedures are the same as for Methanol with multiple shots. FT LIF with the Sagnac Interferometer has all the advantages that FT Raman Spectroscopy with the Sagnac Interferometer has, plus the fluorescence signal is generally much stronger than the Raman signal.

Two examples of FT LIF, from green paper and from a wood chip (black spruce), are shown in Figure 4.1-2 and Figure 4.1-3, respectively. Fluorescence of the green paper from 266nm to 700nm can be obtained. The cutoff in the Sagnac spectrum at 460 nm is due to the mirrors used in the interferometer. The lower resolution of the Sagnac interferometer is not a major limitation when measuring broad features of a fluorescence spectrum. No reference spectrum are available for comparison to these data.

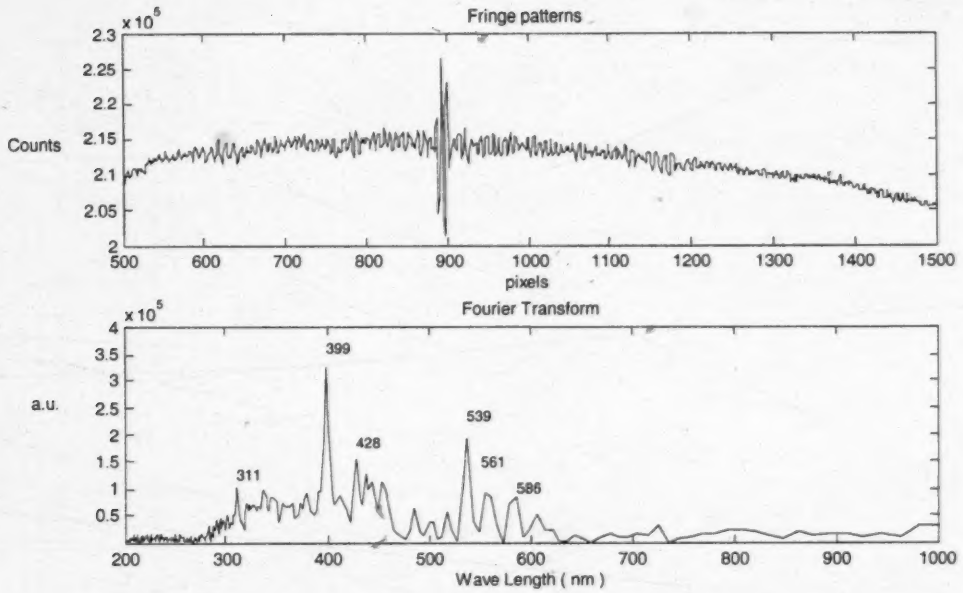

Fig. 4.1-2 The experimental LIF of green paper with laser energy 1mJ,

1000 shots and resolution 226 cm^{-1}

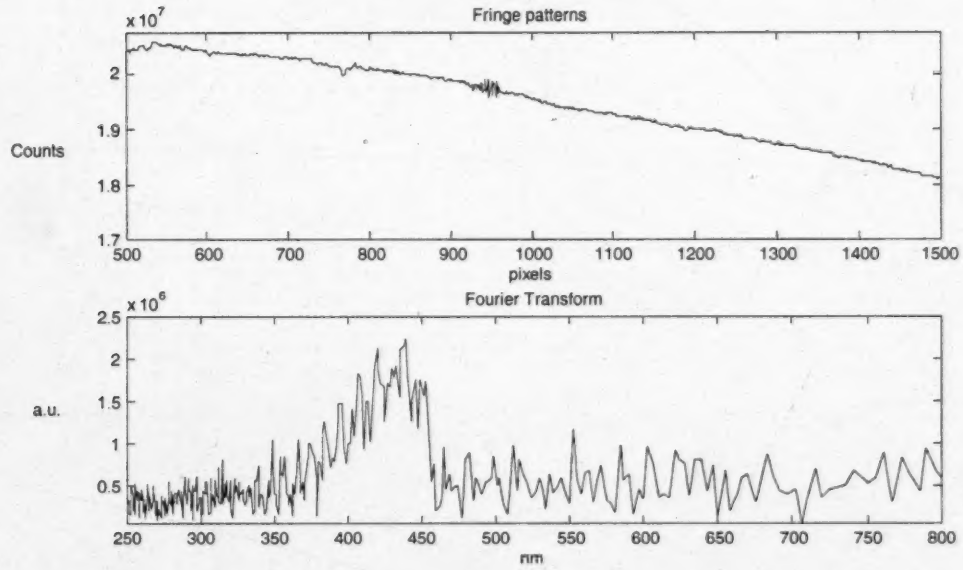

Fig. 4.1-3 The experimental LIF of black spruce with laser energy 1mJ,

1000 shots and resolution 113 cm^{-1}

Chapter V

Discussions and Conclusions

A Sagnac interferometer has been built and characterized for use at Ultraviolet wavelengths. The characteristics of the Sagnac interferometer have been studied theoretically and experimentally. The fringe spacing of the Sagnac interferometer was derived from a geometric optics model and confirmed with the experimental results. The maximum theoretical resolution is determined not only by the number of pixels in the CCD detector array but also by the minimum wavelength, which for Raman spectroscopy is the wavelength of the exciting laser. However the actual resolution achievable is limited by the aberrations due to optical components which cause a significant reduction of fringe visibility when fine fringes are employed to obtain high resolution.

In the Sagnac interferometer, the CCD camera is located at a position where the transmitted and reflected wave fronts cross at the focal plane of the lens and not the imaging plane of the source. The position of the movable mirror determines the spacing of the fringes which also determines the spectral resolution and the visibility of the fringes. As the visibility improves with increased fringe spacing while the resolution is inversely proportional to fringe spacing, a trade off between signal to noise ratio and resolution must be made in determining the desired position of the movable mirror.

A suitable focal length of the FT lens has to be chosen based on the curvature of fringes and the collecting angle of the input signals. In order to obtain a higher optical throughput and thus high S/N ratio, a shorter focal length of FT lens should be employed.

Meanwhile, a smaller curvature of fringes must be maintained by using a longer focal length of the FT lens, otherwise, the edge fringe patterns will be deformed leading to blurring when summing up the pixels in one column and the non uniform fringe spacing will distort the resultant FT spectra.

Fourier Transform Ultra-Violet Raman Spectroscopy using the Sagnac Interferometer has been successfully demonstrated and FT Raman spectra of selected samples have been measured. All these FT spectra are compared with their corresponding conventional spectra. Also, single shot FT UV Raman spectra have been demonstrated showing that time-resolved Raman spectroscopy covering the whole wavelength range is feasible.

Raman Spectroscopy with a conventional dispersive spectrometer was also carried out for comparison. Fluorescence and Rayleigh scattering was found to interfere with the Raman signal and filters must be used to eliminate Rayleigh scattering to avoid excessive scattered light in the single spectrometer system. The theoretical analysis of the strength of the N_2 Raman spectrum matches the experimental result reasonably well for the dispersive spectrometer but was significantly stronger than the measured Raman spectrum for the Sagnac interferometer.

Other than Raman spectroscopy, Laser Induced Breakdown Spectroscopy (LIBS) and Laser Induced Fluorescence (LIF) can also take advantage of Fourier Transform Spectroscopy. Experimental results are shown indicating that FT LIBS and FT LIF are feasible.

The present results show that a Sagnac interferometer is potentially useful for Raman spectroscopy in the Ultraviolet wavelength region. Critical issues such as aberrations introduced by the Fourier Transform lens both in reduction of fringe visibility and nonlinear spacing of fringes have been identified. With the present system single shot Raman spectra of limited resolution have been demonstrated for liquid and solid samples and it is expected that improved control of aberration can lead to improved signal to noise ratio and resolution in such single shot spectra.

A number of issues should be studied in more detail in the future in order to improve upon the results obtained in the present study. More detailed measurements should be made of the optical flux of the Raman signal at various points throughout the Sagnac interferometer to identify why the measured signal strength is less than predicted. A detailed ray trace analysis of the system should be carried out to study the expected blurring of fringes due to lens aberrations, and various improved lens designs studied in order to allow high fringe visibility at high spectral resolution. At the same time, the wavelength dependence of fringe spacing due to chromatic aberration should be calculated and compared in detail to the measured results. It also appears that the

multiple shot interferograms have lower fringe visibility than the single shot results indicating potential blurring of fringes due to vibration of optical components from shot to shot. Overall, it is expected that these further studies will help to identify the critical variables which need to be improved in order to obtain the expected higher optical efficiency and Nyquist limited resolution of a Sagnac interferometer as compared to a standard dispersive spectrometer.

References

1. Ivanov EV "Static Fourier transform spectroscopy with enhanced resolving power"
J of Opt. A-Pure&Applied Opt. 2(6):519-528 NOV 2000

2. Hirschberg JG "Pentaferomter_a solid Sagnac interferometer"
Applied Optics, 38: (1) 136-138 JUN 1 1999

3. Genest J "Throughput of tilted interferometers"
Applied Optics 37: (21) 4819-4822 JUL 20 1998

4. Korenberg MJ "Raman Spectral Estimation Via Fast Orthogonal Search"
Analyst, 122: (9) 879-882 Sep 1997

5. Zhao Jun "Multichannel FT-Raman spectroscopy"
Applied Spectroscopy 51, pp.1687 (1997)

6. Courtial J "Design of a static Fourier-transform spectrometer..."
Applied Optics, 35: (34) 6698-6702 DEC 1 1996

7. Dierking MP "Solid-block stationary Fourier-transform spectrometer "
Applied Optics 35: (1) 84-89 Jan 1 1996

8. Zhao Jun "Multichannel Fourier Transform Raman Spectroscopy",
Applied Spectroscopy, 50, 1209 (1996).

9. Rafert JB "Monolithic Fourier-transform imaging spectrometer"
Applied Optics 34: (31) 7228-7230 NOV 1 1995

10. Sellar RG " Fourier-transform imaging spectrometer with a single toroidal optic"
Applied Optics, 34: (16) 2931-2933 JUN 1 1995

11. Sellar Rg "Effects Of Aberrations On Spatially Modulated FT Spectrometers" Optical Engineering, 33: (9) 3087-3092 Sep 1994

12. Junttila Ml "Stationary Fourier Spectrometer For Optical Transmittance Measurements", Measurement Sci. & Tech. 4: (7) 740-745 Jul 1993

13. Takahashi S "Multichannel Fourier-Transform Spectroscopy Using 2-D Detection Of The Interferogram and Its Application To Raman-Spectroscopy" Applied Spectroscopy, 47: (7) 863-868 Jul 1993

14. Junftila ML "Stationary Fourier-transform spectrometer" Applied Optics 31: (21) 4106-4112 JUL 20 1992

15. Hashimoto M "S/N Ratio of Multi-channel Fourier-transform Spectroscopy " J. of Spectroscopic Society of Japan, (41) 317, 1992

16. Junttila Ml "Performance Limits Of Stationary Fourier Spectrometers J. of The Opt. Soc.of Ame. A, 8:(9) 1457-1462,1991

17. Sweedler JV "Crossed interferometric dispersive spectroscopy" Applied Spectroscopy. 44, pp.14 (1990)

18. Sweedler JV "Spatially Encoded Fourier-Transform Spectroscopy In The UV To Near-IR". Applied Spectroscopy 43, pp.1378 (1989).

19.Barnes TH "Photodiode array Fourier transform spectrometer with improved dynamic range". Applied Optics 22, 3702 (1985)

20.Okamoto T "Optical Method For Resolution Enhancement In Photodiode Array FT Spectroscopy". Applied Optics 24, pp.4221 (1985)

21.Okamoto T "Fourier transform spectrometer with a self-scanning photodiode array" Applied Optics 23, 269 (1984)

22. Chadha S. "UV-Excited Raman and Resonance Raman Spectra of Synthetic Polymers" Applied Spectroscopy 23, 1176 (1992)

23. Chakrabarti S. "Self-compensating, all-reflection interferometer" Applied Optics, p2596, 1 May 1994

24. R. Fedosejevs "Laser Sensor Technology", EE 602 B8 Lecture Notes, 2000. The Department of Electrical and Computer Engineering, U of Alberta

25. DMS Butterworths "UV Atlas of Organic Compounds", Library of Congress Catalog Card Number #66-21543, D7/3

26. Tolansky S. "An Introduction to Interferometry", U of A library number,, QC 411 T64 I c.2

27. John Chamberlain "The principles of intrferometric Spectroscopy"U of A library number, QC 454 F7 C44

28. Francon M "Optical Intrferometry", U of A library number, QC 411 F82 C.3

29. Ming Wu "Stan-off Detection of Chemicals by UV Raman Spectroscopy", Applied Spectroscopy, 800, Volume 54, Number 6, 2000

30. Craig J. Sansonetti "Wavelengths of spectral lines in mercury pencil lamps", 74, Applied Optics, Volume 35, No.1 1 January 1996

31. Joseph Reader "Irradiance of spectral lines in mercury pencil lamps", 78, Applied Optics, Volume 35, No.1 1 January 1996

31. Malitson IH "Interspecimen comparison of the refractive index of fused silica," J. Opt. Soc. Am. 55, 12054209 1965

32. Fundamentals of Optics, F. Jenskins, H. White, McGRAWHILL P. LTD, 1955.

33. Data base of Raman spectroscopy, Website: http://www.aist.go.jp/ RIODB /SDBS/ sdbs/owa/sdbs_sea.cre_frame_sea

34. Optical filters, Barr Associates Inc. Website: http://www.barrassociates.com/

35. Quartz cell, NSG Precision Cells, Inc. Website: http://www.nsgpci.com

36. UV CCD Camera, Andor Technology Limited, Website: http://www.andor-tech.com

37. Alan V. Oppenheim "Discrete-Time Signal Processing". Second Edition. p542

Appendix A

Pictures of experimental setup

Fig. A-1 Experimental setup (Top left view)

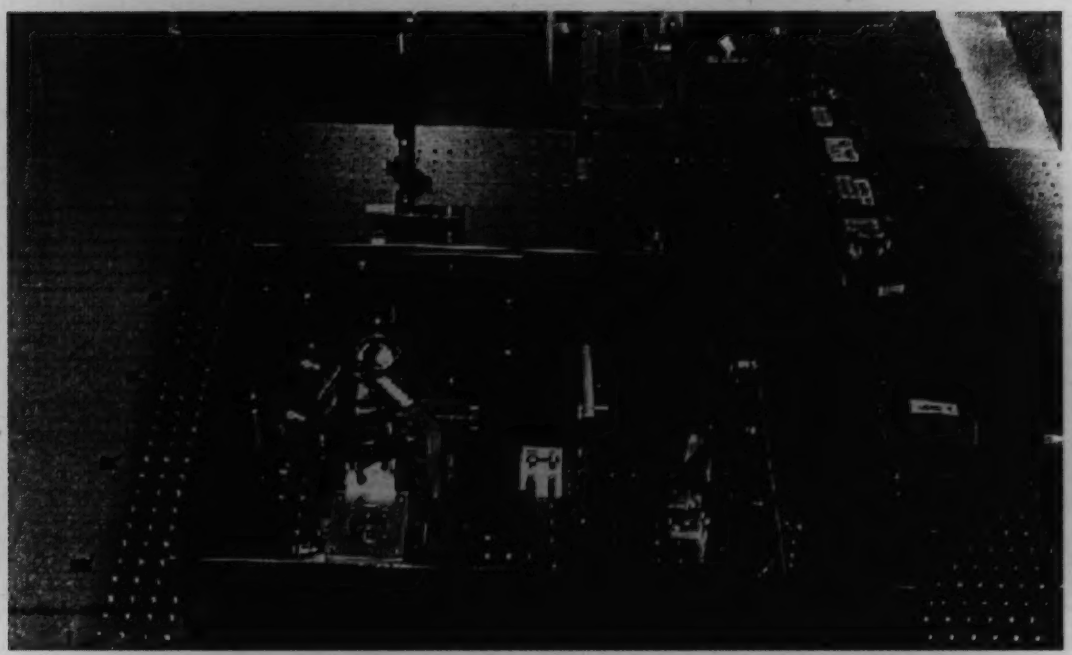

Fig. A-2 Experimental setup (Top right view)

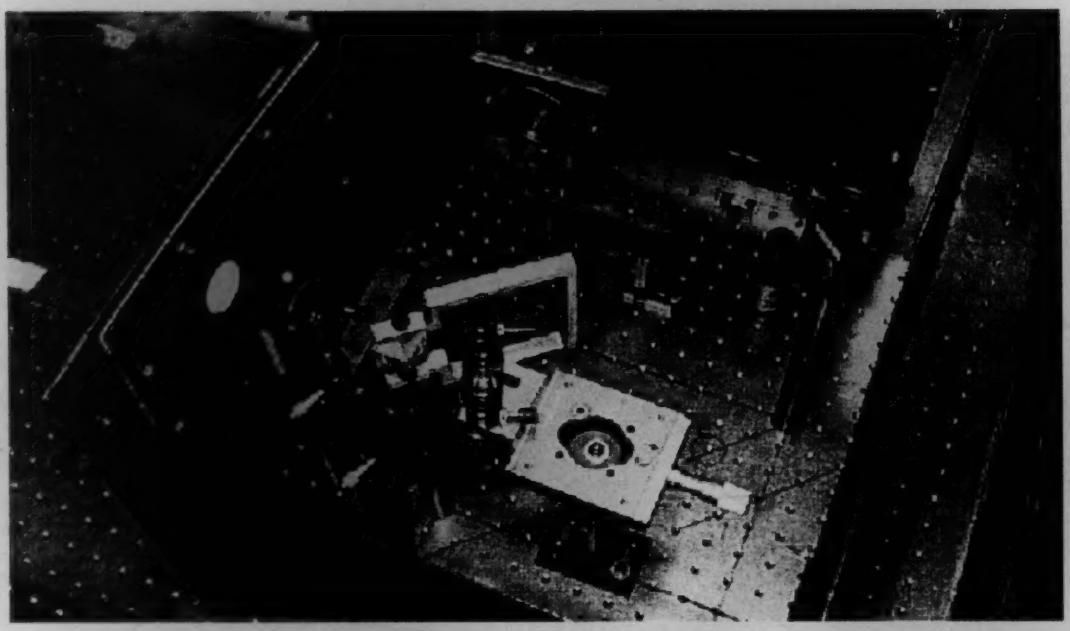

Fig. A-3 Experimental setup (Internal top right view)

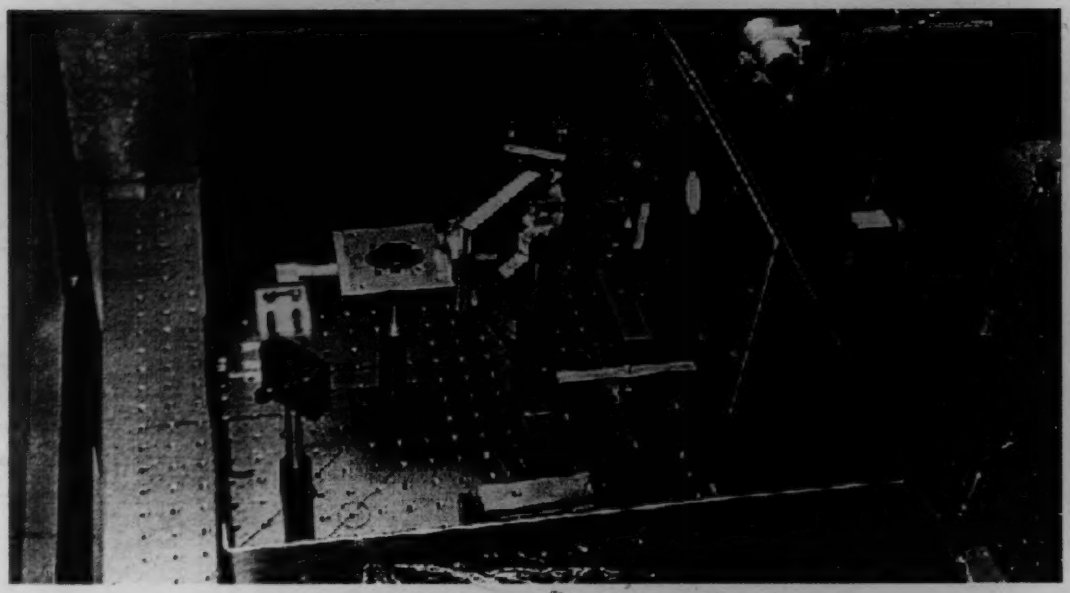

Fig. A-4 Experimental setup (Internal top back view)

Fig. A-5 Sangac Interferometer (top right view)

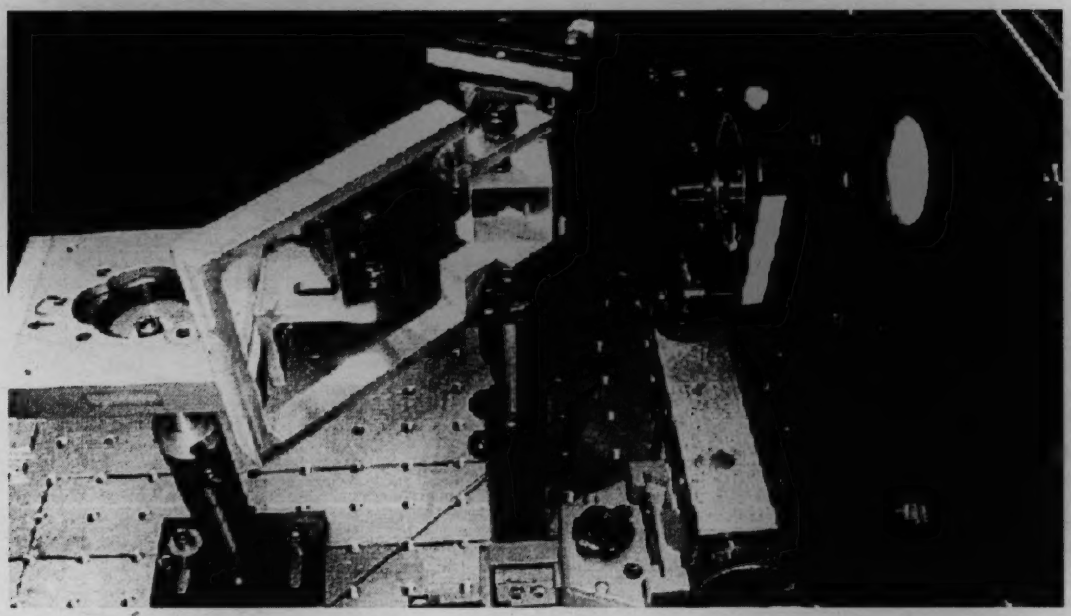

Fig. A-6 Sangac Interferometer (top back view)

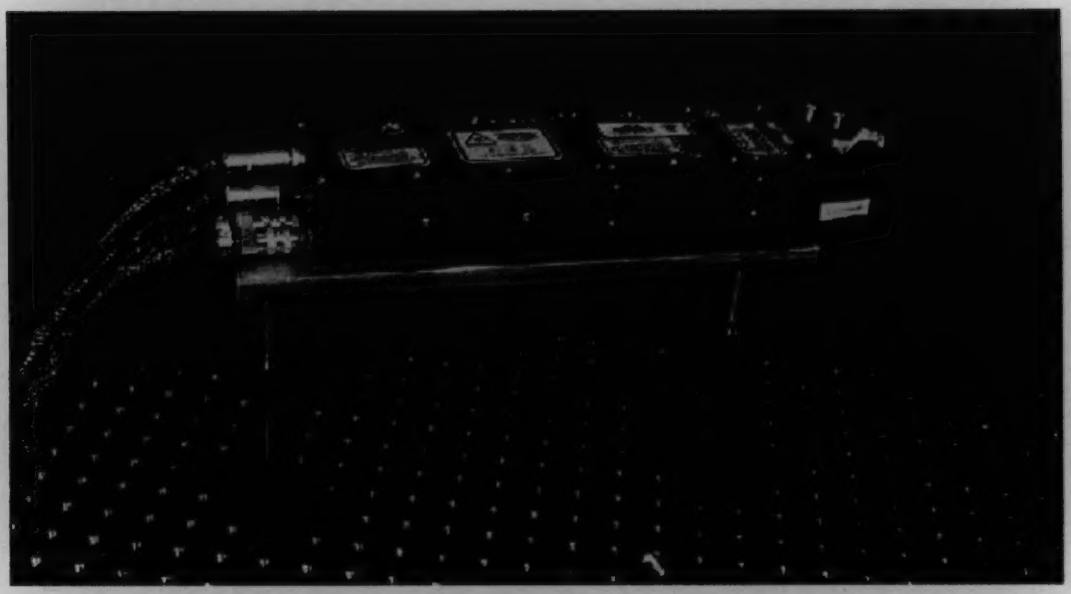

Fig. A-7 4th harmonic Nd:YAG laser (Raman exciting laser)

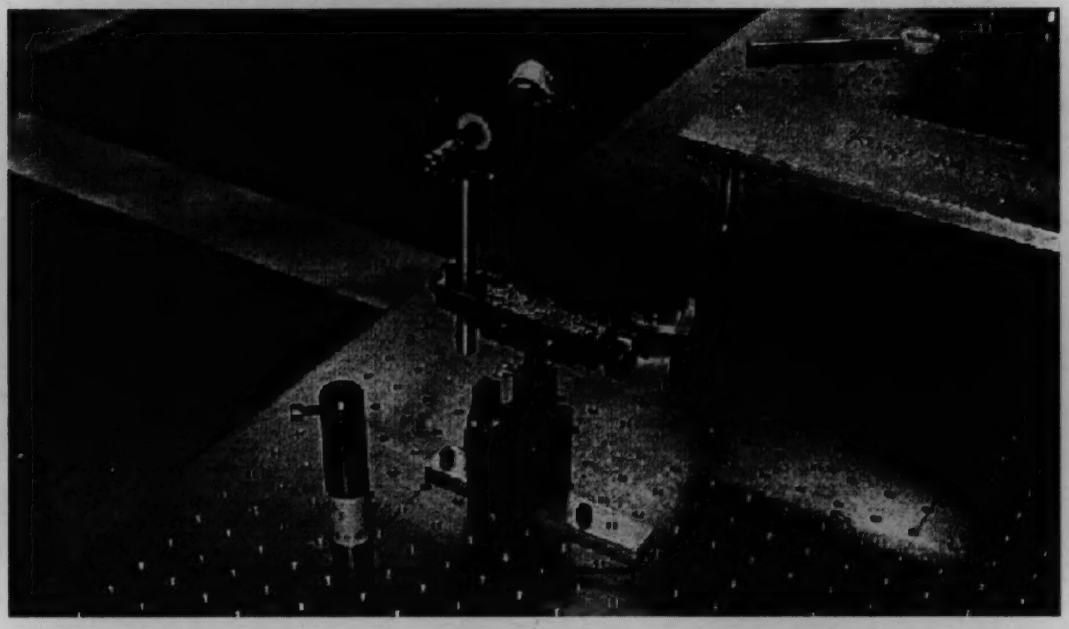

Fig. A-8 2nd harmonic Nd:YAG laser (for alignment)

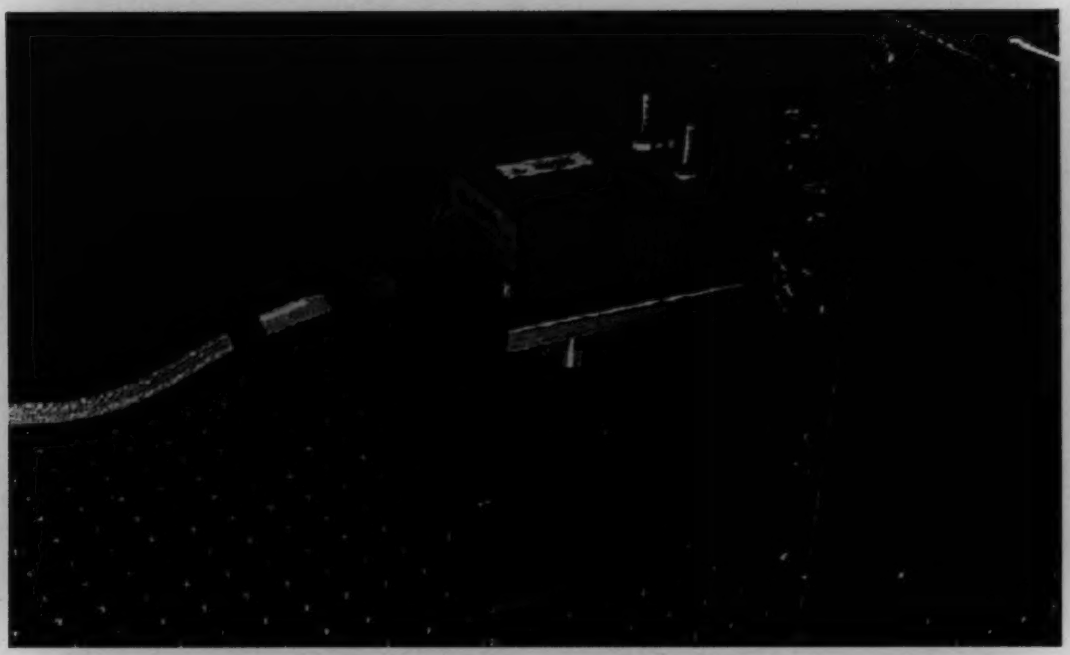

Fig. A-9 UV CCD camera

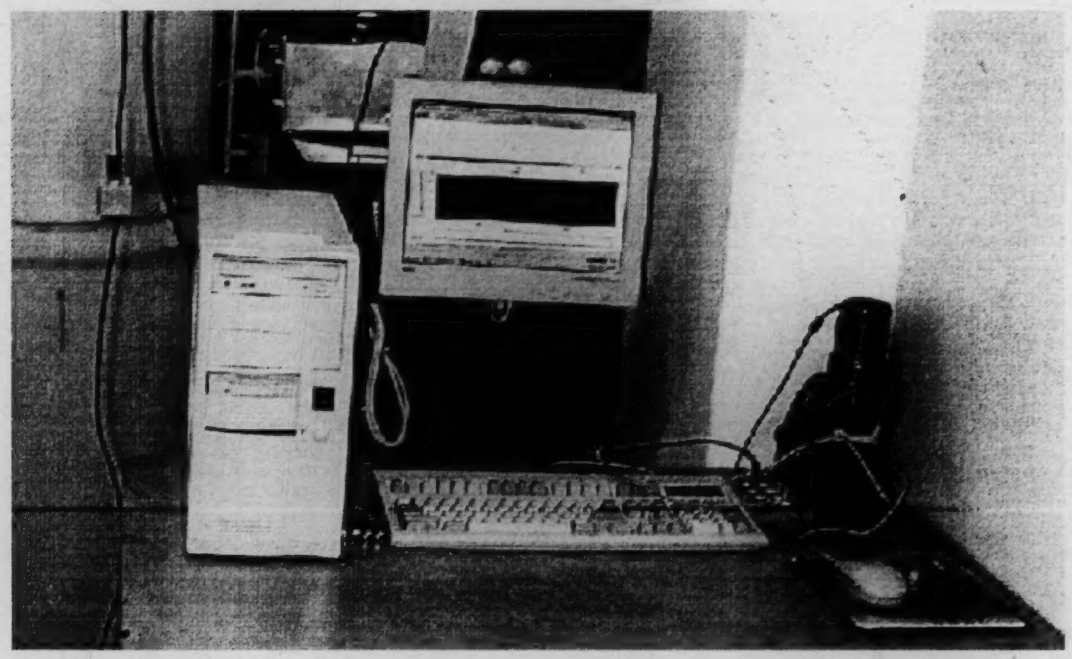

Fig. A-10 Computer

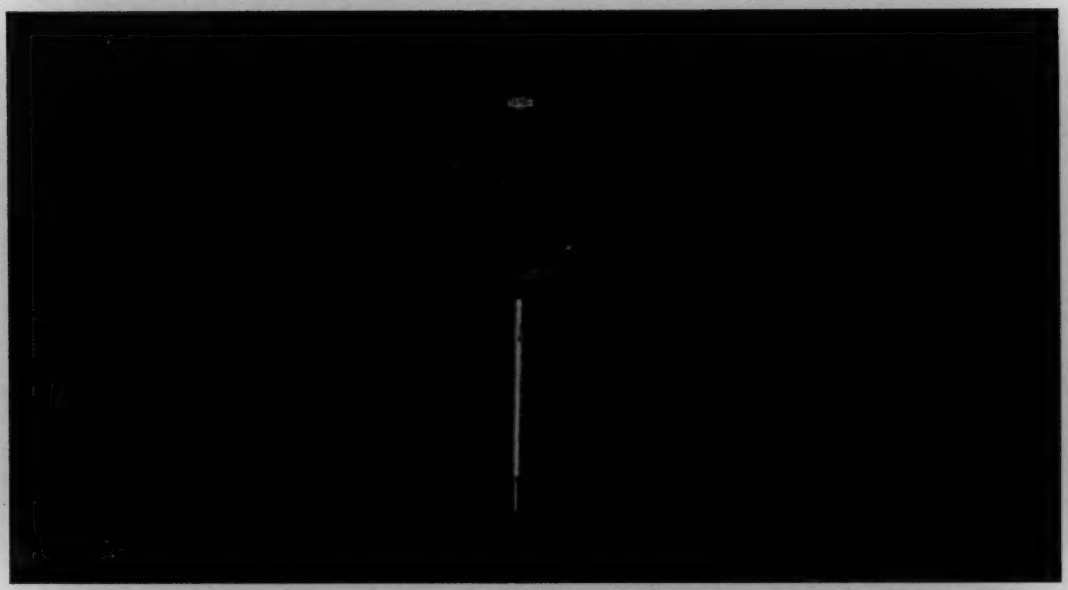

Fig. A-11 UV Liquid High pass filter

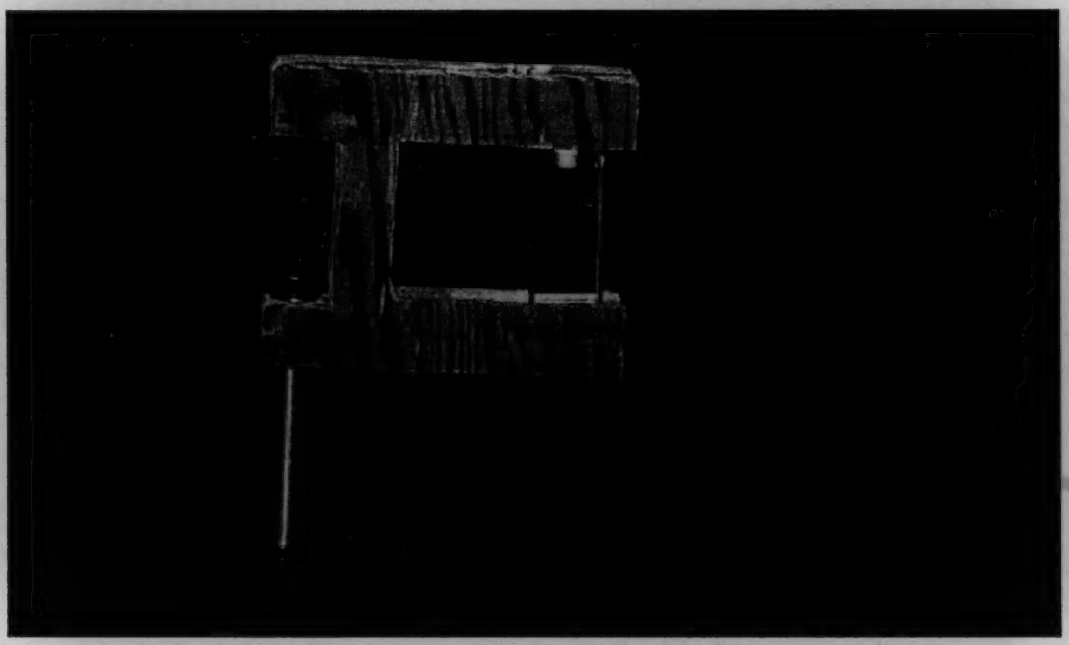

Fig. A-12 Liquid sample holder

Appendix B

Alignment Procedure

for the Sagnac Interferometer

While the alignment of Sagnac interferometer is not difficult, it is still necessary to take care in order to obtain the desired performance. The procedure for setting up the FT Raman spectroscopy with a Sagnac interferometer that was followed is as following.

(01) **Set up the beam height and alignment laser**

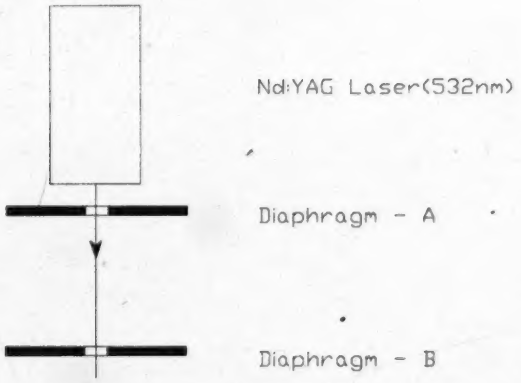

Fig. B-1 The alignment of the proper height for all diaphragms

A pencil type of 532 nm Nd:YAG laser is fixed on a 2-D travel translation stage which sits on an optical table. The diaphragm is fixed on a post on which a collar is attached. The heights of all the post holders of the diaphragms should be the same. Every diaphragm is put on the post holder at a position A, and its height is fixed by its collar so that the laser beam goes through it. In this way, all the diaphragms in system will have the same height. Two diaphragms are then positioned at A and B along the same column of holes on the optical table. The laser beam is adjusted until it goes through both of them. Then, a laser beam parallel to both the surface of the optical table and one set of column holes is obtained. All the optical components are then aligned using this laser beam,

(02) **Alignment of the UV beam splitter**

Fix the diaphragms C and D along a row of the optical table and then adjust the alignment mirror until the laser beam goes through both of diaphragms C and D. Because all the heights of diaphragms are already calibrated, the laser beam is parallel to both the row of mounting holes and the surface of the optical table.

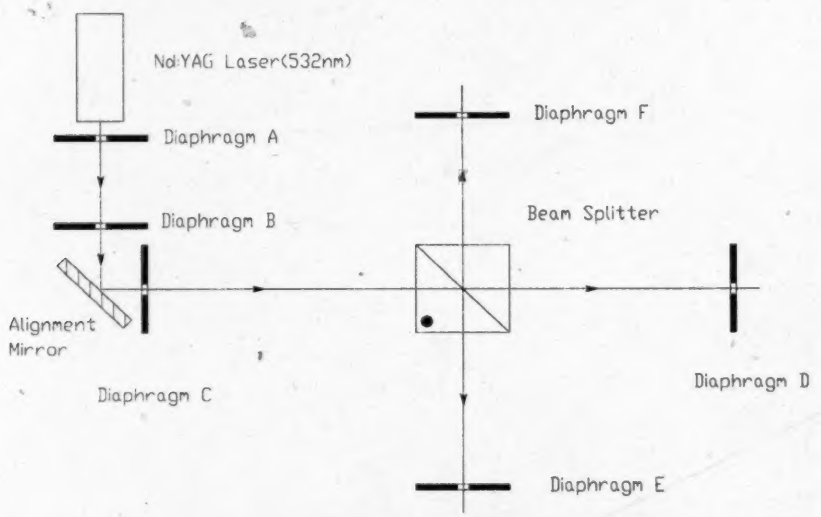

Fig. B-2 The alignment of the beam splitter

Now, put the beam splitter in place and adjust it until the laser beam goes through the diaphragms E and F which sit along the same column of the optical table. The laser beam must also go through the center of every surface of beam splitter. Because the surface reflection from the entrance face of the beam splitter, part of the laser beam will go back along its incoming path. By looking at this spot on the diaphragm C and adjusting the beam splitter until the spot goes through the diaphragm C, the surfaces of beam splitter will be aligned vertical to the surface of optical table and aligned with the directions of the mounting holes.

(03) Alignment of the 45° mirror

Both the movable mirror and static mirror in the Sagnac interferometer have a 22.5° angle with respect to their incident beams as shown in Figure B-3. A mirror, named 45° mirror, is used to carry out this alignment as shown in Figure B-4.

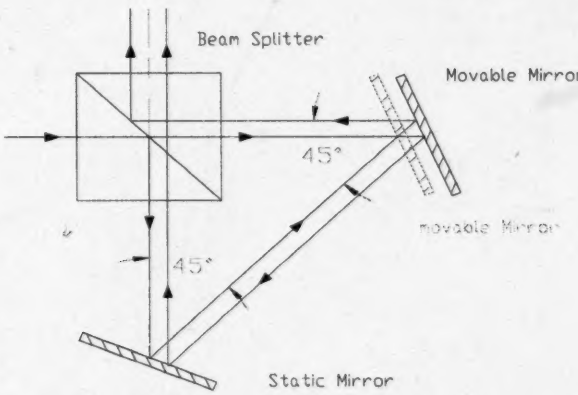

Fig. B-3 Schematic diagram of a Sagnac interferometer

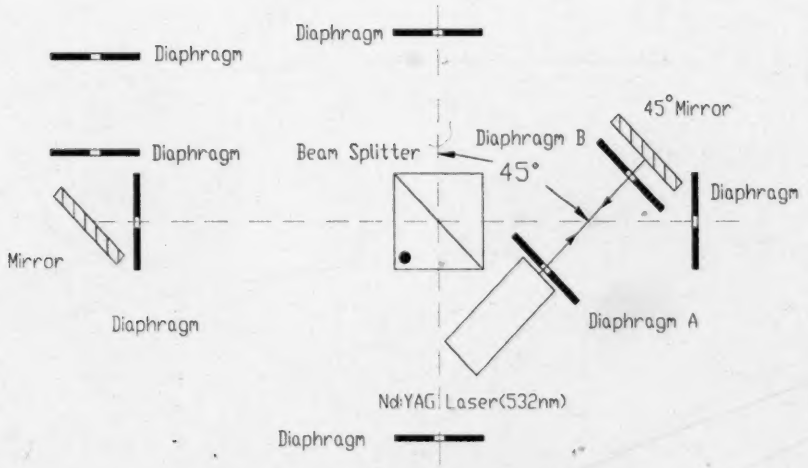

Fig. B-4 Alignment of a 45° mirror

The optical table has mounting holes separated by one inch both in the column and row directions. So, its diagonal is at a 45° angle and we take advantage of this to set up the 45° mirror. As shown in Figure B-4, a mirror, two diaphragms A and B and the 532 nm Nd:YAG laser are arranged along the diagonal of the optical table. By checking the feedback from the 45° mirror on the diaphragm A, a 45° angle to both the rows and the columns can be obtained. The 45° mirror remains at this position for the remainder of the alignment. Diaphragms A and B are removed and the 532 nm Nd:YAG laser is moved back to its original position.

(04) **The alignment of the static mirror**

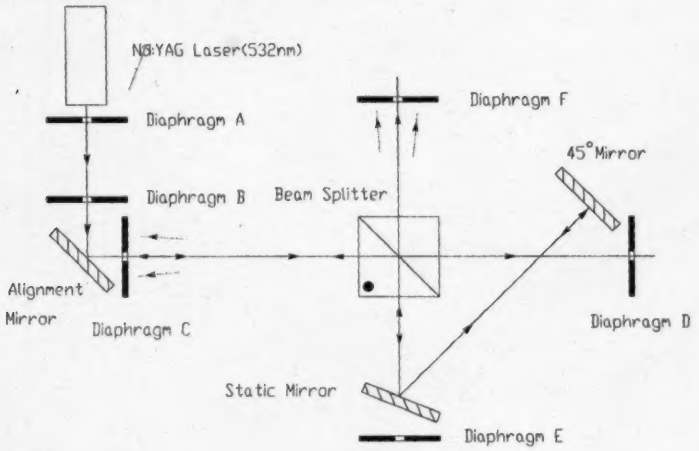

Fig. B-5 Alignment of the static mirror

As shown in Figure B-5, the laser beam is reflected by the beam splitter, reflected by the static mirror, reflected by the 45° mirror, reflected by the static mirror, reflected by the beam splitter and back to diaphragm C. The reflected spot of the laser on diaphragm C is used to adjust the static mirror. The laser beam should also hit the center of the static mirror.

(05) **The alignment of the movable mirror**

As shown in Figure B-6, the movable mirror is put at a position from where it has an equal distance to the surface of beam splitter as the distance between the static mirror and the surface of beam splitter. Adjust the movable mirror, so the laser beam hits the center of its surface. The beam splitter divides the laser beam into two parts. One is reflected by the beam splitter, reflected by the static mirror, reflected by the movable mirror, then, part of it reflected to the diaphragm F and part of it transmits to the diaphragm C. The other one is transmitted by the beam splitter, reflected by the movable mirror, reflected by static mirror, then, part of it is reflected to the diaphragm C and part of it is transmitted to the diaphragm F. By checking the spots on the diaphragms C and F, the movable mirror can be adjusted to a position at an angle of 22.5° to the incident beam.

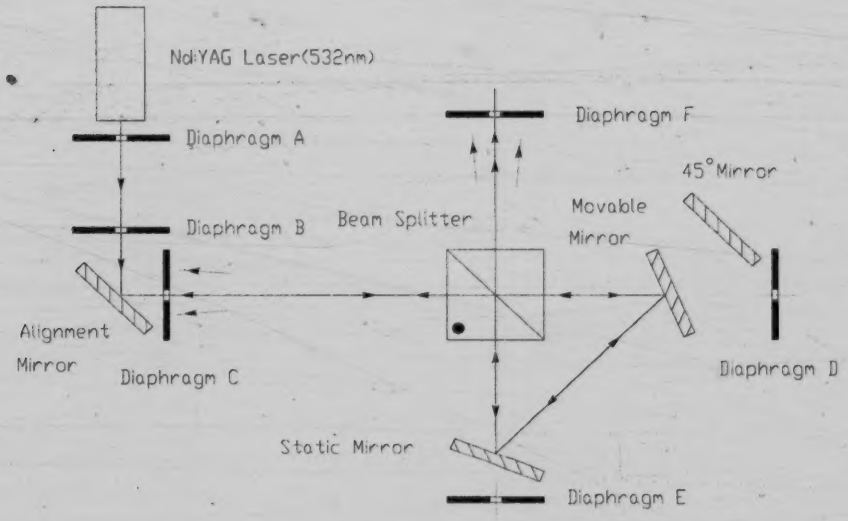

Fig. B-6 Alignment of the movable mirror

(06) **The alignment of FT lens and the collecting lens**

The alignment of the FT lens is illustrated in Figure B-7. Firstly, adjust the FT lens to make sure the laser beam goes through the center of the FT lens and diaphragm F. Secondly, adjust the laser spot reflected by the surfaces of lens so that the spot goes through the diaphragm C. The spots both on the diaphragms C and F have to be monitored. So, the laser beam goes through the center of lens and its flat side surface is perpendicular the laser beam.

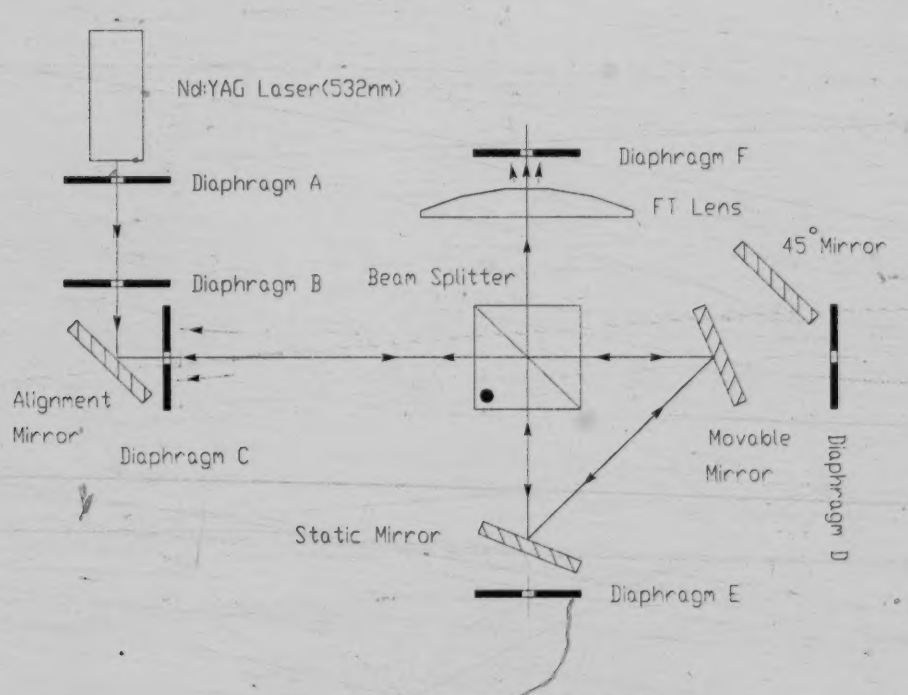

Fig. B-7 Alignment of the FT lens

The alignment of the collecting lens is carried out with a similar procedure as FT lens as shown in Fig. B-8.

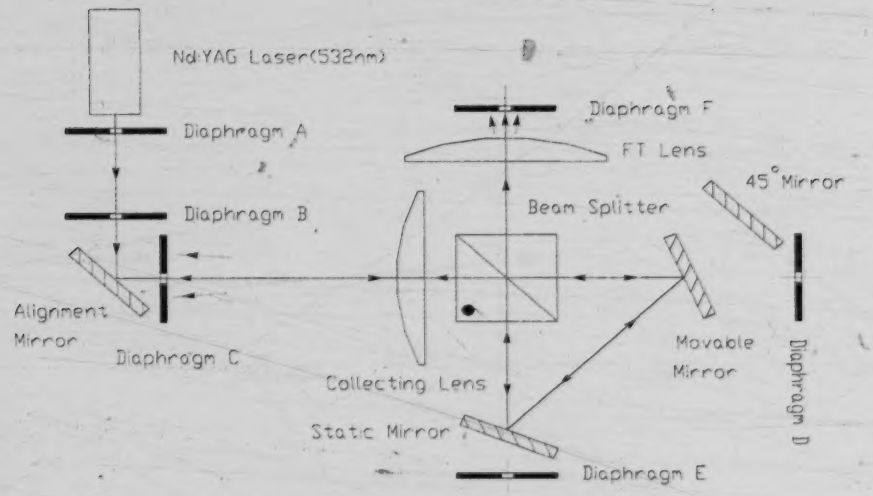

Fig. B-8 Alignment of the collecting lens

(07) Align Raman filter and the diaphragm

The alignment of Raman filter and light collection diaphragm are relatively easy as shown in Figure B-9. Just adjust these components until the laser goes through the centers of diaphragm and Raman filter.

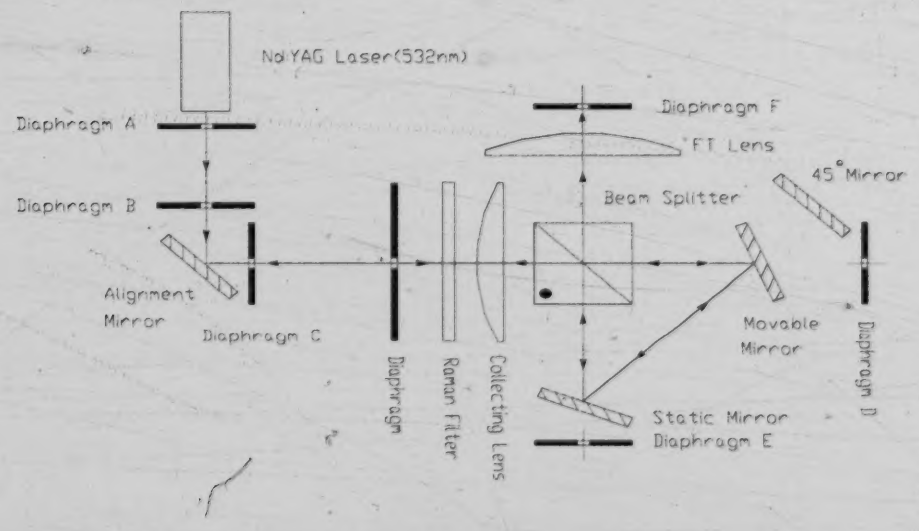

Fig. B-9 Alignment of the diaphragm and Raman filter

(08) Alignment of Hg Lamp and UV CCD

The UV CCD camera should never be aligned by using the Nd:YAG 532nm laser beam, otherwise the UV CCD camera will be seriously damaged. An Oriel Hg lamp is used for the alignment of UV CCD instead of laser. The Hg lamp is inserted into a specially designed housing with 1 mm diameter opening on both sides. Move the Hg lamp out of the housing first and put the housing in the path of laser beam and make sure the laser beam goes through 1mm pinholes on the housing as shown in Figure B-10. After this, insert the Hg lamp into its housing.

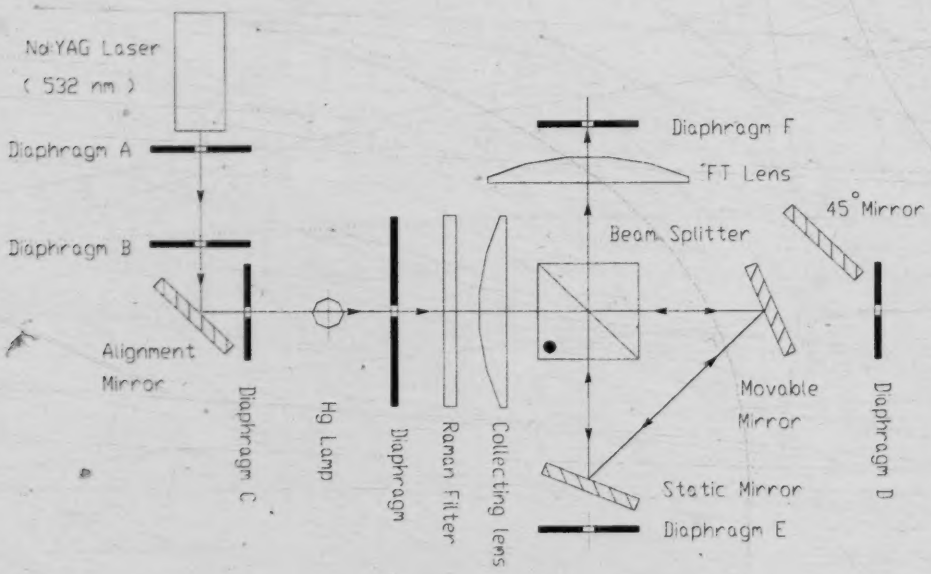

Fig. B-10 Alignment of the Hg lamp

After properly aligning the Hg lamp, turn off the laser and insert a beam block between the diaphragm A and B as a precaution in case that laser is turned on accidentally and may cause damage to the UV CCD camera.

As shown in Figure B-11, turn off the 532 nm Nd:YAG laser, insert a beam block and put in the UV CCD camera. Run the UV CCD camera in the image mode. The image of diaphragm F will show up on computer monitor as shown in Figure B-12. By moving the UV CCD camera in the vertical or horizontal direction with respect to the optical beam, center the UV CCD camera in the beam. Close the window of the UV CCD camera for protection.

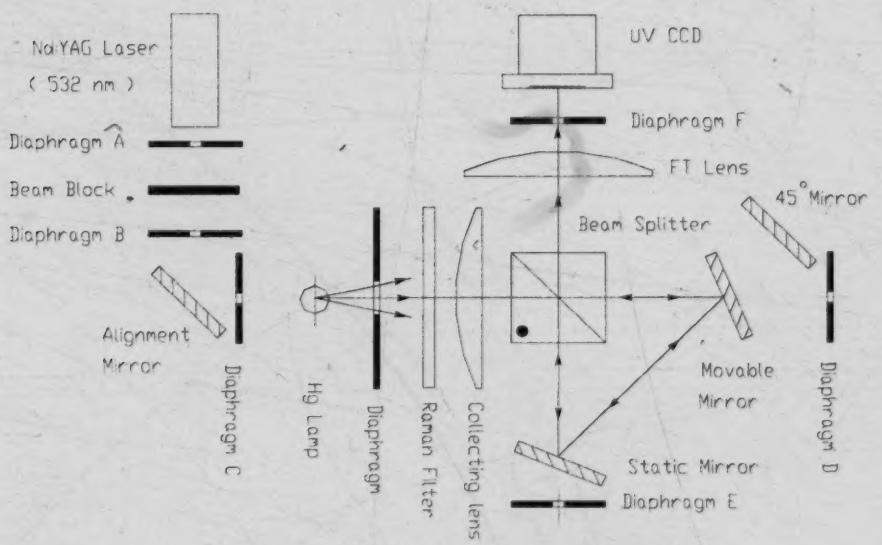

Fig. B-11 Alignment of the UV CCD camera

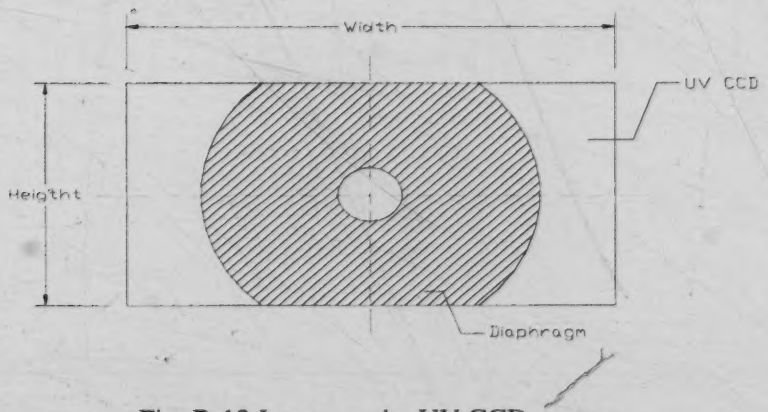

Fig. B-12 Image on the UV CCD camera

(09) **Alignment of the 4ω Nd:YAG**

As shown in Figure B-13, locate two diaphragms M, N with the same height as diaphragm A. Locate another diaphragm at the position where originally the Hg lamp sat which will be the location of the samples. Close the window of the UV CCD camera to avoid any damage to it. Turn on the 532 nm Nd:YAG laser and let the laser beam go though a diaphragm located at the sample position. Then rotate this diaphragm 90 degrees around its vertical axis. Turn on the 4ω Nd:YAG laser and let the laser beam go through the diaphragm M, N and the diaphragm located at the sample position. Now, remove the diaphragm at the sample position and put a sample in. Also align the beam dump in order to block stray laser light in the case that transparent samples are used.

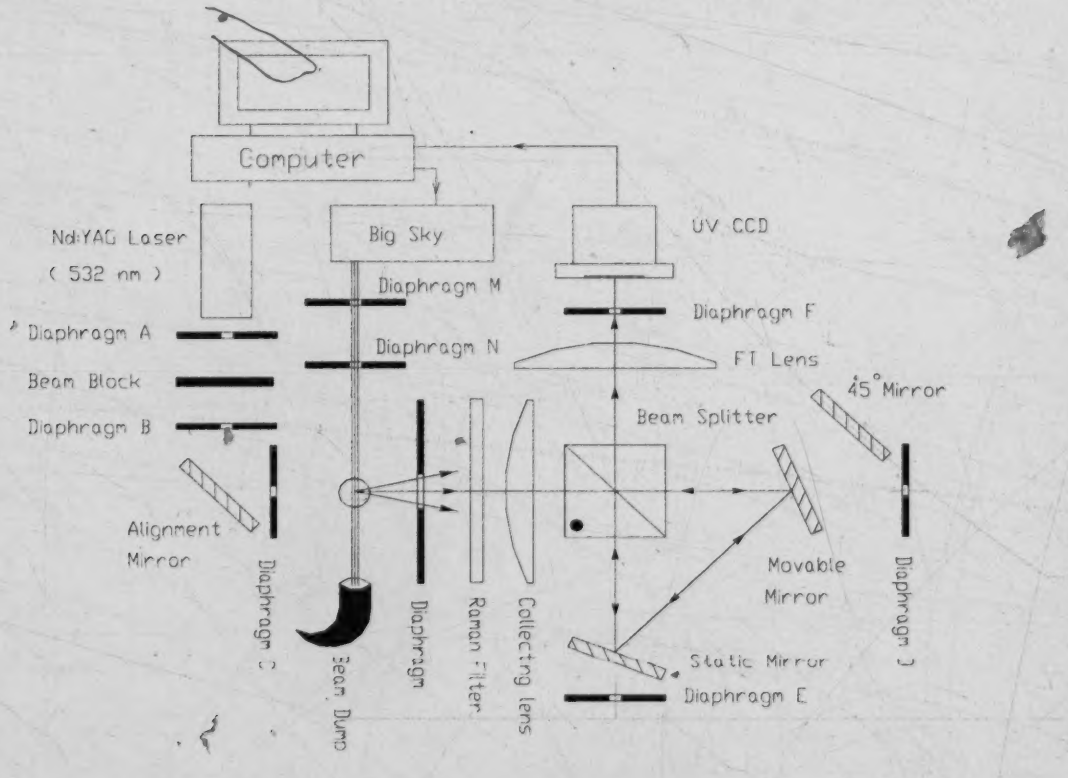

Fig. B-13 The alignment of the Big Sky laser

Appendix C

Fourier Transform program

with

an example output graph

```
%%%%%%%%%%%%%%%%%%%%%%%%%%%%%%%%%%%%%%%%%%%%%%%%%%%%%%%%%%%%%%%%%%%%%%%%%%%%%%%%
%     FT Raman spectroscopy with a Sagnac interferometer                        %
%     Written by Bin Li, April 18, 2002, with Matlab, this file is at %
%     D:\Binli\Data\2002 Data\July 22 2002_H2O_Methanol_LIBS\raman.m  %
%%%%%%%%%%%%%%%%%%%%%%%%%%%%%%%%%%%%%%%%%%%%%%%%%%%%%%%%%%%%%%%%%%%%%%%%%%%%%%%%

FileID = 'teflon10s.asc';      % *.asc was exported from UV CCD software
fid_rawdata = fopen(FileID);
Raw_data_fringes = fscanf(fid_rawdata,'%f',[2,2048])';

Hgnm = fopen('Hgcalnm.txt'); % Wavelength calibration,see section 3.4.3
Wavelength= fscanf( Hgnm,'%f',[1,513])';
Hgcm = fopen('Hgcalcm.txt'); % Wavelength calibration,see section 3.4.3
Wavenumber= fscanf( Hgcm,'%f',[1,513])';
fstatus = fclose('all');

%%%%%%%%%%%%%%%%%%%%%%%%%%%%%%%%%%%%%%%%%%%%%%%%%%%%%%%%%%%%%%%%%%%%%%%%%%%%%%%%
%    Plot Fringes pattern in subplot (1) and subplot (2)                        %
%%%%%%%%%%%%%%%%%%%%%%%%%%%%%%%%%%%%%%%%%%%%%%%%%%%%%%%%%%%%%%%%%%%%%%%%%%%%%%%%

for i=1:2048
   X_fringes(i)=Raw_data_fringes(i,1);
   Y_fringes(i)=Raw_data_fringes(i,2);
end

subplot(2,2,1);  % In subplot(1), show raw fringes pattern on CCD
plot(X_fringes(1:2048),Y_fringes(1:2048));
y11=3.8e6;    y12=4.8e6;
axis([1 2048 y11 y12]);
title('Fringe patterns');xlabel('pixels');ylabel('Counts')

subplot(2,2,2);  % In subplot(2), show the detail fringes of subplot(1)
plot(X_fringes(1:2048),Y_fringes(1:2048));
y21=4.63e6;    y22=4.75e6;
axis([900 1000 y21 y22]);
title('Fringe patterns in detail');xlabel('pixels');ylabel('Counts')

%%%%%%%%%%%%%%%%%%%%%%%%%%%%%%%%%%%%%%%%%%%%%%%%%%%%%%%%%%%%%%%%%%%%%%%%%%%%%%%%
%                 Fourier Transform                                             %
%%%%%%%%%%%%%%%%%%%%%%%%%%%%%%%%%%%%%%%%%%%%%%%%%%%%%%%%%%%%%%%%%%%%%%%%%%%%%%%%

Nstart=512;                                    % The start point  of FFT
Npoints=1024;                                  % The total points of FFT

for i=1:(2048-Nstart)
   Raw_data_Npoints(i)=Raw_data_fringes(i-1+Nstart,2);
end

Mean_Raw_Data_N=mean(Raw_data_Npoints);
Period_FFT=(0:Npoints/2)/Npoints;      %Assign 'FFT_domain' by 0~0.5pi
Inten_FFT=abs(fft((Raw_data_Npoints - Mean_Raw_Data_N),Npoints));
FFT_Inten_Period=[-Period_FFT(1:(Npoints/2+1))',...
                  Inten_FFT(1:(Npoints/2+1))'];
FFT_Inten_nm=[Wavelength(1:(Npoints/2+1)),Inten_FFT(1:(Npoints/2+1))'];
FFT_Inten_cm=[Wavenumber(1:(Npoints/2+1)),Inten_FFT(1:(Npoints/2+1))'];
```

```
%%%%%%%%%%%%%%%%%%%%%%%%%%%%%%%%%%%%%%%%%%%%%%%%%%%%%%%%%%%%%%%%%%%%%%%%%%%%
%    Plot(3) Fourier Transform specrtum by Wavelength (nm)                    %
%%%%%%%%%%%%%%%%%%%%%%%%%%%%%%%%%%%%%%%%%%%%%%%%%%%%%%%%%%%%%%%%%%%%%%%%%%%%

subplot(2,2,3);
plot(Wavelength,Inten_FFT(1:(Npoints/2+1)));
y3=6e6;                                % Change according the peak value
axis([250 350 -inf y3]);
title('Fourier Transform');xlabel('Wave Length ( nm )');ylabel('a.u.')

str3(1) = {'CCD@Z+19.0mm'};    % Str3 describe experimental conditions
str3(2) = {'Mirror:12.230mm'};
str3(3) = {'File: Teflon 10s.asc'};
str3(4) = {'Date: 07/22/02'};
str3(5) = {'FVB, Temp = -50'};
str3(6) = {'No. of Accu. 1,000'};
str3(7) = {'Readout time 32e-6s'};
str3(8) = {'Laser energy, Full'};
str3(9) = {'s  Polarization'};
str3(10) = {strcat('Start point:  ',num2str(Nstart))};
str3(11) = {strcat('FFT Points:  ',num2str(Npoints))};
text(300,0.5*y3, str1,'FontSize',8)          % put str3 in subplot(3)

%%%%%%%%%    semi-auto label peak's wavelength   %%%%%%%%%%%%%%%%%%%%%%%

% Note: How to use this ?
% Look at the spectrum first, gues a peak's wavelength,
% then assign some value for 'wv*_start' < guess value < 'wv*_end'

wv1=zeros((Npoints/2+1),2);  wv1_start=260;   wv1_end=270;
wv2=zeros((Npoints/2+1),2);  wv2_start=270;   wv2_end=273;
wv3=zeros((Npoints/2+1),2);  wv3_start=272;   wv3_end=280;
wv4=zeros((Npoints/2+1),2);  wv4_start=280;   wv4_end=305;

for i=(Npoints/2+1):-1:1
   if FFT_Inten_nm(i,1)>wv1_start &   FFT_Inten_nm(i,1)<wv1_end
      wv1(i,1)=FFT_Inten_nm(i,1);  wv1(i,2)=FFT_Inten_nm(i,2);
   end
   if FFT_Inten_nm(i,1)>wv2_start &   FFT_Inten_nm(i,1)<wv2_end
      wv2(i,1)=FFT_Inten_nm(i,1);  wv2(i,2)=FFT_Inten_nm(i,2);
   end
   if FFT_Inten_nm(i,1)>wv3_start &   FFT_Inten_nm(i,1)<wv3_end
      wv3(i,1)=FFT_Inten_nm(i,1);  wv3(i,2)=FFT_Inten_nm(i,2);
   end
   if FFT_Inten_nm(i,1)>wv4_start &   FFT_Inten_nm(i,1)<wv4_end
      wv4(i,1)=FFT_Inten_nm(i,1);  wv4(i,2)=FFT_Inten_nm(i,2);
   end
end

[y_wv1,i_wv1]= max(wv1(1:(Npoints/2+1),2));   x_wv1= wv1(i_wv1,1);
[y_wv2,i_wv2]= max(wv2(1:(Npoints/2+1),2));   x_wv2= wv2(i_wv2,1);
[y_wv3,i_wv3]= max(wv3(1:(Npoints/2+1),2));   x_wv3= wv3(i_wv3,1);
[y_wv4,i_wv4]= max(wv4(1:(Npoints/2+1),2));   x_wv4= wv4(i_wv4,1);

text(x_wv2, 1.1*y_wv2, strcat(num2str(x_wv2,'%4.1f')), ...
     'Rotation',90,'FontSize',8)
text(x_wv3, 1.1*y_wv3, strcat(num2str(x_wv3,'%4.1f')), ...
```

```
     'Rotation',00,'FontSize',8)
text(x_wv4, 1.5*y_wv4, strcat(num2str(x_wv4,'%4.1f')), ...
     'Rotation',90,'FontSize',8)

%%%%%%%%%%%%%%%%%%%%%%%%%%%%%%%%%%%%%%%%%%%%%%%%%%%%%%%%%%%%%%%%%%%%%%%%%%%%%%%
%    Plot(4) Fourier Transform specrtum by Wave number (-cm)                    %
%%%%%%%%%%%%%%%%%%%%%%%%%%%%%%%%%%%%%%%%%%%%%%%%%%%%%%%%%%%%%%%%%%%%%%%%%%%%%%%

subplot(2,2,4);
plot(Wavenumber,Inten_FFT(1:(Npoints/2+1)));
y4=6e6;                                    %Change according maximum data
axis([ -500 5000 -inf y4]);
title('Fourier Transform');
xlabel('Wave Number ( cm -1 )');ylabel('a.u.')

%%%%%%%%%    semi-auto label peak's wave number  %%%%%%%%%%%%%%%%%%%%%%%

% Note: How to use this ? Refer to semi-auto label peak's wavelength

wv1=zeros((Npoints/2+1),2);  wv1_start=-100;  wv1_end=100;
wv2=zeros((Npoints/2+1),2);  wv2_start=500;   wv2_end=1000;
wv3=zeros((Npoints/2+1),2);  wv3_start=1000;  wv3_end=1500;
wv4=zeros((Npoints/2+1),2);  wv4_start=2000;  wv4_end=4000;

for i=(Npoints/2+1):-1:1
   if FFT_Inten_cm(i,1)>wv1_start &   FFT_Inten_cm(i,1)<wv1_end
      wv1(i,1)=FFT_Inten_cm(i,1);  wv1(i,2)=FFT_Inten_cm(i,2);
   end
   if FFT_Inten_cm(i,1)>wv2_start &   FFT_Inten_cm(i,1)<wv2_end
      wv2(i,1)=FFT_Inten_cm(i,1);  wv2(i,2)=FFT_Inten_cm(i,2);
   end
   if FFT_Inten_cm(i,1)>wv3_start &   FFT_Inten_cm(i,1)<wv3_end
      wv3(i,1)=FFT_Inten_cm(i,1);  wv3(i,2)=FFT_Inten_cm(i,2);
   end
   if FFT_Inten_cm(i,1)>wv4_start &   FFT_Inten_cm(i,1)<wv4_end
      wv4(i,1)=FFT_Inten_cm(i,1);  wv4(i,2)=FFT_Inten_cm(i,2);
   end
end

[y_wv1,i_wv1]= max(wv1(1:(Npoints/2+1),2));   x_wv1= wv1(i_wv1,1);
[y_wv2,i_wv2]= max(wv2(1:(Npoints/2+1),2));   x_wv2= wv2(i_wv2,1);
[y_wv3,i_wv3]= max(wv3(1:(Npoints/2+1),2));   x_wv3= wv3(i_wv3,1);
[y_wv4,i_wv4]= max(wv4(1:(Npoints/2+1),2));   x_wv4= wv4(i_wv4,1);

text(x_wv2, 1.2*y_wv2, strcat(num2str(x_wv2,'%4.0f')), ...
   'Rotation',0,'FontSize',8)
text(x_wv3, 1.1*y_wv3, strcat(num2str(x_wv3,'%4.0f')), ...
   'Rotation',0,'FontSize',8)
text(x_wv4, 1.5*y_wv4, strcat(num2str(x_wv4,'%4.0f')), ...
   'Rotation',90,'FontSize',8)

%%%%%%%%%%%%%%%%%%%%%%%%%%%%%%%%%%%%%%%%%%%%%%%%%%%%%%%%%%%%%%%%%%%%%%%%%%%%%%%
%   End. Please refer to the output picture on next page                        %
%%%%%%%%%%%%%%%%%%%%%%%%%%%%%%%%%%%%%%%%%%%%%%%%%%%%%%%%%%%%%%%%%%%%%%%%%%%%%%%
```

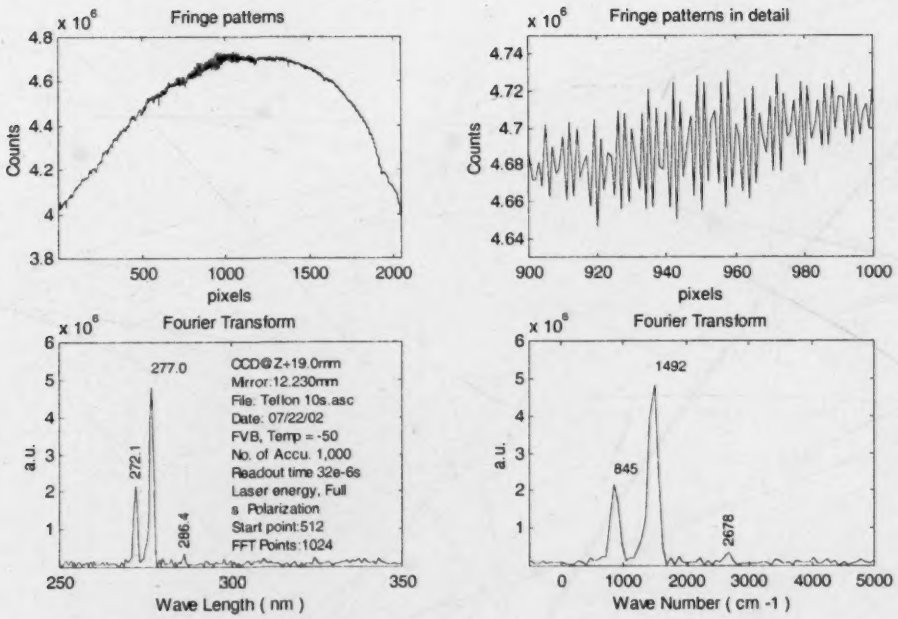

Figure C-1 An example output graph of the Fourier Transform program for a Raman spectrum of Teflon

Appendix D

The characteristics of the FT Hg spectrum

as a function of movable mirror displacement

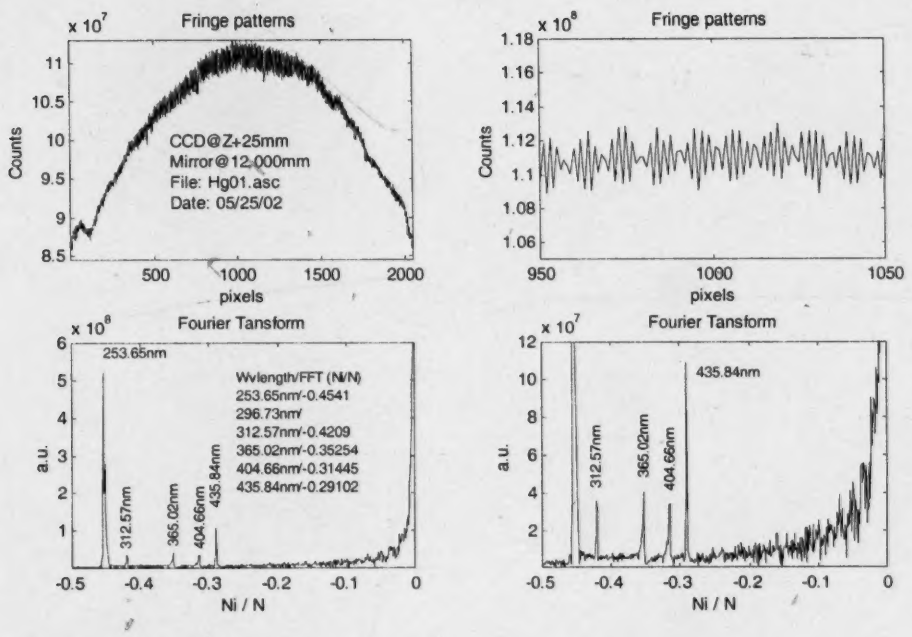

Figure D-1 FT Hg spectrum with the movable mirror at 12.000 mm

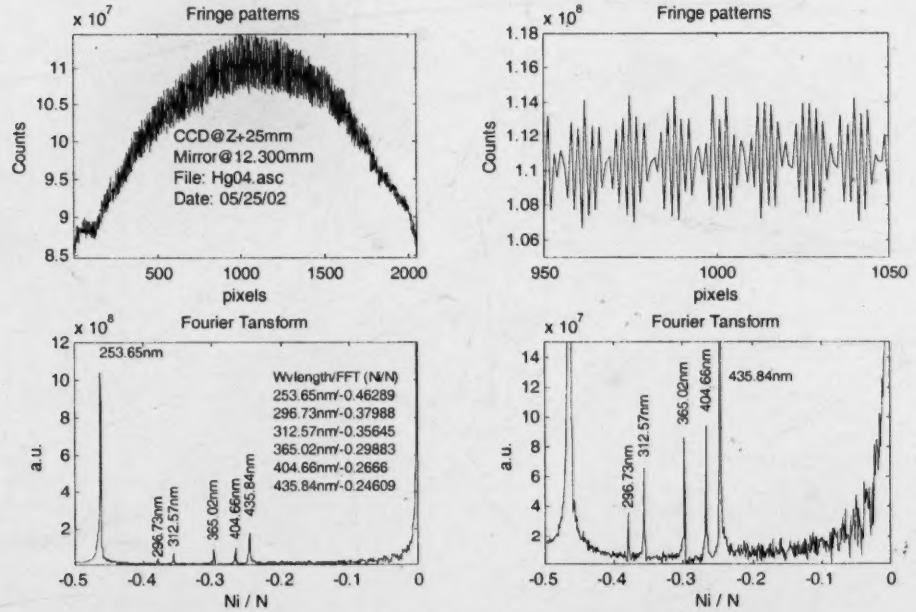

Figure D-2 FT Hg spectrum with the movable mirror at 12.300 mm

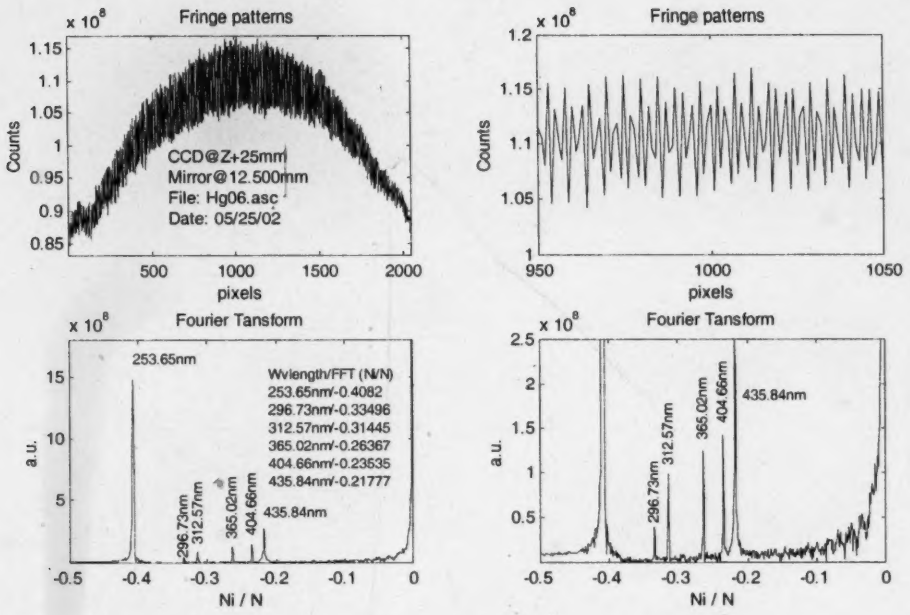

Figure D-3 FT Hg spectrum with the movable mirror at 12.500 mm

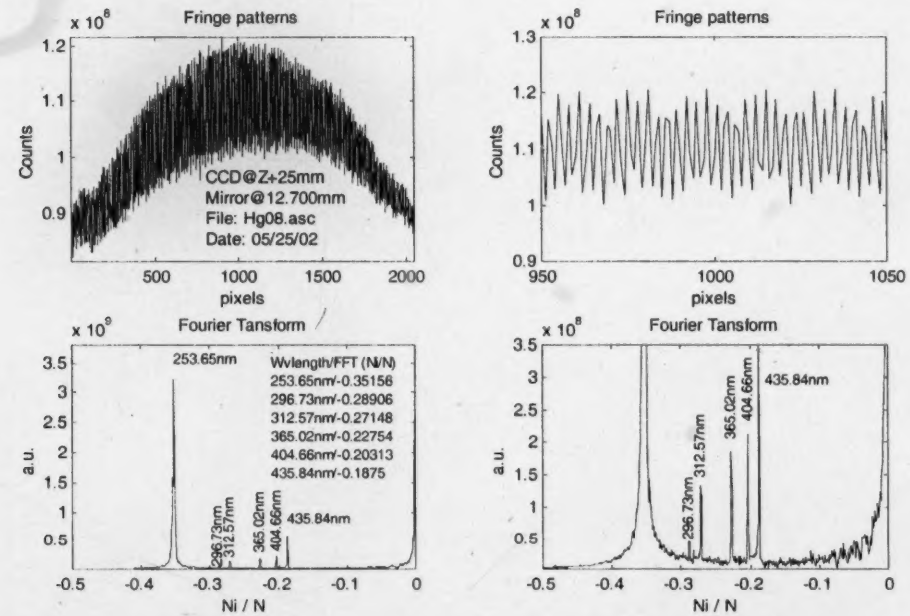

Figure D-4 FT Hg spectrum with the movable mirror at 12.700 mm

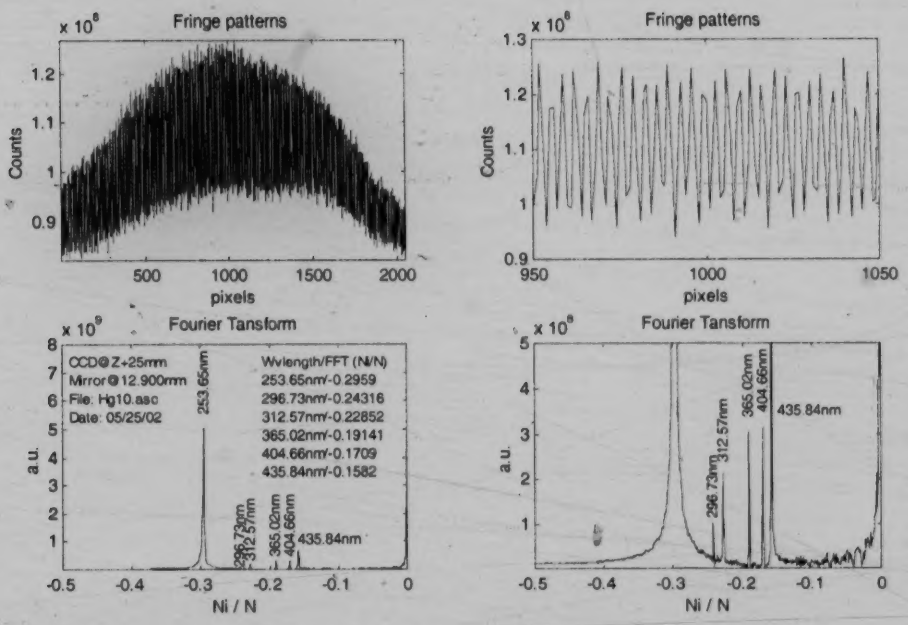

Figure D-5 FT Hg spectrum with the movable mirror at 12.900 mm

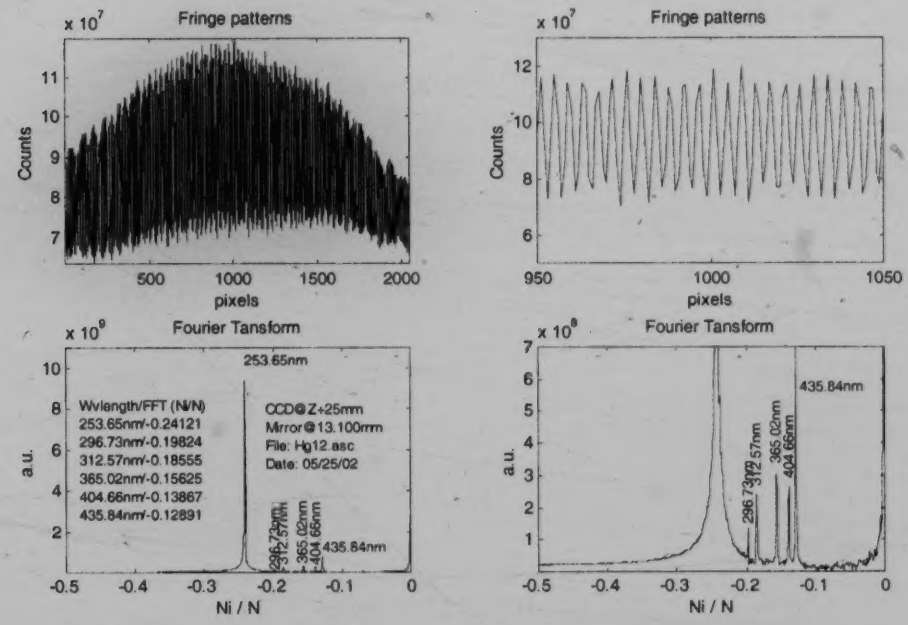

Figure D-6 FT Hg spectrum with the movable mirror at 13.100 mm

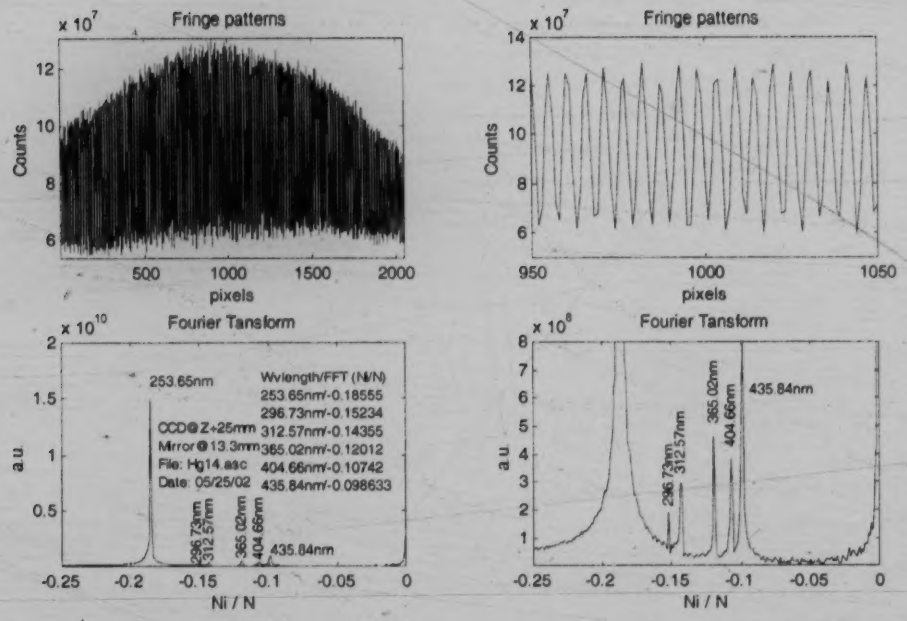

Figure D-7 FT Hg spectrum with the movable mirror at 13.300 mm

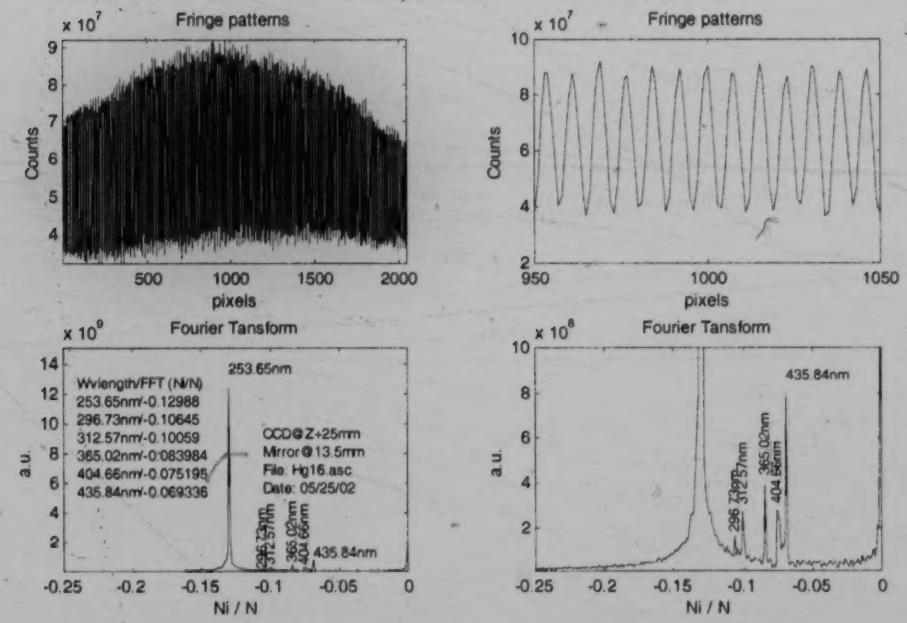

Figure D-8 FT Hg spectrum with the movable mirror at 13.500 mm

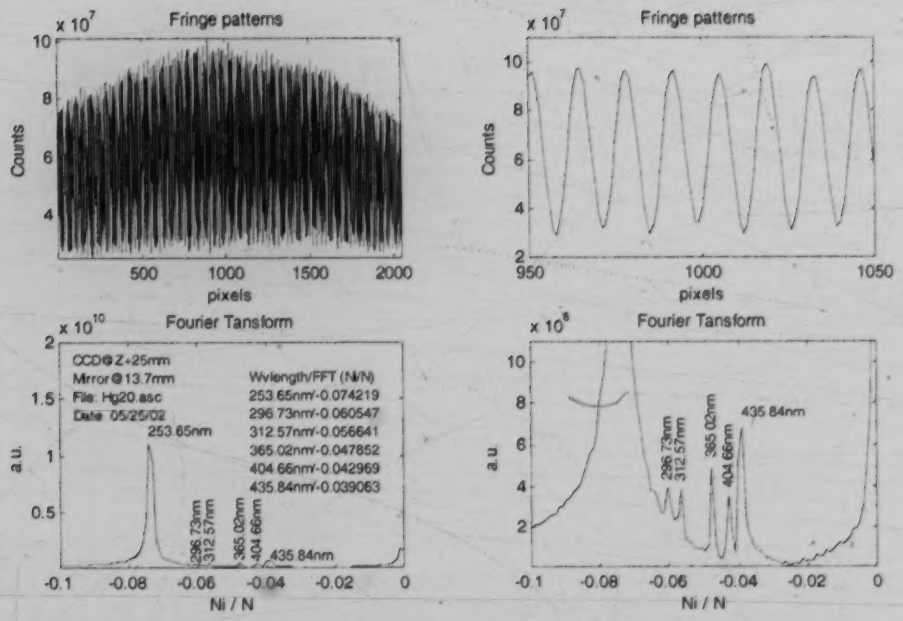

Figure D-9 FT Hg spectrum with the movable mirror at 13.700 mm

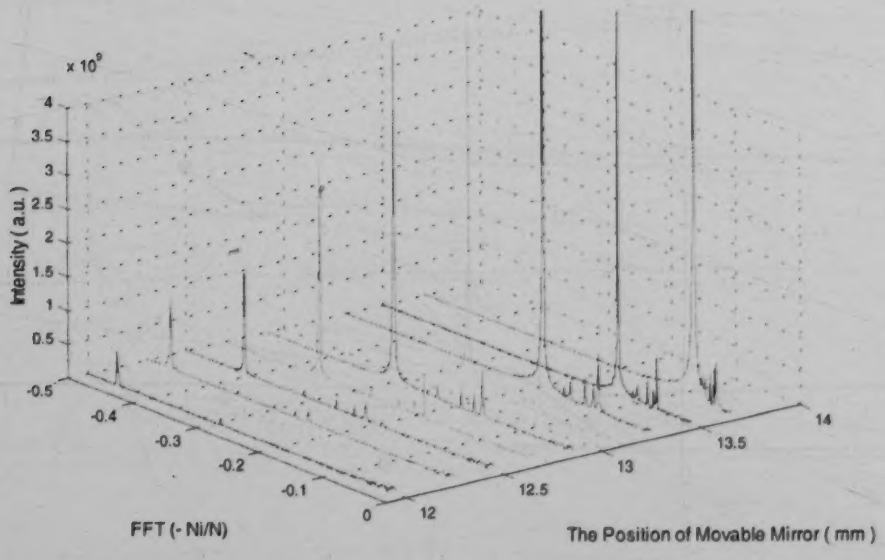

Figure D-10 FT Hg spectrum 3-D plot with the movable mirror in a serial position

Appendix E

The characteristics of the FT Hg spectrum as a function of the UV CCD camera position

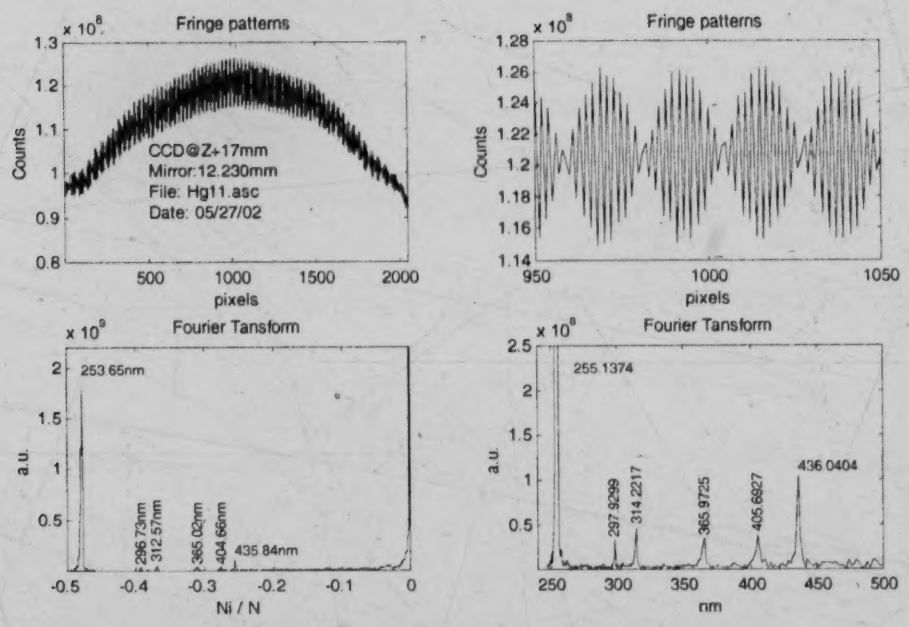

Figure E-1 FT Hg spectrum with UV CCD at Z+17 mm

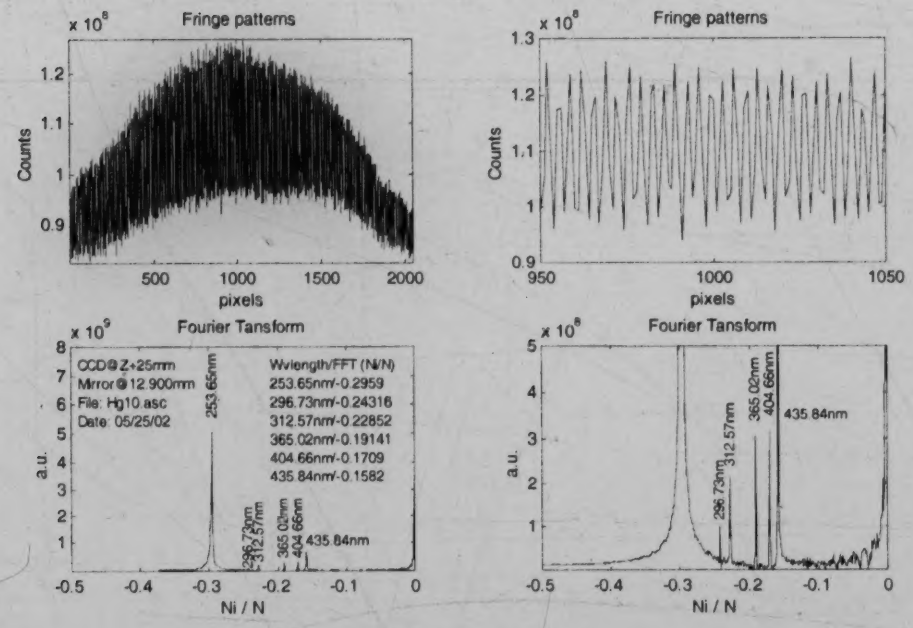

Figure E-2 FT Hg spectrum with UV CCD at Z+18 mm

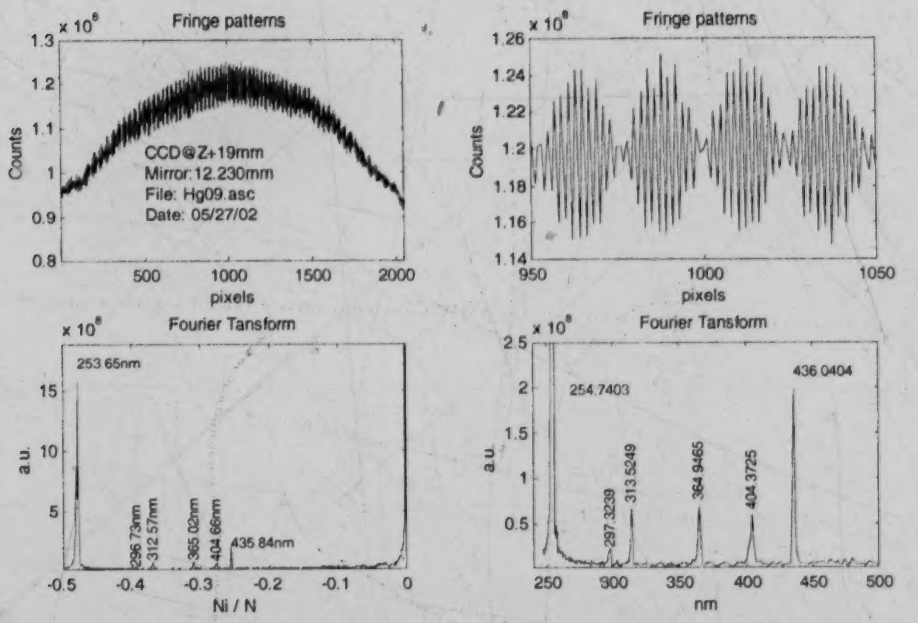

Figure E-3 FT Hg spectrum with UV CCD at Z+19 mm

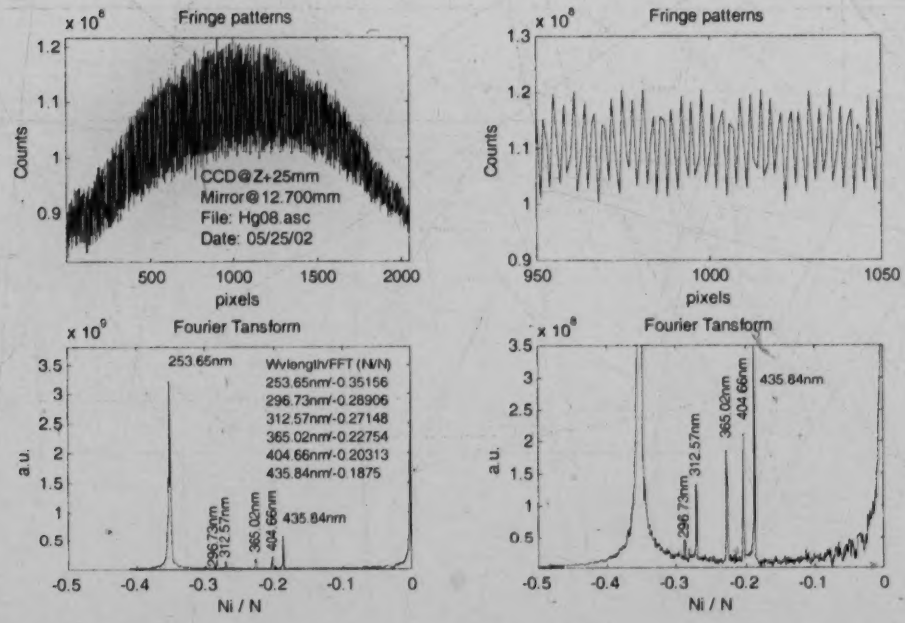

Figure E-4 FT Hg spectrum with UV CCD at Z+20 mm

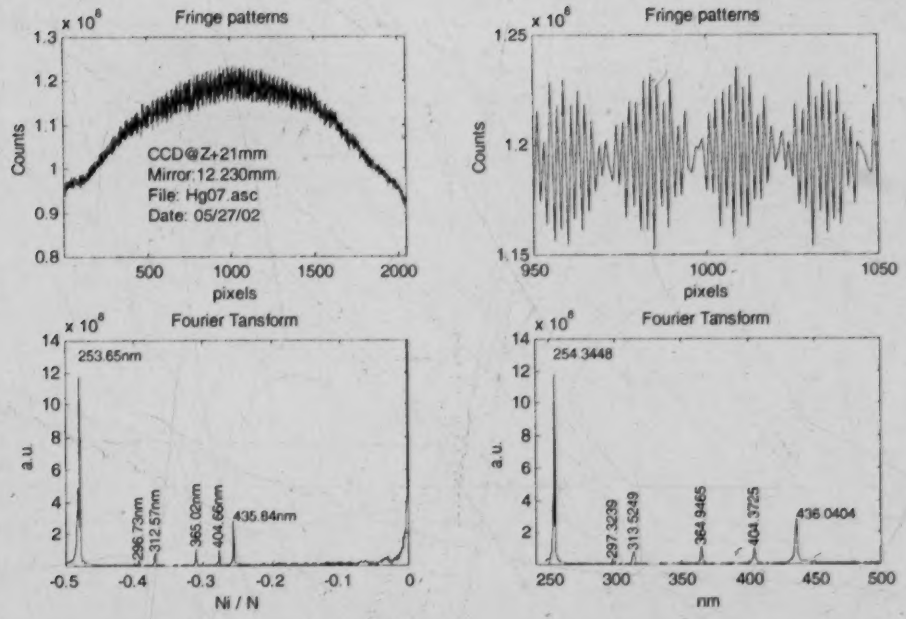

Figure E-5 FT Hg spectrum with UV CCD at Z+21 mm

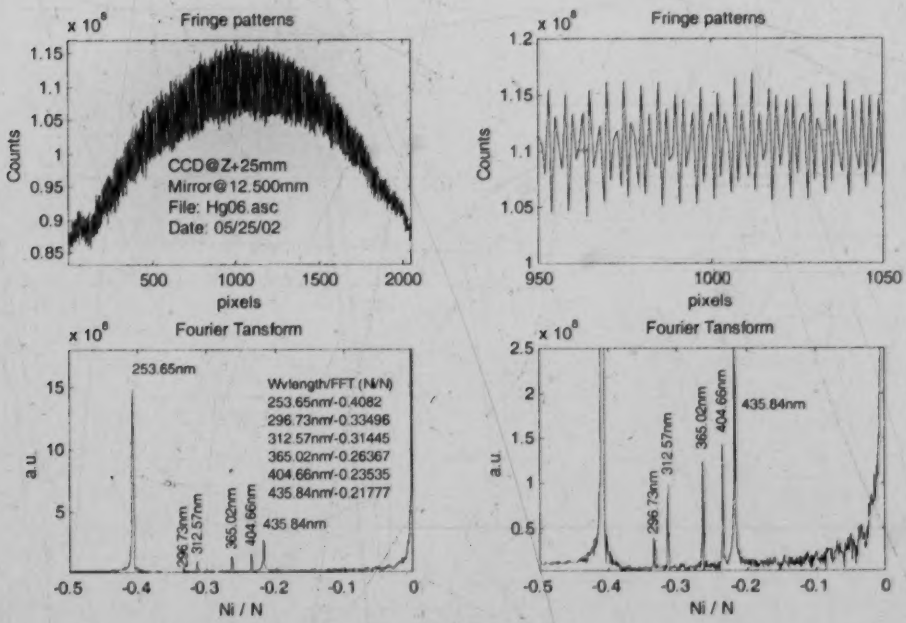

Figure E-6 FT Hg spectrum with UV CCD at Z+22 mm

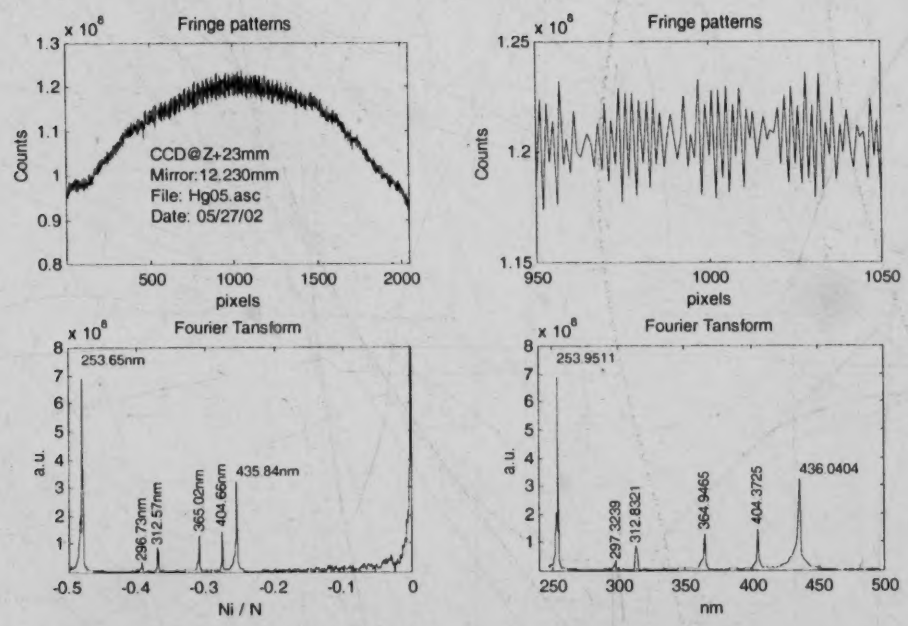

Figure E-7 FT Hg spectrum with UV CCD at Z+23 mm

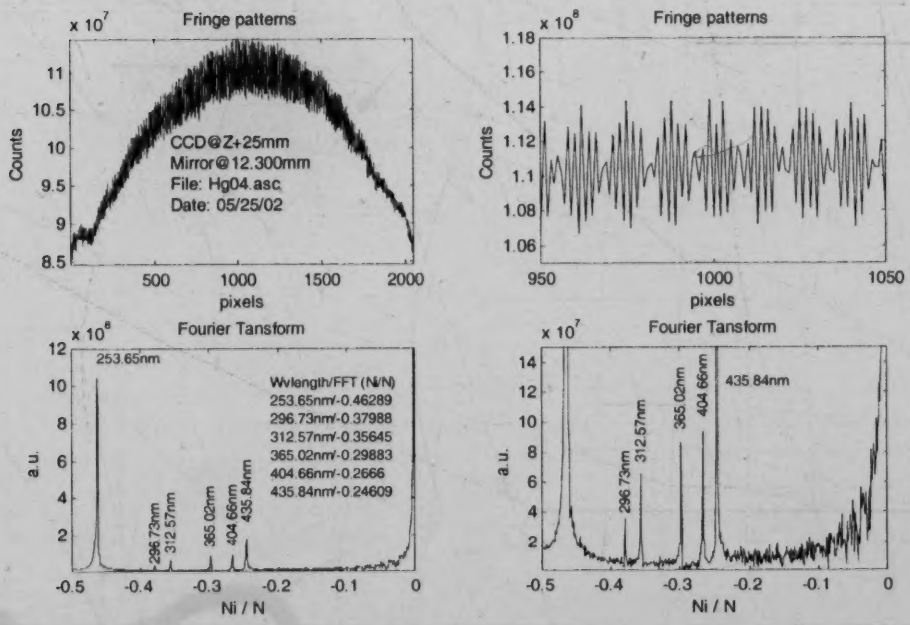

Figure E-8 FT Hg spectrum with UV CCD at Z+24 mm

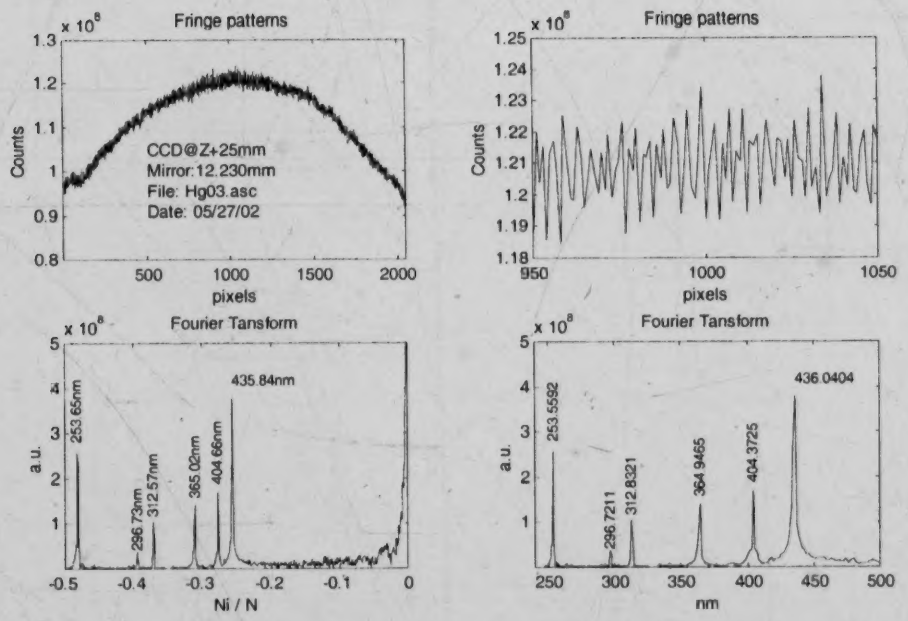

Figure E-9 FT Hg spectrum with UV CCD at Z+25 mm

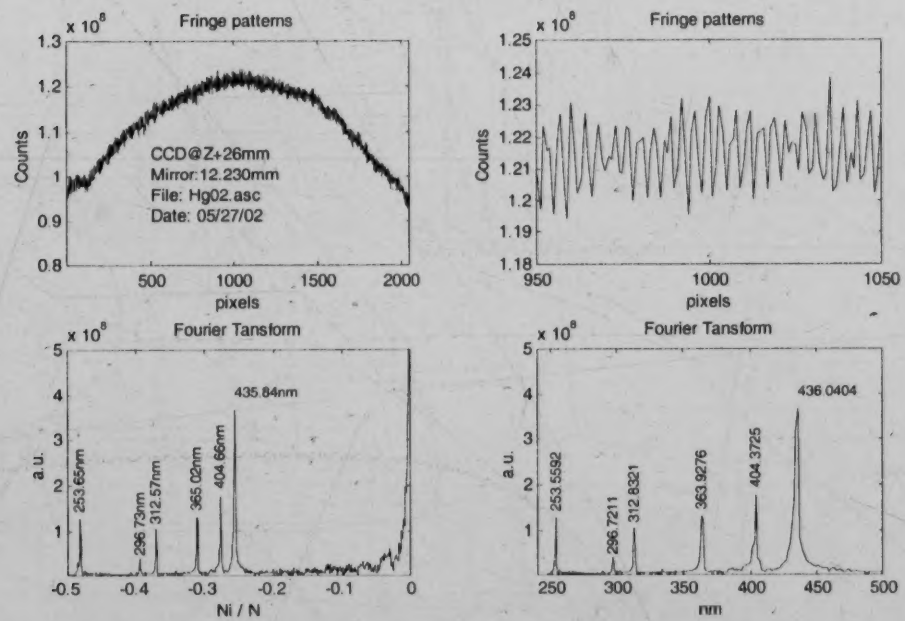

Figure E-10 FT Hg spectrum with UV CCD at Z+26 mm

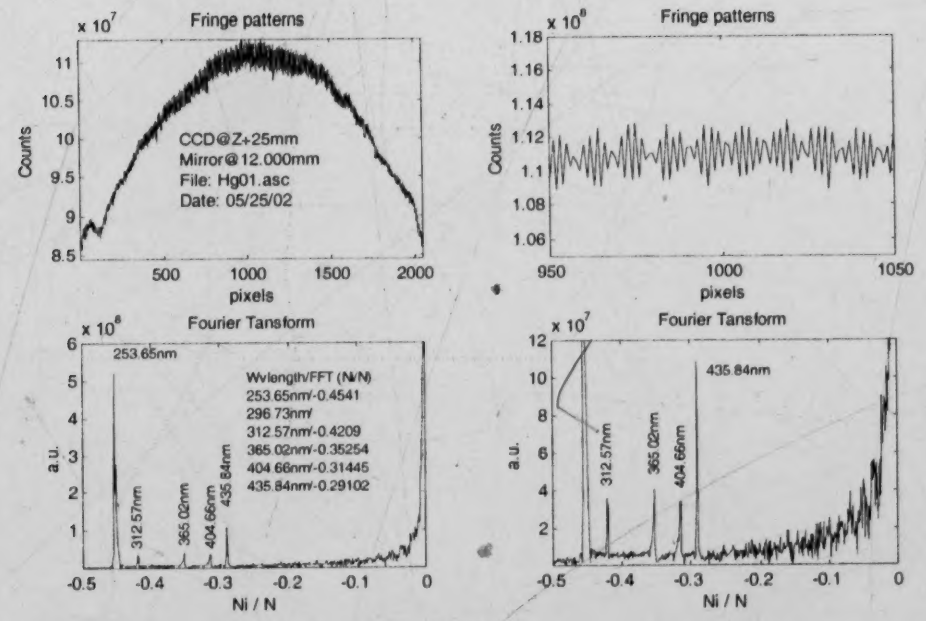

Figure E-11 FT Hg spectrum with UV CCD at Z+27 mm

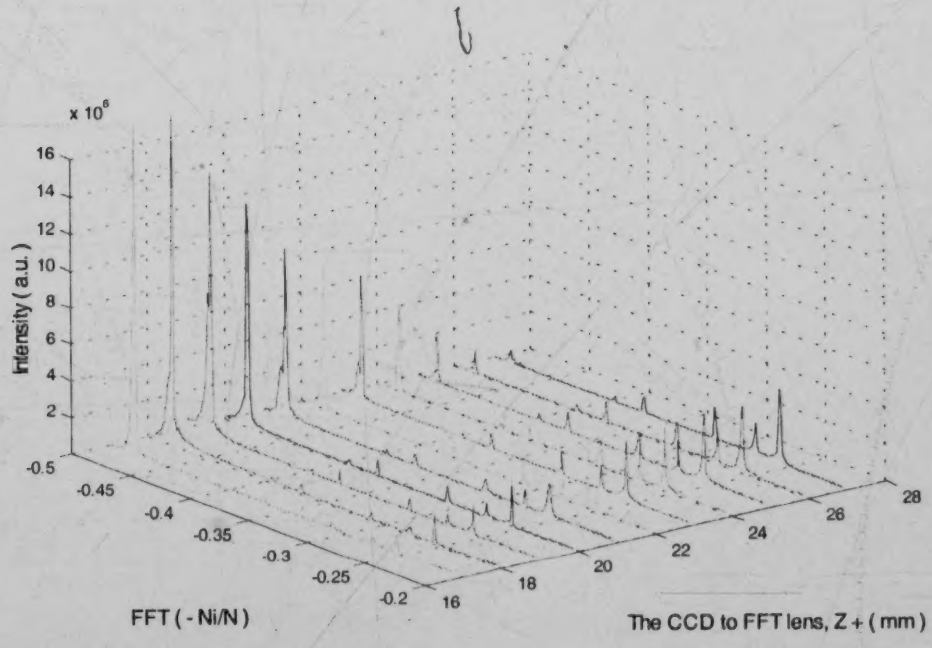

Figure E-12 FT Hg spectrum 3-D plot with UV CCD in a serial position